Interactions of molecules in the vicinity of gold nanoparticles

Lidiya Osinkina

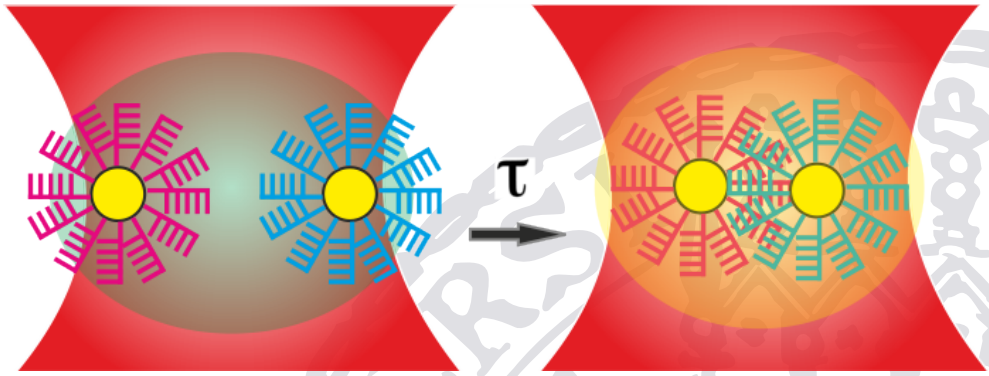

München 2014

Interactions of molecules in the vicinity of gold nanoparticles

Lidiya Osinkina

München 2014

Interactions of molecules in the vicinity of gold nanoparticles

Lidiya Osinkina

Dissertation
der Fakultät für Physik
der Ludwig-Maximilians-Universität
München

vorgelegt von
Lidiya Osinkina
aus Charkiw, Ukraine

München
21. 02. 2014

First reviewer:	Prof. Dr. Jochen Feldmann
Second reviewer:	Prof. Dr. Jan von Delft
Date of Defence:	16.12.2014

Title figure: Schematic drawing of binding of two biofunctionalised gold nanoparticles in the optical trap

Publications discussed in this work

- L. Osinkina, S. Carretero-Palacios, J. Stehr, A. A. Lutich, F. Jäckel, J. Feldmann

  Tuning DNA Binding Kinetics in an Optical Trap by Plasmonic Nanoparticle Heating

  Nano Letters, 13, 3140-3144 (2013).

- L. Osinkina, T. Lohmüller, F. Jäckel, J. Feldmann

  Synthesis of Gold Nanostar Arrays as Reliable, Large-Scale, Homogeneous Substrates for Surface-Enhanced Raman Scattering Imaging and Spectroscopy

  The Journal of Physical Chemistry C, 117, 22198-22202 (2013).

- V. Fässler, C. Hrelescu, A. A. Lutich, L. Osinkina, S. Mayilo, F. Jäckel, J. Feldmann

  Accelerating fluorescence resonance energy transfer with plasmonic nanoresonators

  Chemical Physics Letters, 508, 67-70 (2011).

Other publications

- L. Osinkina, M. Markström, O. Orwar, A. Jesorka

  A Method for Heat Stimulated Compression of (poly(N-isopropylacrylamide) Hydrogel Inside Giant Unilamellar Vesicles

  Langmuir, 26, 1-4 (2010).

- J. Baran, L. Dolgov, T. Gavrilko, L. Osinkina, G. Puchkovska, H. Ratajczak, Y. Shaydyuk, A. Hauser

  Effect of clay surface modification on the structure and electro-optical properties of liquid crystal/clay nanocomposites

  Philosophical Magazine, 87, 4273-4285 (2007).

Contributions to conferences and workshops

- V. Fässler, C. Hrelescu, A. A. Lutich, L. Osinkina, S. Mayilo, F. Jäckel, J. Feldmann

  Plasmonic nanoresonators for the manipulation of fluorescence resonant energy transfer

  iNANO Summer School for Nanooptics; Aarhus, Denmark, September 2010.

- L. Osinkina

  Binding kinetics in the optical trap; Nanostar arrays

  Workshop "From Biophotonics to Optoelectronics"; Riezlern, Austria, October 2011.

- L. Osinkina, T. Lohmüller, F. Jäckel, J. Feldmann

  Ordered nanostar arrays as reliable substrates for surface enhanced Raman scattering (SERS)

  DPG Spring meeting; Berlin, Germany, March 2012.

Contents

Kurzfassung

Goldnanopartikel (AuNPs) besitzen die Eigenschaft die Temperatur ihres umliegenden Mediums lokal zu erhöhen. Auch treten in der Nähe ihrer Oberfläche Regionen mit hoher Feldverstärkung auf. Diese beiden Effekte resultieren aus der eingeschlossenen Oszillation der Leitungsbandelektronen, sogenannten Plasmonen, welche durch ein resonantes elektromagnetisches Feld angeregt werden. In dieser Arbeit wurden Heiz- und Feldverstärkungseigenschaften von AuNP verwendet, um die Wechselwirkungen zwischen an die AuNPs gebundenen Moleküle zu manipulieren. Zwei zwischenmolekuläre Prozesse werden untersucht: die Entstehung von DNA Doppelsträngen und der Energietransfer zwischen fluoreszenten Molekülen.

Die Bildung von DNA-Doppelsträngen in der Nähe von AuNPs wurde auf der Einzelpartikel -Ebene untersucht. Dafür wurden zwei einzelne AuNPs mit komplementären DNA-Strängen an ihren Oberflächen mit einer optischen Falle nah zueinander gebracht. Die Bildung von DNA-Doppelsträngen, welche zur Bindung zwischen einzelnen AuNPs führt, wird anhand der Änderung der optischen Eigenschaften der AuNPs durch die plasmonische Kopplung bei sehr kleinen Abständen systematisch detektiert. Außerdem wird die spezifische Bindung durch die Erhöhung der Fallenstärke um mehr als eine Größenordnung verlangsamt. Dieser Effekt ist anhand eines semi-quantitativen Modells erklärt, wonach die Temperaturerhöhung des umgebenden Mediums als Folge von plasmonischem Heizen mit der Schmelz- bzw. Denaturierungstemperatur von DNA-Strängen verglichen wird, welche zu einer Auftrennung der Doppelsträngen führt. Der plasmonische Heizeffekt bringt das System näher an die Schmelztemperatur von DNA, wodurch die Entstehung der Doppelstränge unterdrückt wird.

Des Weiteren wurde der Förster-Resonanzenergietransfer (FRET) zwischen zwei fluoreszenten Molekülen, welche an AuNPs gebunden sind, untersucht. FRET beschreibt einen strahlungsfreien Energietransfer-Prozess, durch den die Fluoreszenz des Donor-Moleküls gesenkt und die des Akzeptor-Moleküls erhöht wird. Durch die Messung der Fluoreszenzlebensdauer von Donor und Akzeptor einmal in der Nähe von AuNPs und einmal in freien FRET-Paaren wurde der Einfluss von AuNPs auf FRET quantifiziert. Die FRET-Effizienz in der Nähe von AuNPs bleibt fast so hoch wie bei freien FRET-Paaren und die FRET-Raten werden in der Anwesenheit von AuNPs erhöht. Die Simulation einer FRET-Erhöhung zwischen zwei AuNPs suggeriert die Anwesenheit von mehreren Feldverstärkenden und -abschwächenden Bereichen. Um das hier gezeigte Potential von AuNP Dimeren für eine FRET Verstärkung komplett auszuschöpfen, wird eine präzise Positionierung der Moleküle notwendig.

Abstract

Gold nanoparticles (AuNPs) can locally increase the temperature of their surrounding medium and provide regions of high field enhancement near their surface. The origin of these two effects lies in the confined oscillations of conduction band electrons called plasmons, which are excited by the resonant electromagnetic field. In this thesis heating and field enhancing properties of AuNPs are used to manipulate the interaction of molecules attached to them. Two intermolecular processes are studied: formation of DNA double strand and energy transfer between fluorescent molecules.

Formation of DNA double strands near AuNPs is studied on the single-particle level. To this end, two single AuNPs with complementary DNA strands on their surface are brought into close proximity by optical trapping. The formation of DNA double strands leading to binding between two single nanoparticles is detected systematically by the change of the optical properties of AuNPs due to plasmonic coupling at small distances. Moreover, the increase of the trapping laser power slows down the specific binding by more than an order of magnitude. The observed result is explained by a semi-quantitative model where the temperature increase of the surrounding medium due to plasmonic heating is compared to the temperature required to dissociate DNA double helices. Plasmonic heating brings the system closer to the melting temperature and the formation of double strand is suppressed.

Further, Förster resonant energy transfer (FRET) between two fluorescent species attached to AuNPs is investigated. FRET is a non-radiative energy transfer leading to the decrease of fluorescence of the donor molecule and increase of fluorescence of the acceptor molecule. By measuring the fluorescence lifetime of donor and acceptor molecules near AuNPs and in free FRET pairs we quantify the influence of AuNPs on FRET. FRET efficiencies near AuNPs stay nearly as high as in the case of free FRET pairs and FRET rates in the presence of AuNPs are increased. The simulations of FRET enhancement between AuNPs suggest the presence of several regions of field enhancement and of field suppression. To fully use the potential of AuNP dimers for FRET enhancement a precise placement of molecules is required.

1 Introduction

Understanding the interactions between biological molecules and their interaction with other species is essential to study the basic processes occuring in the world around us. Binding events and transfer processes between biomolecules have been studied in detail in bulk solution, [1–4] where molecules are homogeneously distributed in the medium. Importantly, the information obtained from bulk studies can not be assumed valid for real heterogeneous systems in which clustering and macromolecular assembling is observed [5]. For example, the hybridization of DNA single strands and formation of double helices in solution differs from the same process taking place in real cell [6]. Therefore it would be beneficial to obtain tools which allow the study of biomolecular processes in heterogeneous nanoscale systems.

The recent flourishing of nanoscale science and technology gave rise to the development of such tools. With their help very low amounts of biomolecules were detected, analyzed, mimicked and even externally manipulated. The examples here are single molecule detection with super-resolution techniques [7, 8], changing a conformation of a single molecule with scanning tunneling microscopy [9] and touchless movements of DNA molecules by laser light [10, 11].

In the last case, DNA molecules were manipulated indirectly through the small object which was attached to them and moved. It is often in nanoscience that for studies of properties and behavior of molecules, special hybrid nanosystems consisting of micro or nanoparticles attached to the molecules of interest are created. Among these nanosystems one class is of particular interest. These are nanosystems where single components influence properties of each other and therefore change the performance of the whole system.

Gold nanoparticles (AuNPs) which are capable of hosting localized oscillations of conduction band electrons, called plasmons, are very suitable to perform as an

active component for such tunable hybrid system. AuNPs are chemically rather inert so the chemical properties of molecules attached to them are preserved. On the other hand, due to the special optical characteristics of AuNPs emerging from plasmons, the field distribution around them can be changed and therefore influence optical properties of molecules situated nearby. Moreover, due to the energy dissipation during the plasmon oscillation decay in the AuNPs the temperature inside and outside of the nanoparticle increases so that the molecules in their vicinity can be efficiently heated [12, 13].

Plasmonic properties of AuNPs were succesfully used to study and tune properties of molecules attached to them. To name a few achievements, Raman scattering and fluorescence signals of molecules were strongly enhanced [14–16], fluorescence spectra of dyes situated between plasmonic nanoparticles were shaped [17], melting of DNA helices induced through plasmonic heating was studied in an ensemble [18, 19] Furthermore, the increase of energy transfer between nanoscopic donor and acceptor was predicted [20].

This thesis, for the first time, investigates how the hybridization of DNA strands and energy transfer between organic molecules can be manipulated by the optical properties of gold nanoparticle dimers situated near them. The specific binding of DNA-coated AuNPs manipulated by laser beam is investigated on the single-particle level. It is observed that the hybridization of DNA strands situated on AuNPs can be actively tuned via a change of plasmonic heating. Plasmonic heating is manipulated directly during the experiment by changing the laser settings.

Another process manipulated in this thesis is the energy transfer between dye and protein. These molecules are situated in the inter-particle region of AuNP dimer and the energy transfer is investigated on the ensemble level. The comparison is made between the performance of AuNP dimer and monomer for modification of energy tranfer rates in the protein-fluorescent dye system.

The present thesis consists of six chapters. Chapter 2 following this introduction focuses on fundamentals of AuNPs interaction with electromagnetic radiation as well as on basic properties of DNA molecules and fluorescent dyes. First, excitation of plasmonic oscillations in AuNPs as a result of interaction with incident light is described. Also, resonance conditions leading to strong plasmonic

responce are discussed. A specific plasmonic structure - AuNP dimer - is introduced, where two AuNPs are placed close to each other and their plasmonic oscillations couple. After that a method for touchless manipulation of single AuNPs with light – optical trapping (OT) – is discussed. In this thesis OT is used to bring AuNPs with molecules attached to their surface close to each other and create an AuNP dimer. Further, the structure of DNA molecules and mechanisms of formation of a DNA double helix are explained. The concept of DNA melting temperature is introduced and the latest findings about hybrid systems consisting of nanoparticles and DNA molecules are summarized. Finally, the process of Förster Resonant Energy Transfer between fluorescent dyes is discussed. The efficiency of this process is defined by the molecule's fluorescence decay rates which can be heavily altered in the presence of AuNPs.

Chapter 3 deals with the materials and experimental methods employed in this thesis. Here the synthesis, surface modification and aggregation of AuNPs are discussed. The extinction spectra of nanoparticles used in this thesis are given. Further, the mechanisms used to connect two AuNPs into a dimer in bulk and on single dimer level are explained. After that the setups used to characterize nanoparticles and their aggregates are discussed. These include electron microscopy and the dark-field mode of optical microscopy. The optical trapping technique combined with dark-field microscopy to manipulate single gold nanoparticles dispersed in water is described as well. Finally the spectroscopic methods used to study the steady-state and time-resolved optical response of AuNPs and a hybrid system containing AuNPs and organic molecules are discussed.

In chapter 4 the hybridization of complementary DNA strands attached to AuNPs is investigated. Single AuNPs with DNA on their surface are manipulated in three dimensions by OT. When two nanoparticles are in close vicinity they bind due to hybridization of complementary DNA strands. The binding event is detected optically by the change in the plasmon resonance frequency upon plasmonic coupling of AuNPs. It is shown that this specific binding can be tuned by plasmonic heating. At larger trapping powers the hybridization rates decrease by more than an order of magnitude. This result is explained by higher temperatures preventing the formation of dimers with lower binding energies. Since factors other than chemical affinity can result in the binding of

two nanoparticles in the optical trap, several control experiments which prove the specificity of binding are conducted. Finally attempts to extend the idea of binding in the optical trap to other systems including protein-functionalized AuNPs and AuNPs of non-spherical shapes, such as nanostars, are discussed.

In chapter 5 studies of Förster resonant energy transfer (FRET) between proteins and fluorescent dyes situated near AuNPs are presented. By exciting the donor in the AuNPs/FRET pair system and detecting the acceptor fluorescence the occurence of FRET is proven. The results of steady-state measurements are shown, where no difference between the FRET process in the free FRET pair and in the FRET pair attached to AuNPs was detected. Also the results of time-resolved fluorescent measurements which provide a more detailed information about FRET in different configurations are presented. Both single AuNPs and AuNP dimers accelerate FRET while AuNP dimers perform slightly better. Finally, the model calculations of the intensity enhancement near the nanoparticle monomers and dimers are introduced. The results of the calculations are in the agreement with experimental findings.

The last chapter – chapter 6 – focuses on the summary of the results as well as on conclusions and the outlook of this thesis.

2 Hybrid systems of gold nanoparticles and (bio)molecules

Gold nanoparticles (AuNPs) can enhance optical signals of neighboring molecules by several orders of magnitude [21, 22], strongly and very locally increase the temperature of nanometer-small volumes [12, 13] and are used to overcome the diffraction limit in imaging [23]. The origin of such an excellent performance lies in the peculiar response of AuNPs to electromagnetic radiation. Light of characteristic energy excites collective oscillations of conductive band electrons – plasmons – in AuNPs. Plasmons to a large extent define optical properties of AuNPs and field distribution around them. Moreover, when two AuNPs are placed close to each other, their plasmons couple giving rise to new properties.

This chapter describes the basics of plasmonic properties of AuNPs and explains how these properties influence molecules situated near them. Besides, the theory of manipulation of small objects by a laser beam and its specifics in case of plasmonic nanoparticles is explained.

Further the properties of the molecules investigated in this thesis are introduced. The structure of DNA and mechanisms of DNA double helix formation are explained. Also the concept of DNA melting temperature is introduced and double helix formation at conditions different from the bulk is discussed.

Finally, the fundamentals of Förster resonant energy transfer (FRET) between fluorescent dyes are given. The influence of AuNPs on the molecule's fluorescence decay rates, which, among other factors, defines the efficiency of FRET, is discussed.

2.1 Plasmonic properties of gold nanoparticles

2.1.1 Localized surface plasmons

Nanometer-sized spherical AuNPs strongly scatter and absorb in the green spectral range, which can be observed by the naked eye when investigating beakers containing suspensions of these nanoparticles in water. If one keeps such a beaker against the light, the solution appears red since the green part of the light is absorbed. If one puts an opaque material on the back side of the beaker and observes the scattering response, the solution appears green. The hydrosols of non-spherical AuNPs appear red to blue depending on the exact shape of the nanoparticles. This behavior suggests a resonant response of AuNPs to the incident electromagnetic radiation.

The reason for resonant response of AuNPs to incident light is the excitation of collective oscillations of conductive band electrons called localized surface plasmons. If an electromagnetic wave of suitable energy penetrates the nanoparticle, electrons are displaced from their positions. Coulomb attraction between positive ion cores and electrons provides the restoring force for this displacement and as a result the oscillation is induced. Apart from gold, localized surface plasmons are also present in silver and copper nanoparticles. In bulk noble metals localized plasmon oscillations are not observed since the penetration depth of the electromagnetic field into bulk metal is only some tens of nanometers in the visible range [24, 25]. Non-localized propagating surface plasmons are detected in noble metal thin films [26].

Interaction of nanoparticles with incident electromagnetic radiation can be described in terms of the quasi-static approximation [27, 28]. In this approximation plasmonic nanoparticle with a radius a much smaller than the excitation wavelength λ is considered as a point dipole. This implies that the phase of the applied field is constant over the nanoparticle's whole volume and the particle can be seen as situated in an electrostatic field. To find the potentials inside (Φ_{in}) and outside (Φ_{out}) of the particle, the Laplace equation $\nabla^2\Phi = 0$ is solved in r, θ coordinates for the nanoparticle's boundary conditions. The resulting expressions

for the potentials are [28]:

$$\Phi_{in} = -\frac{3\varepsilon_h}{\varepsilon + 2\varepsilon_h} E_0 r cos\theta \tag{2.1}$$

$$\Phi_{out} = -E_0 r cos\theta + \frac{\varepsilon - \varepsilon_h}{\varepsilon + 2\varepsilon_h} E_0 a^3 \frac{cos\theta}{r^2} \tag{2.2}$$

where ε is the dielectric function of the particle and ε_h is the dielectric function of the host (medium).

Introducing the dipole moment

$$\mathbf{p} = 4\pi\varepsilon_0\varepsilon_h a^3 \frac{\varepsilon - \varepsilon_h}{\varepsilon + 2\varepsilon_h} \mathbf{E_0} = \varepsilon_0\varepsilon_h \alpha \mathbf{E_0} \tag{2.3}$$

allows the nanoparticle's polarizability α to be defined as:

$$\alpha = 4\pi a^3 \frac{\varepsilon - \varepsilon_h}{\varepsilon + 2\varepsilon_h}. \tag{2.4}$$

As can be seen, the polarizability shows a resonant behavior with a maximum value at $|\varepsilon + 2\varepsilon_h|$=min.

To get further insight into the resonance conditions, one has to analyse the dielectric function of the material. The dielectric function of gold is a frequency-dependent complex value: $\varepsilon = Re[\varepsilon(\omega)] + Im[\varepsilon(\omega)]$. For slowly-varying or small $Im[\varepsilon]$ the resonant condition is simplified to $\Re[\varepsilon] = 2\varepsilon_h$. This expression is called the Fröhlich condition.

The simplest way to derive the dielectric function of a metal is the free-electron or Drude model [24]. In this model metal consists of positive ion cores and quasi-free non-interacting electrons characterized by the damping constant γ. The total response is calculated by solving the equation of motion for one electron and multiplying the response by the total number of electrons. The resulting expression for $\varepsilon(\omega)$ is:

$$\varepsilon(\omega) = \varepsilon_\infty - \frac{Ne^2}{\varepsilon_0 m_e} \frac{1}{\omega^2 + i\gamma\omega} = \varepsilon_\infty - \frac{\omega_p^2}{\omega^2 + i\gamma\omega} \tag{2.5}$$

where ε_∞ describes the contribution from positive ion cores, N is the density of free electrons and e and m_e are electron charge and mass, respectively. The quantity ω_p is called the plasma frequency and corresponds to the frequency at which the electromagnetic field starts to penetrate the metal.

In gold and other noble metals, visible light can induce not only excitation of electrons within the conduction band, but also the transition of electrons from lower bands to the conduction band. In this case the free-electron approximation fails, which is illustrated by the discrepancy between measured and calculated dielectric functions for noble metals in the visible range [28]. In practice ε derived from the free-electron model is used for calculations in the deep red and infrared range of the spectrum, while for the visible range the interpolated curve obtained from the experimental data in reference [29] is used.

The electric field inside and around the particle can be calculated from the potentials as $E = -\nabla\Phi$ [28]:

$$\mathbf{E_{in}} = \mathbf{E_0}\frac{3\varepsilon_h}{\varepsilon + 2\varepsilon_h} \tag{2.6}$$

$$\mathbf{E_{out}} = \mathbf{E_0} + \frac{3\mathbf{n}(\mathbf{n}\cdot\mathbf{p}) - \mathbf{p}}{4\pi\varepsilon_0\varepsilon_h}\frac{1}{r^3} \tag{2.7}$$

From these equations and recalling the expression for the dipole moment (Eq. 2.3), it can be seen that at the Fröhlich condition a resonant field enhancement inside and outside of the particle is observed. In this thesis a field enhancement around plasmonic particles is used to manipulate energy transfer between molecules attached to them.

2.1.2 Optical properties of gold nanoparticles

Plasmon oscillations in a nanoparticle result in photon emission at the resonant frequency, which can be experimentally detected as elastic scattering. The photon emission represents a radiative decay of plasmon oscillation. Simultaneously a nonradiative decay process takes place, resulting into the absorption of energy by the nanoparticle. Nonradiative decay occurs via Landau damping – the mechanism where the plasmon in the nanoparticle decays into an electron-hole pair

[30, 31]. Here both interband (within conduction band) and intraband (valence band to conduction band) transitions are possible. Excited electrons then thermalize with other conduction electrons changing the thermal distribution of the Fermi sea. Subsequently the energy is transferred to the volume of the particle by electron-phonon scattering and by scattering on defects or impurities. The absorption of light energy by a plasmonic nanoparticle determines its optothermal properties: by transferring the excess of energy to the surrounding medium the plasmonic nanoparticle performs as a highly localized heater.

Optical properties of AuNPs are characterized by scattering and absorption cross sections, C_{sca} and C_{abs}, which quantify the amount of scattered and absorbed light. Their sum is called the extinction cross section C_{ext}. Cross sections can be understood as apparent areas with which a nanoparticle gathers light, and they have a unit of area. Cross-sections, expressed through the dipolar polarizability, are written as

$$C_{sca} = \frac{k^4}{6\pi}|\alpha|^2 \tag{2.8}$$

$$C_{ext} = kIm[\alpha] \tag{2.9}$$

$$C_{abs} = C_{ext} - C_{sca} \tag{2.10}$$

where α is the polarizability calculated in the quasi-static approximation. At resonance frequencies extinction cross sections of plasmonic nanoparticles exceed their geometrical sizes so their absorption and scattering spectra show a peak at these frequencies. The peak position is determined by the real part of the dielectric function. It can also be largely influenced by the refractive index of the surrounding medium: an increase of the refractive index results in the redshift of the plasmonic peak, because the frequency of plasmonic oscillations decreases in the medium with higher polarizability. The width of the plasmonic peak is related to nonradiative decay and energy absorption and is described by the imaginary part of the dielectric function.

Although giving a good qualitative picture, the quasi-static approximation fails with the increase of the nanoparticle size. Namely, broadening and redshift of the plasmonic peak is observed, which is known as a retardation effect. The reason for this effect is that with the increase of the nanoparticle's size the field distribution

is not constant over the whole nanoparticle's volume [32], so to describe the field distribution correctly, not only dipolar order but also higher multipole orders have to be considered. The overview of the different theoretical methods to calculate the optical response of plasmonic nanoparticles precisely is given in reference [33].

In this thesis the Mie theory implemented in a commercial software MQMie is used to calculate the cross sections of AuNPs with diameters of 40 nm and 60 nm. In the Mie theory, Maxwell's equations are solved for spheres of known size and known dielectric function situated in homogeneous medium. The exact analytical solution is obtained for internal and external fields and for cross sections [27, 34]. The resulting expressions for the cross sections are

$$C_{sca} = \frac{2\pi}{k^2} \sum_{n=1}^{\infty} (2n+1)(|a_n|^2 + |b_n|^2) \tag{2.11}$$

$$C_{ext} = \frac{2\pi}{k^2} \sum_{n=1}^{\infty} (2n+1) Re[a_n + b_n] \tag{2.12}$$

where k is wave vector and a_n and b_n are Mie coefficients expressed in the following way:

$$a_n = \frac{m\psi_n(mx)\psi_n'(x) - \psi_n(x)\psi_n'(mx)}{m\psi_n(mx)\xi_n'(x) - \xi_n(x)\psi_n'(mx)} \tag{2.13}$$

$$b_n = \frac{\psi_n(mx)\psi_n'(x) - m\psi_n(x)\psi_n'(mx)}{\psi_n(mx)\xi_n'(x) - m\xi_n(x)\psi_n'(mx)}. \tag{2.14}$$

Here $m = \frac{\sqrt{\varepsilon}}{\sqrt{\varepsilon_h}}$ and ψ_n and ξ_n are Riccati-Bessel functions. Different numbers n describe multipole contributions, e.g. $n = 2$ corresponds to dipole. When considering only dipolar contributions one arrives back to the quasi-static limit.

Figure 2.1 shows the scattering and absorption spectra of spherical AuNPs of 40 and 60 nm size calculated with MQMie. One clearly sees the plasmon resonance both in absorption and scattering response. Also the change of relative intensity of scattering and absorption with size is observed: scattering originating from radiative decay becomes more prominent for larger particles.

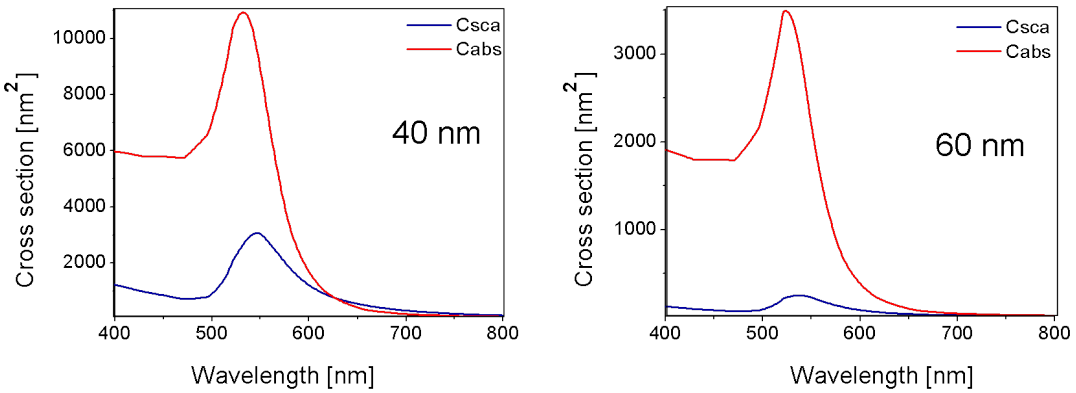

Figure 2.1: a) Calculated absorption (red) and scattering (blue) cross section of 40 nm AuNP in the visible range. b) Calculated absorption (red) and scattering (blue) cross section of 60 nm AuNP in the visible range.

2.1.3 Plasmonic coupling in gold nanoparticle dimers

Plasmonic dimers can be defined as a pair of plasmonic nanoparticles separated by a distance smaller than the nanoparticle's radius. In this arrangement the properties of the whole structure differ drastically from the properties of its isolated components. In the extinction spectra of such dimers, broadening of plasmonic peak or appearance of another peak that is redshifted in comparison to the original one is observed [35]. Moreover, it was reported that the field enhancement in the central region between two nanoparticles is larger than the sum of the field enhancement from each particle [36]. This region of extraordinary field enhancement is referred to as the "hot spot".

The change in the properties of dimer as compared to monomers originates from the coupling of plasmon oscillations [37]. When two nanoparticles are situated close enough, their fields are influenced by each other [38, 39]. There are two plasmonic modes in a dimers, each one giving rise to a peak in the extinction spectrum. Excitation of these modes has a polarization dependency: the transversal mode is excited with light polarized perpendicular to the dimer axis and the longitudinal mode is excited with light polarized along the dimer axis. This is schematically shown in Figure 2.2, where P indicates the direction of polarization of the incident field. For the longitudinal mode the individual particles

are situated in the enhanced fields of each other, so this mode can be excited with lower energy and redshift of the plasmonic peak is observed. Higher polarizability of the longitudinal mode leads to an increase of C_{ext}. The transversal mode, on the other hand, is slightly blue-shifted, however since this blue-shift is not prominent it almost coincides with a single-particle mode [37].

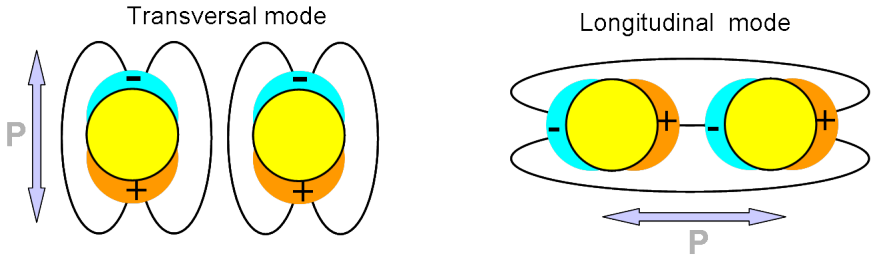

Figure 2.2: Transversal and longitudinal mode of plasmon coupling between two spherical nanoparticles of equal size. P indicates the polarization direction of the incident field

The difference in energy needed to excite two plasmonic modes in a dimers has strong dependence on the interparticle distance. The plasmonic near field is present only in the immediate vicinity of a nanoparticle, so with the increase of interparticle separation the interaction between fields of two nanoparticles rapidly vanishes. In reference [40] the dependence of plasmonic coupling on the separation between particles is exressed as:

$$\frac{\Delta\lambda}{\lambda_0} \approx k \cdot e^{\frac{-a}{0.2D}} \tag{2.15}$$

where $\frac{\Delta\lambda}{\lambda_0}$ is the plasmon shift normalized by the resonant wavelength of a single particle, a is the diameter of the particle and D is the interparticle distance.

In [17] distance-dependent plasmonic coupling is used to apply a plasmonic dimer as a resonator which selects particular transitions of a fluorescent molecule placed in the interparticle gap. Different interparticle distances result in enhancement of different modes, so a different shape of the molecule's fluorescence spectrum at different interparticle distances is observed.

In this thesis the cross sections of AuNP dimers are calculated with commercial software MQAggr. This sofware is based on Mie theory and reference [41] and considers interaction of all multipoles of the fields of both particles in a dimer. The expression used for the polarizability of dimers in this software is as follows [42]:

$$\alpha_{dimers} = \frac{2\alpha}{1 - F\left\{\frac{a}{2D}\right\}^3 \frac{\varepsilon - \varepsilon_h}{\varepsilon + 2\varepsilon_h}} \tag{2.16}$$

where F is a factor taking value 2 for longitudinal mode and -1 for the transversal mode.

2.2 Optical trapping of nanoparticles

When photons impinge on an object they exert force on it. An example for this effect from astronomy is a comet, whose two tails originate from dust and gas particles deflected by solar radiation. In case of light sources available on Earth, radiation pressure is as weak as several femtonewtons and cannot be recognized in the everyday life. That is why it was not untill the end of the last century that manipulation of micro and nanoobjects with tightly focused laser beams was discovered [43]. This method, called optical trapping (OT) or optical tweezing, is nowadays a well established touchless, noninvasive and effective manipulation tool on micro and nanoscale [44–47].

Optical trapping of nanoparticles can be described in terms of Lorentz force acting on a small object. The induced polarization on the particle is expressed as $\mathbf{p} = \varepsilon_0 \varepsilon_h \alpha \mathbf{E}$, where ε_0 and ε_h are dielectric constants of vacuum and of the medium (host), respectively, α is the complex polarizability of the particle, and $\mathbf{E}$ is an incident field. Proceeding by applying the vector equality to Maxwell's equations, and averaging the total force over one optical cycle, the optical force density is written as [25]:

$$< \mathbf{F}_{opt} >= \frac{\varepsilon_0 \varepsilon_h}{4} Re[\alpha] \nabla (\mathbf{E}^* \mathbf{E}) + \frac{\varepsilon_0 \varepsilon_h}{2} Im[\alpha] Im \left\{ \sum_i E_i^* \nabla E_i \right\} \tag{2.17}$$

Here * stands for complex conjugate, and i is an index accounting for $i = x, y, z$. From this expression it can be seen that the total optical force has two components corresponding to terms of the sum. The first term is called the gradient force:

$$< \mathbf{F}_{grad} >= \frac{\varepsilon_0 \varepsilon_h}{4} Re[\alpha] \nabla (\mathbf{E}^* \mathbf{E}) \tag{2.18}$$

The gradient force is acting towards the region of the highest intensity, which for a focused Gaussian beam corresponds to the beam waist. Control of the gradient force is achieved by tightening the focus of the trapping laser. In practice objectives with high numerical aperture are used for trapping since they provide the strongest focusing.

The second term in equation 2.17 is called the scattering force:

$$< \mathbf{F}_{scat} >= \frac{\varepsilon_0 \varepsilon_h}{2} Im[\alpha] Im \left\{ \sum_j E_j^* \nabla E_j \right\} = \frac{\sqrt{\varepsilon_h}}{c} (C_{sca} + C_{abs}) < \mathbf{S} > \tag{2.19}$$

Here $< \mathbf{S} >= \frac{1}{2} Re(\mathbf{E} \times \mathbf{H}^*)$ is the Poynting vector, averaged over one optical cycle, $\mathbf{H}$ stands for magnetic field; c is speed of light and C_{sca} and C_{abs} are scattering and absorption cross sections of the particle, respectively. The scattering force is acting in the direction of the beam propagation and increases with the power of the trapping laser. The scattering force diminishes the action of the gradient force by pushing the object out of the focal point. In other words, to trap the object in three dimensions conditions under which the gradient force overcomes the scattering force are required. If the scattering force prevails, only manipulation in two dimensions may be possible while in the third dimension the particle is mechanically confined by the underlying surface. If the laser is focused on the surface and the laser power is increased the particle is positioned on the surface; this effect is known as laser printing [48].

From 2.17 it can be seen that the gradient force depends on the real part of the polarizability $Re[\alpha]$ and the scattering force depends on its imaginary part $Im[\alpha]$. For AuNPs of 60 nm the maximum of $Re[\alpha]$ is at $\sim$ 560 nm and the maximum of $Im[\alpha]$ is at $\sim$ 540 nm [25]. Towards the longer wavelengths $Re[\alpha]$ slowly decays while the decay of $Im[\alpha]$ is much faster. This means that if

linearly-polarized trapping laser is tuned to the deep-red or infrared region, the $F_{grad} \sim Re[\alpha]$ overcomes the $F_{scat} \sim Im[\alpha]$ providing stable optical trapping in three dimensions.

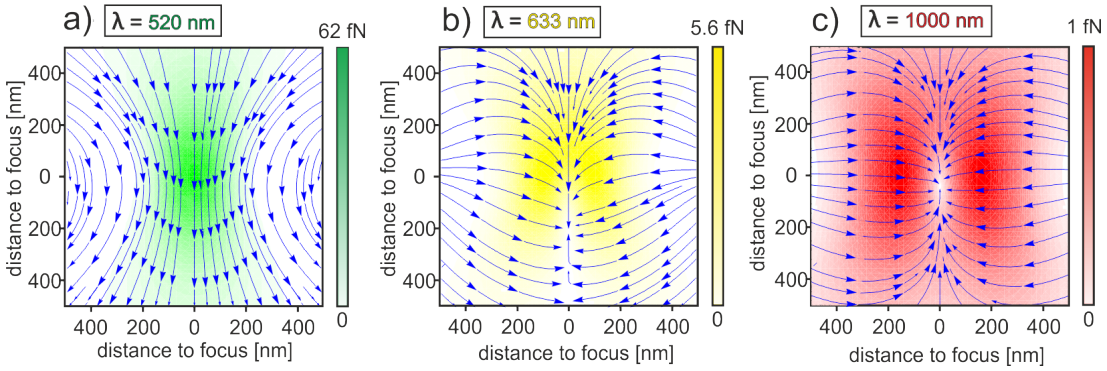

Figure 2.3: Calculation of the optical force acting on 60 nm AuNP in water at wavelengths of the trapping laser of a) 520, b) 633 and c) 1000 nm. The laser power on the sample is 100 mW. Arrows show the directions of the force. Direction of beam propagtion is from the top to the bottom of the box.

In Figure 2.3 the calculations for the total optical force acting on 60 nm AuNP in water at three different trapping wavelengths are shown. Calculations were performed based on references [25, 49, 50]. For each wavelength the laser power on the sample is 100 mW. Laser light is propagating from the top to the bottom of the box. Arrows show the direction of optical force. If the trapping laser is operating at 520 nm (panel a), which is close to the optical resonance of the trapped particle, $F_{scat} > F_{grad}$ since $Im[\alpha] > Re[\alpha]$. As a result the particle is driven out of the focus of the trapping laser. If the trapping laser operates at 1000 nm (see panel c), which is redshifted compared to the plasmon resonance of the particle, $F_{scat} < F_{grad}$ since $Re[\alpha] > Im[\alpha]$ and the particle is attracted to the focus. In this case stable confinement in three dimensions is observed. Trapping at 633 nm represents an intermediate case where both forces contribute in a complex way and two-dimensional trapping is possible, see panel b of Figure 2.3.

In this thesis optical trapping with an infrared laser is used to manipulate single 60 nm AuNPs and to bring two AuNPs close to each other to investigate their interaction on a single-pair level.

2.3 DNA in solution and on gold nanoparticles

2.3.1 DNA and formation of double helix

Nucleic acid molecules encode all the life diversity present on Earth and yet have a very simple structure. Deoxyribonucleic acid (DNA) consists of only five chemical elements – hydrogen, oxygen, nitrogen, carbon and phosphorus. These elements are assembled into repeating building blocks called nucleotides. Only four different nucleotides exist (the fifth is found in ribonucleic acid - RNA).

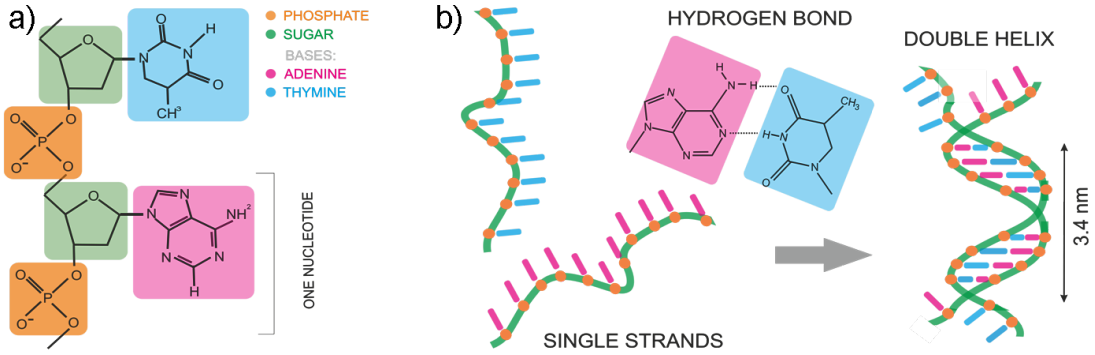

Figure 2.4: Structure of DNA. Phosphate group is shown in orange, sugar is shown in green and bases adenine and thymine are shown in pink and blue respectively. Bases guanine and cytosine are not considered in this example. a) Schematic of the chemical structure of the nucleotide chain consisting of two nucleotides with adenine and thymine bases; b) Cartoon showing the hybridization of two single DNA strands each consisting of repeating adenine and thymine units. The hydrogen bonds between two complementary bases are shown in the inset.

The structure of one DNA chain, also called single stranded DNA (ssDNA), is shown in Figure 2.4a. Each nucleotide consists of a phosphate unit shown in orange, sugar (deoxyribose) shown in green, and a nucleobase shown in blue or

pink depending on type. Combination of interchanging phosphate and sugar units is responsible for the polymer's stiffness, therefore it is called a DNA's backbone. Phosphate units are negatively charged, which results in the negative charge of the whole polymer chain. All the deoxyribose units in one ssDNA are oriented in the same way giving direction to the strand. Two different DNA ends are referred to as 3' and 5' ends, the numbers corresponding to the nominal numbers of carbon atoms in the deoxyribose unit.

The nucleotides can attach to each other in any order forming long linear polymer chains - polynucleotides. The sequence in which the nucleotides are assembled into polynucleotide sets a specific code, which defines the diversity in structure and functions of all living organisms. Oligonucleotides, DNA chains consisting of only several tens of nucleotides, can be synthesized in the lab and serve as good model systems to study the properties of the natural DNA polymers.

Nucleobases, aromatic cyclic structures situated along the backbone and connected to it covalently, define the differences between nucleotides and are responsible for carrying the genetic information. The four types of nucleobases are: adenine (A), thymine (T), guanine (G) and cytosine (C). The chemical structure of A and T is shown in Figure 2.4. In this thesis the DNA strands composed of only A and T units are considered.

If two ssDNA approach each other under suitable conditions, the bases of the strands connect by hydrogen bonds forming a double strand (dsDNA), see Figure 2.4b. While ssDNA are flexible chains attaining different shapes in solution (the configuration referred to as a random coil), dsDNA are stiff compact structures of a well-defined shape. This shape is frequently described as a twisted ladder [51], where two strands are connected antiparallel (3' ends attach to the 5' ends) and are coiled around a common axis. The helix makes a turn every 3.4 nm. The backbones of two strands are situated on the outside and the paired bases are situated inside of the double helix. The discoverers of DNA's double stranded configuration Watson and Crick found that the four bases can form only two pairs: A only binds to T while G only binds to C [52]. These bases are called complementary and the pairs they form are called Watson-Crick pairs.

There are two hydrogen bonds formed in an A-T pair and the number of hydrogen bonds in the C-G pair is three, making this connection stronger. The

most stable connection occurs between two strands with two completely complementary sequences, while mismatches destabilize the double helix. In addition to the hydrogen bonds, hydrophobic and electrostatic interactions between bases situated next to each other also contribute to the stability of the double strand. These interactions are called base-stacking.

Single DNA chains can also self-hybridize if they have complementary stretches within the structure. In this case the molecule bends over itself and complementary stretches attach. The part of the molecule between these complementary stretches is then forming a secondary structure called a loop or a hairpin [53].

Kinetics of DNA hybridization is a complex issue. Generally, reactions between biomolecules can be described by the first passage time theory developed in [54]. In this approach the interactions between different parts of biological macromolecules are considered to be diffusion-controlled. The intramolecular diffusion rates are calculated and the time needed for two reactive groups situated at some distance apart to collide and react is deduced. This theory was applied to study the formation of hairpin by single DNA strands, and the dynamics of the ssDNA attached to DNA double strands (a structure called dsDNA with a dangling end), as well as for the investigations of other biomolecules like proteins [55–57].

The formation of a double strand by two ssDNA molecules of different types can be seen as a bimolecular reaction (a reaction where two molecules take part) of the form $SS_1 + SS_2 \rightleftharpoons DS$. This reaction is of the second order, which means that reaction rates k depend on the concentration of both reagents in solution: $\frac{d[DS]}{dt} = k[SS_1][SS_2]$, where square brackets stand for concentration. A bimolecular reaction of second order is a two-states-one-step process: two separate species assemble into a complex in one single step.

Reaction rates of most of chemical reactions depend on temperature. Namely, the increase in temperature leads to the increase in frequency of collisions as well as to the increase of amount of molecules with energies large enough for the reaction to occur. Quantitatively the temperature dependence of the reaction rate is described by the Arrhenius equation: $k = Ae^{-E_a/k_BT}$. Here A is the frequency constant describing intermolecular collision, also called as Arrhenius constant, E_a is the activation energy of the reaction, k_B is the Boltzman constant and T is the temperature. k values can be determined experimentally, so if one takes the

logarithm of the Arrheius equation and plots ln k versus $\frac{1}{T}$, the value of E_a can be deduced from the slope of the graph. For conventional chemical reactions E_a values are positive. However for the association of two ssDNA, apparent negative E_a values corresponding to the decrease of the reaction rates with increase in temperature are sometimes reported [57–59]. The term "apparent" should be used since the negative values of E_a are unphysical.

Apparent negative activation energies can be explained by the presence of an intermediate step present in the binding reaction so that the reaction is not of two-states-one-step type [58, 60]. In other words, for successful hybridization the formation of a so-called nucleus consisting of several basepairs is required. There is a critical size of the nucleus, and if the amount of hybridized bases at a certain stage of interaction is smaller, the dissociation back to single strands will be observed. Only if the amount of hybridized basepairs is sufficient is "zipping" to the fully hybridized state expected.

It should be mentioned that in some cases positive activation energies corresponding to the acceleration of DNA binding with temperature were also reported [61, 62]. Authors in [61] point out the large influence of the exact sequences of bases in the interacting strands on the E_a values. Authors in [63] suggest that negative E_a values observed at high temperatures change to positive values if the temperature is lowered.

While kinetics of DNA hybridization is not fully clarified yet, the thermodynamics of this process is well described. The developed thermodynamic theory for DNA hybridization allows for modeling of interaction between two DNA strands of arbitrary sequences and lengths at different experimental conditions. This theory is described in the next subsection.

2.3.2 Defining DNA melting temperature

As mentioned above, two strands are assembled into a double helix by hydrogen bonds which form between complementary nucleobases as well as by the base stacking. These interactions are weak, so the hybridization of DNA is a reversible process. Generally speaking, at any moment molecules in both unhybridized and hybridized states are present in the mixture of complementary DNA strands

in solution. The concentration of either state can be tuned by, for example, changing the salt (NaCl) content and pH [64, 65]. By increasing the amount of Na^+ ions, which screen the charges of phosphate groups, the repulsion between single strands is suppressed and binding is promoted. Extreme pH values hinder binding due to the excessive pro- or deprotonation of the DNA strands.

The temperature of the solution also has an effect on the hydrogen bonding between complementary bases and on the hydrophobic interactions in base stacking. High temperatures result in an increase of kinetic energy of the molecules and as a result bonding is destabilized, leading to the dissociation of strands. The temperature at which hybridized and unhybridized states are present at equal concentration is called the melting temperature T_m. Common experimental methods to measure T_m are based on the difference in light absorption of ss and dsDNA in the ultraviolet. By plotting the absorption of the sample at a particular wavelength versus temperature one obtains a curve of sigmoid shape called the melting curve. The maximum of the first derivative of the melting curve gives the exact T_m value.

Melting temperature can be also predicted theoretically. The expression for T_m is derived according to [66]. Combining thermodynamic equations $\Delta G_N = \Delta H_N - T\Delta S_N$ and $\Delta G = -RT\ln(K_c)$ one gets $T = \frac{\Delta H}{\Delta S - R\ln(K_c)}$. Here ΔG_N, ΔH_N and ΔS_N are respectively Gibbs free energy, enthalpy and entropy of the hybridization of N bases and R is the molar gas constant. K is an equilibrium constant of duplex formation, $K = \frac{2f}{(1-f)^2 c}$, where f is a fraction of hybridized bases and c is the total concentration of strands. At T_m , $f = 1/2$ and with this the expression for T_m in Celsius becomes

$$T_m = \frac{\Delta H_N}{\Delta S_N + R\ln\left(\frac{c}{4}\right)} - 273.15 \tag{2.20}$$

For the mixture of strands of different concentrations $c/4$ should be substituted by $[SS_1] - \frac{[SS_2]}{2}$, and for the self-complementary strands it should be substituted by c [66, 67].

Since the concentration of strands is a known number, defining the values of entropy and enthalpy remains the only challenge. For finding these values the

nearest neighbor model may be used, which was developed in the second half of the last century [68, 69]. The key point of this model is to calculate ΔH_N and ΔS_N of two interacting strands of sequences $X_1X_2...X_N$ and $Y_1Y_2...Y_N$ as following:

$$\Delta H_N = H[X_1Y_{1/init}] + H[X_1X_2/Y_1Y_2] + H[X_2X_3/Y_2Y_3] + ... + H[X_NY_{N/init}], \tag{2.21}$$

$$\Delta S_N = S[X_1Y_{1/init}] + S[X_1X_2/Y_1Y_2] + S[X_2X_3/Y_2Y_3] + ... + S[X_NY_{N/init}]. \tag{2.22}$$

Here $H[X_iY_{i/init}]$ and $S[X_iY_{i/init}]$ with $i = 1$ or N are the enthalpy and entropy of the initiation of connection. The other terms are the enthalpy and entropy of connection of neighboring pairs. At preserved experimental settings all the terms are constants. Their values were measured at different conditions [70–73] and then summarized and unified for the NaCl concentration of 1 M [67]. For the corrections of the T_m values at salt concentrations other than 1 M the following expression suggested in reference [67] should be used:

$$\Delta S_{corrected} = \Delta S_{1MNaCl} + 0.368 \cdot N \cdot ln([Na^+]) \tag{2.23}$$

where N is the number of nucleotide pairs in the strand and $[Na^+]$ is the concentration of Na^+ ions.

To summarise, the nearest neighbor model can be applied for the calculation of T_m for the systems of ssDNA of any length, composition and at different salt concentrations. In this thesis the modified formula for T_m was used to calculate the melting temperature of DNA strands attached to gold nanoparticles. The insight into this hybrid system is given in the following subsection.

2.3.3 DNA attached to gold nanoparticles

AuNPs have very distinctive optical and optothermal properties, originating from their plasmon resonances, but are chemically rather inert. They are therefore good candidates to be connected to DNA strands to serve as carriers, markers and heaters [12, 74–76]. Following this idea, diverse AuNP/DNA hybrid systems were prepared, from single particles to extended aggregates [18, 77–79]. These

were successfully used in different detection and sensing applications [80–84]. Considering these recent advances, the studies of DNA interactions on the surface of AuNPs are of high interest.

DNA can be connected to gold surfaces either by electrostatic or by thiol bonds, referred to as semi-covalent or dative bonds [85]. In case of attachment via thiol bond, 3' or 5' end of a DNA strand is functionalized with an -SH group, which has high affinity to gold. The thiol bond between DNA and gold is very stable – to break it high laser powers are required, which result in particle re-shaping [87, 88]. By tuning the DNA coverage density the configuration of strands on the surface can be controlled [86]. At high densities the molecules are oriented perpendicular to the surface with segments of molecules closest to the surface completely stretched. The remote parts of the molecule attain random coil configuration so that the ends of ssDNA are freely hanging from the particle and can interact with other species present in solution. Due to the negative charge of the DNA strands and high density of coverage the colloid of these hybrid particles is stabilized both electrostatically and sterically. Particles are usually dispersed in common biological buffers.

C. Mirkin and co-workers were the first to assemble single DNA-functionalized AuNPs of two types into extended aggregates [18]. This was done by adding a DNA linker to solution – a free DNA chain, which is partially complementary to strands of both types. The same group suggested to use an optical response of AuNPs for the T_m measurements [89]. This idea is elegant and simple: if upon hybridization AuNPs are brought closer than the particle's radius, plasmon oscillations of individual particles couple leading to a redshift of the peak of the extinction spectrum of the sample. Upon the dissociation of DNA chains at $T > T_m$, the reversed change of the extinction spectrum is observed. Plotting the optical response at one of the resonances versus temperature one obtains a T_m curve. In this study the bulk heating of the whole sample is done and AuNPs are used only as optical markers. The authors in [19] propose an important improvement for this technique, namely they suggest to use plasmonic properties of AuNPs to locally heat the dsDNA attached to them. When a plasmonic particle is excited by laser light the absorbed energy is converted into heat, resulting in a

local temperature increase and the dehybridization of the DNA strands near the particle's surface, so that no global heating is required any more.

Studies of DNA hybridization on a planar surface show that it differs from the hybridization of free DNA chains in solution, with both stronger and weaker interchain binding being reported [90–92]. In the case of hybridized DNA in AuNP aggregates, sharper melting transitions were observed [18]. The reason for this behavior is cooperatively originating from multiple binding. More insights into the factors influencing the T_m of DNA in AuNP aggregates can be found in [93], where the influence of the interparticle distance, salt concentration, DNA coverage and other effects on T_m of the system are addressed. In [94] and [63] the thermodynamics of hybridization of free ssDNA strands with complementary ssDNA attached to AuNPs is studied in detail. The authors show that in this case T_m of the system is lower compared to the T_m of the corresponding free chains in bulk. This effect is attributed to the destabilization of the connection between strands by competitive attraction to the gold surface.

All the studies mentioned above are ensemble measurements conducted in bulk. In [95] binding of two single dielectric microparticles covered with DNA is investigated. The interaction potential is deduced from the change of positions of particles confined in the focus of optical trap. No studies combining optical manipulation, optical heating and optical detection of DNA hybridization process are reported so far.

In this thesis, the specific binding of DNA-coated AuNPs manipulated by light is studied for the first time on a single-particle level. Moreover, by changing the experimental conditions, the kinetics of particle binding is tuned via plasmonic heating.

2.4 Fluorescent dyes near gold nanoparticles

2.4.1 Fluorescence and Förster Resonance Energy Transfer

Fluorescence is emission of photons by a molecule or other species driven to the excited electronic state due to interaction with incident light. The typical timescales of fluorescence are on the order of 10^{-8} s. Sometimes the more general

term photoluminescence (PL) is used although this also includes phosphorescence – an emission from the quantum mechanically forbidden states with timescales on the order of milliseconds to minutes. Good introduction into fluorescence can be found in the reference [96].

The most famous for showing fluorescence are organic molecules having aromatic rings in their structure. Fluorescence is also detected from semiconductor nanocrystals called quantum dots and from metallic nanoparticles [97, 98]. In this section we focus on fluorescent organic molecules, which are referred to as fluorophores or dyes.

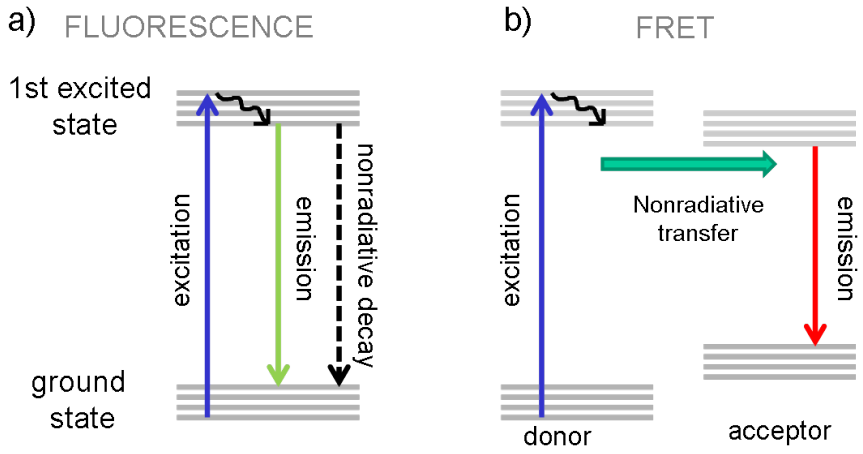

Figure 2.5: The processes of (a) fluorescence and (b) FRET shown as a Jablonski diagram.

In molecules the transition to the excited electronic state occurs via the absorption of a photon with suitable energy. The emitted photon has lower energy than the photon, which was absorbed. The reason for this difference, called a Stokes shift, lies in the fine structure of energy levels of a molecule. This structure is shown in Figure 2.5 in the form of a Jablonski diagram. Every electronic energy level has a distribution of vibrational levels associated with it. The molecule, which is driven to the higher vibrational level of the excited electronic state, first relaxes to the lowest vibrational level of the first electronic excited state by dissipation of the excess of vibrational energy. After this relaxation to one of the vibrational states of the ground state by spontaneous emission of a photon can

occur. The fine structure of energy levels also explains the fact that fluorescence spectra of molecules are a continuum and do not appear as single lines.

A fluorophore's absorption is characterized by the absorption cross section C_{abs}, and its emission is characterized by the average lifetime τ. Average lifetime is defined as the time the molecule needs to decay to the ground state. The inverted quantity $\Gamma = \tau^{-1}$ is called the decay rate. The relaxation to the ground state can occur not only via the spontaneous emission of a photon but also via nonradiative decay. Therefore two different decay rates, Γ_{rad} and Γ_{nonrad} exist, and the joint decay rate is the sum of them. The values of both decay rates are defined by the intrinsic properties of the emitting molecule.

From the decay rates another important characteristics of a fluorophore can be derived: the fluorescence efficiency. The fluorescence efficiency also called the quantum yield QY is a ratio of the radiative decay rate to the joint decay rate:

$$QY = \frac{\Gamma_{rad}}{\Gamma_{rad} + \Gamma_{nonrad}} \tag{2.24}$$

The fluorescence quantum yield can be decreased due to a process called quenching. In this case additional nonradiative decay rates enter the denominator in the expression for the quantum yield. Consequently the average total fluorescent lifetime decreases. Quenching can be a result of interaction of molecule with a solvent, of an excited state chemical reaction or a result of energy transfer from the fluorophore to another object.

Förster resonant energy transfer (FRET) is one of the possible energy transfer mechanisms and occurs without emission of a photon. The molecule which transfers energy is called a donor and the molecule to which energy is transfered is called an acceptor. FRET can take place between two fluorophores, between a fluorophore and a non-fluorescent molecule, between a fluorophore and a quantum dot or between two quantum dots. When the donor is excited, the fluorescent acceptor will emit as a result of FRET. A detailed explanation of the FRET process is given in references [96] and [99].

Commonly FRET rates and efficiencies are described by the Förster theory [100]. In this theory Coulomb mediated charge interaction, which lies in the origin of FRET, is treated as interaction between two point dipoles representing

both fluorophores. The FRET rate k_{FRET} is expressed as

$$k_{FRET} = \frac{QY_D\kappa^2}{\tau_D R^6}\left(\frac{9000(ln10)}{128\pi^5 N_A n^4}\right)\int_0^\infty \mathrm{F_D}(\lambda)\varepsilon_\mathrm{A}(\lambda)\lambda^4\,\mathrm{d}\lambda = \frac{1}{\tau_D}\left(\frac{R_0}{R}\right)^6 \quad (2.25)$$

Here QY_D is the donor quantum yield, τ_D is the donor lifetime, R is the distance between donor and acceptor, κ^2 is an orientation factor, $F_D(\lambda)$ is the donor fluorescence spectrum with λ being the wavelength, ε_A is the acceptor molar extinction spectrum, n is the refractive index of the medium and N_A is Avogadro number. R_0 is called a Förster radius - the distance between donor and aceptor at which the probabiliy of FRET is equal to the probabity of donor radiative decay. In this formula all the quantities of the donor are given in the absence of an acceptor.

The orientational factor is expresed as $\kappa^2 = (cos\theta_{DA} - 3cos\theta_D cos\theta_A)^2$, where θ_{DA} is an angle between transition dipole moments of the donor and acceptor, and θ_A and θ_D are angles between the transition dipole moment of the acceptor and donor, respectively, and the distance vector between them.

From this formula the requirements for successful FRET can be extracted. First, the emission spectrum of a donor and the excitation spectrum of an acceptor should overlap. Additionally, due to the $\frac{1}{R^6}$ dependence of the FRET rate, the distance between the molecules should be sufficiently small to observe FRET. Finally, the dipoles of the donor and of the acceptor should not be situated perpendicularly.

FRET efficiency is defined as

$$E = 1 - \frac{\tau_{DA}}{\tau_D} = \frac{1}{1 + (\frac{R}{R_0})^6} \quad (2.26)$$

Normally FRET efficiency is manipulated as suggested by the Förster theory: a donor and acceptor with overlapping spectra are chosen and the distance between them is decreased.

2.4.2 Modification of decay rates near gold nanoparticles

Before focusing on the change of FRET near plasmonic structures we discuss the influence of plasmonic structures on the behavior of single fluorescent species. Studies of radiative and nonradiative rates of fluorescent species in the vicinity of plasmonic stuructures show that the interactions in these systems are very subtle and the change in rates depends on many factors. Experimentally both the enhancement [101–105] and decrease [106–108] of fluorescence in the vicinity of plasmonic nanostructures are observed.

In references [109, 110] the emission of a fluorescent species near a metal nanoparticle is expressed as a product of excitation in the presence of metal Γ'_{exc} and metal-modified quantum yield QY':

$$\Gamma'_{emiss} = \Gamma'_{exc} \cdot QY' = \Gamma'_{exc} \cdot \frac{\Gamma'_{rad}}{\Gamma'_{rad} + \Gamma'_{nonrad}} \tag{2.27}$$

Here Γ'_{rad} is a metal-modified intrinsic radiative rate. Γ'_{nonrad} is a metal-modified nonradiative rate, which includes all decay channels other than photon emission.The authors suggest to treat the change of fluorescence as a result of competition between several effects. Depending on which effects prevail, both fluorescence enhancement and decrease can be observed.

If the dipole of the emitting molecule is oriented tangentially to the surface of the particle, destructive interference between the dipoles takes place and the Γ'_{rad} of the dye is decreased [111, 112]. Also, the decrease of fluorescence emission in the presence of metal nanoparticles can be attributed to the FRET process taking place between the excited fluorophore and a metal nanoparticle in its vicinity. In this case the electromagnetic energy of the fluorophore is transferred to the plasmon oscillation of the nanoparticle, which leads to high Γ_{nonrad}. Like in the case of fluorophore-fluorophore FRET, the distance between the dye and the plasmonic particle plays an important role. This means that the dyes situated directly on the surface will suffer from substantial quenching. On the contrary to fluorophore-fluorophore FRET, no dependence on the relative orientation between the molecule's and the nanoparticle's dipole for FRET between molecule and nanoparticle is found [113].

The increase of the fluorescence emission in the presence of AuNPs is assigned to two factors. One factor is the increase of the incident field arising from the plasmon oscillations, which leads to the increase in Γ'_{exc}. Another factor is the increase in the radiative rate of the dye. This effect can be expected if the dipole moment of the molecule is situated radially towards the particle's surface resulting into the constructive interference of their dipole fields [114, 115].

Considering these findings it should be expected that FRET between donor and acceptor influenced by gold nanoparticles situated in the vicinity is a very complex process. In [116] authors theoretically consider a prolate solid state particle, which is situated near a FRET pair and expand the Förster theory for this case. The authors calculate energy transfer rates k_{FRET} for different positions of donor and acceptor. They predict the enhancement of FRET for the case when the transition frequency coincides with a resonant frequency of the solid particle, but simultaneously point out the competing damping processes, which could result in the overall decrease of FRET. In [117] the increase in FRET efficiency and FRET distance for fluorescent dyes incorporated into dielectric shell around single silver nanopshere is shown. Authors in [118] report the increase of FRET efficiencies in the presence of silver nanoislands. Also enhancement of FRET between two quantum dots in the presence of plasmonic nanoparticles is reported [20].

In [119] authors provide general theoretical treatment of any Coulomb-mediated interaction (including FRET) taking place near plasmonic nanosystem. They show that in the vicinity of plasmonic metal nanostructures FRET is governed not by the bare interaction potential but by the plasmon-dressed or renormalized one. The plasmon-dressed interaction potential includes the bare interaction potential and shows resonant frequency dependence:

$$W(\mathbf{r}, \mathbf{r}'; \omega) = V(\mathbf{r} - \mathbf{r}') + \frac{4\pi}{\varepsilon_h} G^r(\mathbf{r}, \mathbf{r}'; \omega). \tag{2.28}$$

Here $\mathbf{r}$ and $\mathbf{r}'$ are coordinates of interacting charges, $V(\mathbf{r} - \mathbf{r}')$ is the bare interaction potential and ω is the resonant frequency. Using quantum mechanical treatment the authors derive the expression for the plasmon-enhanced FRET rate and show that plasmon-mediated FRET has a longer range (expanding over the whole nanoparticle) compared to regular FRET. These findings turn plasmonic

nanostructures into good candidates to manipulate FRET beyond the the Förster theory.

While single AuNPs provide high field enhancement due to their localized surface plasmon resonance, dimers of AuNPs can host coupled plasmon resonances, as explained in Section 2.1. This plasmonic coupling results in highly enhanced fields localized in the central region between particles. Therefore the dimer configuration may have a different impact on FRET between molecules attached to the surface in comparison to the influence of monomers.

In this thesis the FRET process between molecules situated in the inter-particle region of AuNP dimers is investigated for the first time. The performance of AuNP dimers and monomers for modification of FRET rates and efficiencies is compared by measuring the fluorescence lifetimes of donor and acceptor in different configurations.

3 Preparation of samples and experimental setups

AuNPs can be synthesized by a variety of methods including both top-down (wet chemistry) and bottom-up (lithography, laser ablation) approaches [120]. The most popular method, however, is a wet chemistry technique since it provides very good shape and size homogeneity [121, 122]. Spherical nanoparticles of high quality and with diverse surface chemistry are available commercially. The synthesis of non-spherical shapes such as nanostars is more challenging and is normally performed only in research laboratories [123–125].

(Bio)molecules attached to AuNPs play multiple roles. Due to electrostatic (in the case of charged molecules) or steric (in the case of branched and long polymers) stabilization mechanisms molecules on the surface can prevent aggregation of the colloid. Also they can be used as linkers to assemble single nanoparticles into bigger structures. Moreover, (bio)molecules can serve as analytes to probe the performance of AuNPs. All of these functions are used in this work.

In this chapter the properties of AuNPs and (bio)molecules decorating their surface are described. The molecular interactions used to connect AuNPs are explained and the protocol for AuNP dimer formation in bulk is given. Further the methods to characterize the properties of single nanoparticles and their aggregates are discussed, namely electron microscopy and the dark-field mode of optical microscopy. The optical trapping technique combined with dark-field microscopy to detect and to move single AuNPs is introduced. Also the spectroscopic methods used to investigate the optical properties of AuNPs and hybrid systems containing AuNPs and organic molecules are described.

3.1 Biofunctionalized gold nanoparticles

In this thesis spherical nanoparticles of ∼60 nm diameter and of ∼40 nm diameter as well as star-shaped nanoparticles with a core diameter of ∼100 nm were used. Below details about these nanoparticles and DNA, proteins and other organic molecules decorating their surface are given. Also, the mechanisms employed to modify the nanoparticle's surface and to assemble nanoparticles into aggregates are explained.

Unfunctionalized citrate-stabilized AuNPs of ∼60 nm diameter were purchased from British Biocell International, UK. According to the information provided, the nanoparticles are produced by one of the metal salt reduction methods. The surface coverage of the particles with citrate molecules indicates variation of the Turkevich method [126]. In this method an aqueous solution of gold precursor chloroauric acid $HAuCl_4$ is mixed with sodium citrate $Na_3C_6H_5O_7$ and the temperature of the solution is increased. Citrate reduces Au^{3+} ions to Au^0 followed by the growth of spherical AuNPs with a face-centered cubic crystalline phase. Simultaneously, the citrate molecules serve as a capping agent forming a negatively charged AuNP surface. As such, AuNPs repel each other providing stability to the bulk colloid in Mili-Q water or common buffers.

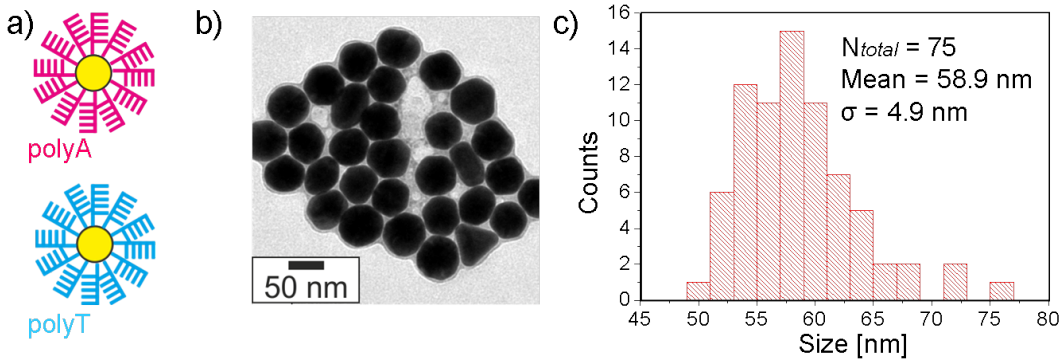

Figure 3.1: DNA-functionalized AuNPs of ∼60 nm size. (a) Schematic representation of the A-type and T-type particles. (b) Transmission electron microscope images of the A-type particles. (c) Statistics on the size distribution of the A-type particles. Adapted from [153]

DNA-functionalized AuNPs of ∼60 nm are provided by GNA Biosolutions GmbH, Germany. The nanoparticles are dispersed in a modified phosphate buffer saline (PBS) from the same company. Functionalization with single-stranded DNA (ssDNA) is performed according to [127]. In brief, DNA single strands (ssDNA) terminated with a thiol group on one end are connected to the surface of AuNP via a semi-covalent thiol-gold bond. Two types of ssDNA chains are used for functionalization: one consisting of repeating adenine units (poly-A) and another consisting of repeating thymine units (poly-T). Two batches of AuNPs are prepared, each functionalized either exclusively with poly-A chains (A-type AuNPs) or with poly-T chains (T-type AuNPs). Poly-A chains contain 25 bases of adenine and poly-T chains contain 24 bases of thymine. Considering the inter-base distance of 0.34 nm, the length of the poly-A chain is 8.5 nm and the length of the poly-T chain is 8.2 nm. Each particle has ∼ 1500 ssDNA distributed over its surface so that the molecules densely cover the nanoparticles.

DNA single strands are negatively charged resulting in an electrostatically stabilized colloid. Additionally, the colloid is stabilized sterically due to the dense coverage with DNA oligomers. Dense coverage is further required to prevent "curling" of DNA molecules around the AuNP due to the unspecific interaction of ssDNA with the surface [86]. At the coverage densities used in this thesis the strands are close enough to repel each other and are therefore situated perpendicular to the nanoparticle's surface. In this configuration DNA ends are free to interact with other molecules if those are present in solution. Figure 3.1a shows a schematic representation of the A-type and T-type particles. Panel b of the same figure shows a transmission electron microscope (TEM) image of the A-type particles. Statistics of the size distribution of A-type particles is shown in panel c. The average particle size is 58.9 nm with the standard deviation of 4.9 nm. The size distribution is not dependent on the functionalization so a similar result for T-type particles can be expected.

Interactions between complementary DNA strands can be used to prepare AuNP aggregates. If A-type and T-type AuNPs are brought into close vicinity to each other, poly-A chains hybridize with complementary poly-T chains and double stranded DNA (dsDNA) connecting two nanoparticles is created. According to the hybridization of A-type and T-type AuNPs in bulk performed by

GNA Biosolutions GmbH using the method reported in [19], particles hybridize at NaCl concentrations of 50-500 mM at temperature below 56^o C. At NaCl concentrations below 50 mM the electrostatic repulsion between the nanoparticles is too strong so that no aggregation is observed. At NaCl concentrations larger than 500 mM the electrostatic repulsion is too weak, and particle aggregation is no longer governed by chemical affinity and becomes unspecific.

Another type of biomolecular interaction exploited in this work is biotin-streptavidin binding. Biotin is a small organic molecule belonging to the vitamins of group B [128]. Biotin has a molar mass of 244.31 g/mol and its chemical formula is $C_{10}H_{16}N_2O_3S$. Streptavidin, on the other hand, is a protein consisting of four tetramers. It has a molar mass of $\sim$ 60000 g/mol [129] and a size of around 5 nm^3 [130]. Each of the four streptavidin subunits has a "pocket" in its structure where the biotin molecule is "docked" when approaching (see the cartoon in Figure 3.3). Five hydrogen bonds are formed between the ureido ring of biotin and the amino acid residues of streptavidin; also hydrophobic interaction and structural changes of the streptavidin molecule contribute to the binding [131]. Taken all together, this results in a very strong connection with an association constant K_a on the order of 10^{15}.

Although the biotin-streptavidin binding is non-covalent, the strength of it is comparable to covalent bonds. As such, the biotin-streptavidin complex survives a large variety of pH conditions and temperatures up to 70^0C [132]. In this thesis the advantage of the biotin-streptavidin connection is used to control the assembly of AuNPs into aggregates and to place fluorescent dyes close to the AuNP surface.

Biotin-functionalized nanoparticles of $\sim$60 nm size are purchased from Nanopartz, USA. These nanoparticles have 70 biotin molecules per particle bound to the surface via the covalent polymer bridge, called streptavidin binding sites. These nanoparticles are dispersed in the PBS buffer and are stable at pH values between 4 and 9.

Biotin-functionalized nanoparticles of $\sim$40 nm size are purchased from Roche Diagnostics GmbH, Germany. Biotin is attached to the gold surface via the protein bovine serum albumin (BSA). There is an unsaturated thiol bond in one of the cysteine residues of the BSA molecule so it readily attaches to gold by

a mechanism similar to the binding of thiol-modified ssDNA to gold. Biotin is connected to the lysine residue of BSA via a valeric acid group. The entire surface of the nanoparticles is passivated by BSA molecules, some of which are biotinylated so that each particle has at least 50 binding sites. The approach to assemble biotinylated AuNPs into aggregates with a controlled number of particles connected via a streptavidin linker in bulk is discussed in the next section. A schematic of a ∼40 nm AuNP with BSA and biotin on the surface is shown in Figure 3.2a. In panel b a TEM image is shown and panel c illustrates the statistics of size distribution: the mean nanoparticle size is 36.2 nm with a standard deviation of 4.9 nm.

Apart from connecting AuNPs, the biotin-streptavidin link is used in this thesis to place fluorescent dyes close to a AuNP's surface. These dyes are used to study the Förster resonance energy transfer (FRET) in the presence of AuNPs. Two fluorescent dyes taking part in FRET are called a FRET pair. One dye plays the role of a donor and the other is performing as an acceptor. In this thesis, the multi-subunit protein R-phycoerythrin and Alexa fluor 647 are used as donor and acceptor, respectively. The FRET pair connected to streptavidin was purchased from Sigma-Aldrich, Germany. A sketch of this system is shown in Figure 3.3a, while in Figure 3.3b the photoluminescence excitation (PLE) and fluorescence (PL) spectra of the dyes are presented. For R-phycoerythrin the maximum of the PLE spectrum is at $\lambda_{ex} = 542$ nm and the maximum of the PL spectrum is at $\lambda_{em} = 575$ nm, while for Alexa fluor 647 $\lambda_{ex} = 647$ nm and $\lambda_{em} = 661$ nm. The spectral overlap between the PL spectra of the donor and PLE spectra of the acceptor, which is a necessary condition for the FRET process, is clearly seen.

The last type of particles discussed in this section are non-spherical spiked gold nanoparticles called nanostars. These particles were synthesised in-house by the method described in [133]. In short, the gold precursor chloroauric acid is reduced by the mild reducing agent ascorbic acid in the presence of the surface stabilizer cetyltrimethylammonium bromide (CTAB) and a small amount of silver ions. Both CTAB and Ag ions play a role in formation of the non-sperical shapes. CTAB molecules preferentially adsorb on particular crystal planes of the freshly formed small particles. In this way the CTAB chains block growth in some directions and promote the formation of sharp tips [134]. The role of the Ag

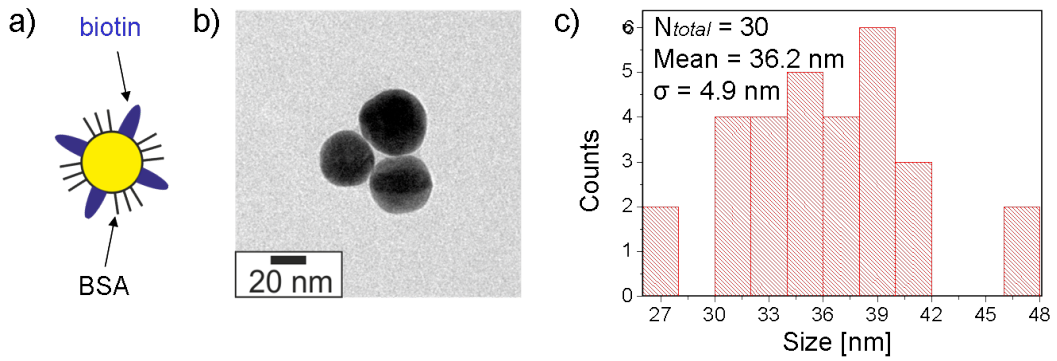

Figure 3.2: Biotinylated AuNPs of ∼40 nm size. (a) Schematic representation of the biotinylated AuNPs. (b) Transmission electron microscope images of the particles. (c) Statistics on the size distribution of the particles.

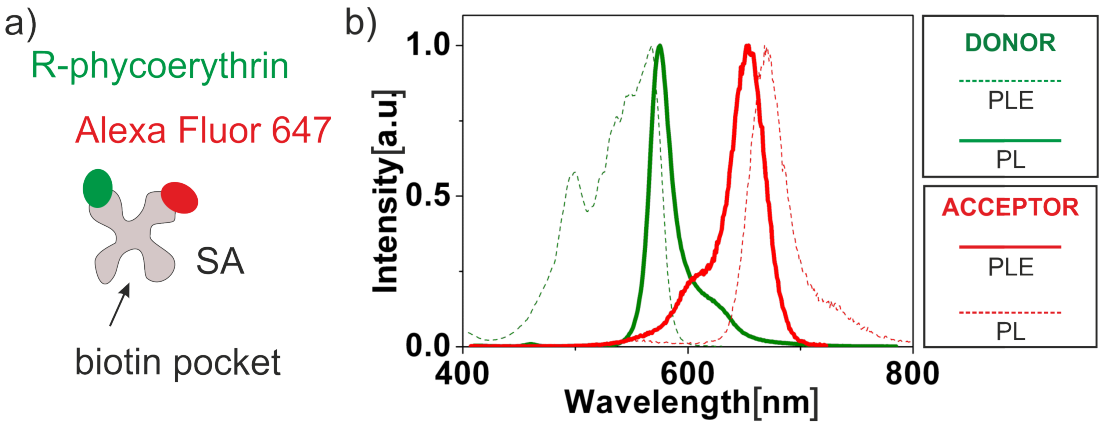

Figure 3.3: (a) Schematic of the streptavidin molecule with a donor and acceptor attached. (b) Photoluminescence excitation (PLE) and fluorescence (PL) spectra of dyes forming the FRET pair: donor R-phycoerythrin and acceptor Alexa Fluor 647 (three molecules).

ions is not clear yet but most probably they are playing a similar blocking role [134, 135]. In Figure 3.4a schematics for a CTAB-stabilized nanostar is shown. Panel b of the same figure shows a TEM image of the nanostars (clustering is due to the sample drying). The average core size of these particles, as revealed from statistics in Figure 3.4c, is 101 nm with a standard deviation of 16.8 nm.

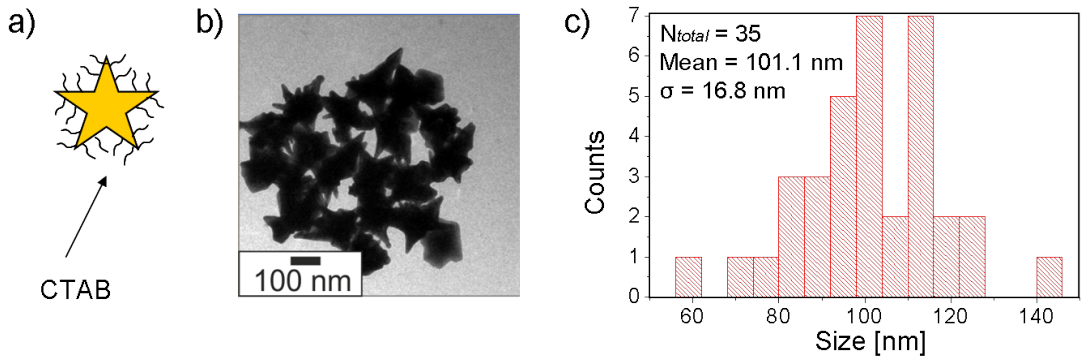

Figure 3.4: Gold nanostars. (a) Schematic representation of the nanostar with the surface stabilizer CTAB. In reality spikes protrude in all directions, also out of the plane of drawing. (b) Transmission electron microscope images of the gold nanostars. (c) Statistics on the core size distribution of the nanostars.

The aim of this thesis is to investigate the influence of AuNPs on the interaction between (bio)molecules situated near their surface. The origin of this influence lies in the plasmonic properties of AuNPs. These properties can be characterized optically. Thus, in the following the optical response of the AuNPs used in this thesis is discussed.

In Figure 3.5 the extinction spectra of hydrosols of spherical biotinylated ∼40 nm AuNPs, of spherical citrate-stabilized 60 nm AuNPs and of Au nanostars with a core size of 101 nm are shown. The measurements of the extinction spectra in bulk were performed on the colloidal gold suspensions dispersed in Mili-Q water. The spectrum of the 40 nm particle shows the plasmon resonance at around 526 nm, while the plasmon resonance of the 60 nm particles is redshifted to around 537 nm. The spectrum of the nanostar shows broad response in the wavelength range above ∼ 650 nm. This response is a sum of several peaks corresponding

to different plasmonic modes of the particle [136]. In case of spectroscopy on a single particle, different peaks of the nanostar can be selected from the general response by installing a polarizer in the detection path [137].

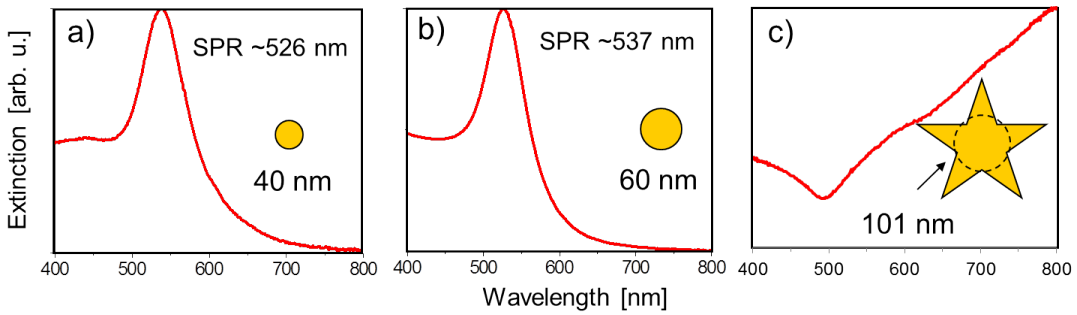

Figure 3.5: Extinction spectra of gold nanoparticles used in this thesis. (a) nanospheres of 40 nm diameter, (b) nanospheres of 60 nm diameter and (c) nanostars with a core size of 101 nm. The response of spherical particles is characterized by a single peak originating from one plasmon mode. The spectrum of nanostars exhibits broad extinction of high intensity due to the overlap of several plasmon modes.

3.2 Protocol for gold nanoparticle dimer formation in bulk

The method for controlled production of AuNP dimers in bulk used in this work was introduced in [110]. The preparation of dimers consists of three steps and is illustrated in Figure 3.6. In the first step streptavidin is added to the hydrosol of biotinylated AuNPs resulting in the formation of streptavidin-linked AuNP aggregates of different sizes. In the second and third step the separation of aggregates according to size and the extraction of aggregates consisting of two particles, i.e. of dimers, is performed. The separation and extraction steps are based on the classical gel electrophoresis technique modified for nanoparticles [138, 139].

The main principle of the gel electrophoresis is the application of a constant electric field to a group of charged species, such as biomolecules or nanoobjects, which are introduced into the porous medium. Charged species move in one direction under the influence of the electric field and the speed of each species depends on its charge and size. If the size and charge distribution in the group of species is discrete, the spatial separation of different species after some time is observed. In this way the mixtures of different small species can be sorted by components.

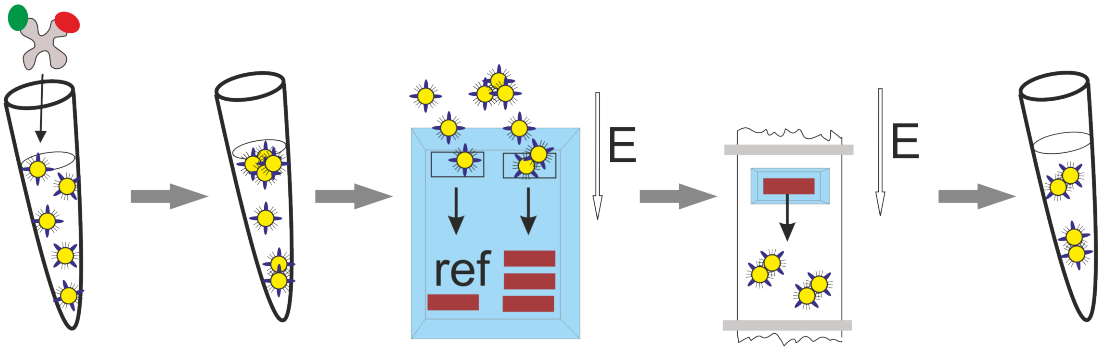

Figure 3.6: Schematic of the preparation of AuNP dimers in bulk. The preparation consists of aggregation, separation and extraction steps.

Aggregation. To induce the aggregation, streptavidin molecules are introduced into the suspension of biotinylated AuNPs. Prior to this the colloid is redispersed in a citrate buffer with a pH of 5.5. At this pH the repulsive force between the nanoparticles is reduced, which enables their aggregation upon addition of the streptavidin linker. The FRET pair consisting of R-Phycoerythrin and Alexa Fluor 647 is already attached to the streptavidin molecule, so it is placed into the central region between the particles in the AuNP dimer upon biotin-streptavidin binding.

In general, if the amount of streptavidin molecules in the solution is too high, a passivation of the AuNP's active sites occurs and the formation of aggregates is suppressed. Also, at too low streptavidin concentrations dimers will be formed only with a very small yield. Therefore the concentrations of streptavidin and biotinylated AuNPs are chosen such that there are two to three streptavidin

molecules available for one biotin molecule. This concentration ratio increases the probability of dimer formation [110].

Separation. After the addition of the streptavidin linker, the solution is incubated for 3 h. Subsequently the sample is centrifuged and the supernatant is removed. The precipitate is then introduced into the gel piece, which is prepared in the following way. Powder of agarose, a polysaccharide derivative of agar, is dissolved in a Tris-Acetate-EDTA (TAE) buffer containing 40 mM tris(hydroxymethyl)aminomethane, 20 mM acetic acid and 1 mM ethylenediaminetetraacetic acid to yield a concentration of 1%. The mixture is brought to boiling, poured into the mold and cooled down. Upon cooling the agarose polymerises and forms a porous structure with pore sizes on the scale of hundreds of nanometeres [140]. The specific shape of the mold serves for the formation of the wells in the gel piece.

After this, the aggregated sample is introduced into one of the wells. Another well is filled with the reference droplet containing only single biotinylated AuNPs with no streptavidin addition. The gel piece is placed into the electrophoresis bath filled with a TAE buffer of pH 8.3 and a DC electric field (140 V, 400 mW) is applied. The different friction experienced by the aggregates of different sizes alters speed of motion in the gel. As time passes, monomers, dimers, trimers and bigger aggregates travel a different distance, resulting in formation of distinct bands in the gel. The furthest band relative to the starting point is the monomer band, closer is the dimer band, and so on. The solution of AuNP monomers with no streptavidin addition is placed into the neighbor well and serves as a reference.

Extraction. To extract AuNP dimers, the dimer band is cut out of the gel and placed in the dialysis tube filled with TAE buffer. Current is applied for a short time and the nanoparticles move out of the gel towards the wall of the dialysis tube. The pores of the dialysis tube are small enough to constrain the movement of the dimers out of the tube (molecular weight cutoff = 5000). As a result, the particles are extracted from the gel into the buffer. The solution is further filtered to get rid of the remaining gel. In this way a hydrosol of AuNP dimers of high yield is obtained. The byproduct of the separation step - the hydrosol of the AuNP monomers decorated with streptavidin bearing the FRET pair - is obtained in the same way.

Due to losses of the nanoparticles in the gel edges, in the walls of the dialysis tube and in the filter, the overall yield of the extraction procedure is around 20% [110]. That is why for the time-resolved measurements presented in Section 5.3, the extraction step was not performed. The dimer band embedded in the gel was cut out and placed into the cuvette for measurements, instead.

3.3 Electron microscopy

AuNPs with sizes of several tens of nanometers cannot be resolved in the optical microscope due to the Abbe diffraction limit [141]. The microscope resolution roughly equals half of the wavelength of the illuminating light, which means that particles of nano sizes are clearly beyond the resolution limit. Electron microscopy, on the other hand, uses electrons for illumination, which allows resolution of several nanometers and below. In this thesis transmission electron microscopy (TEM) and scanning electron microscopy (SEM) are used to gather information about the morphology of samples.

In the TEM the electrons are emanating from the electron gun in the process of thermionic emission. The electron beam is focused by a system of electromagnetic condenser lenses and apertures and directed towards the sample. The beam transmitted through the sample is then focused by the projection system consisting of objective and imaging lenses. Finally, the beam hits the phosphorescent screen, where the magnified image is formed. The magnification of the TEM is determined by the objective lens. Its resolution is defined by the wavelength of the electrons used for illumination, which in turn is controlled by the accelerating voltage. The wavelength of the electrons is calculated as $\lambda = \frac{h}{(2meE)^{1/2}} \approx \frac{1.22}{E^{1/2}}$, where h is Planck's constant, m is electron mass, e is electron charge and E is an accelerating voltage [142]. Therefore with a proper alignment and at an accelerating voltage of 100 kV the resolution is clearly below 1 nm. In this dissertation the samples for the TEM measurements were prepared by drop casting ~ 5 μl of gold hydrosols onto a carbon-covered copper grid. The JEM 1011 transmission electron microscope from Jeol, Germany, was operated at accelerating voltage of 100 kV.

While a TEM is usually used to acquire information about the size and shape of AuNPs, an SEM is more advantageous for studies of the topology of the sample. Here, the image is formed by raster scanning over the sample with an electron beam. The position of the electron beam focused by the condenser lenses is changed by a system of scan coils situated in the objective lens and directed to different points of the sample. Electrons scattered from the sample are collected by a detector. In the SEM several detectors are used. The InLens detector collects electrons inelastically scattered by the sample and is used to obtain information about the surface structures. The SE2 detector gathers both inelastically scattered electrons and elastically scattered electrons and is used to study the topology.

The resolution of the SEM is determined by the beam diameter, the voltage applied to the scanning coils and the working distance, since these effects define the amount of electrons gathered by the detector. The resolution of SEM is on the range of several nm. The magnification of the SEM is defined as the ratio between the area scanned on the sample and the area of the display of the imaging part. In this thesis the SEM measurements were performed with an Ultra Plus 55 field emission SEM (Zeiss, Germany) operated at accelerating voltages of 5-25 kV. Since SEM of non-conducting samples is challenging due to sample charging, samples prepared on glass were covered with a carbon layer prior to characterization.

3.4 Optical trapping dark-field microscopy

Other ways to observe particles having sizes beyond the diffraction limit are fluorescence microscopy and optical microscopy in the dark-field configuration. Dark-field microscopy takes advantage of the high scattering cross sections of metallic nanoparticles at their resonant wavelengths. The sample is illuminated with white light and only the scattered signal is detected, while the directly transmitted light is blocked. As a result, plasmonic nanoparticles or other strongly scattering objects situated on the surface appear as bright spots on the black background. The color of the bright spots corresponds to the resonant wave-

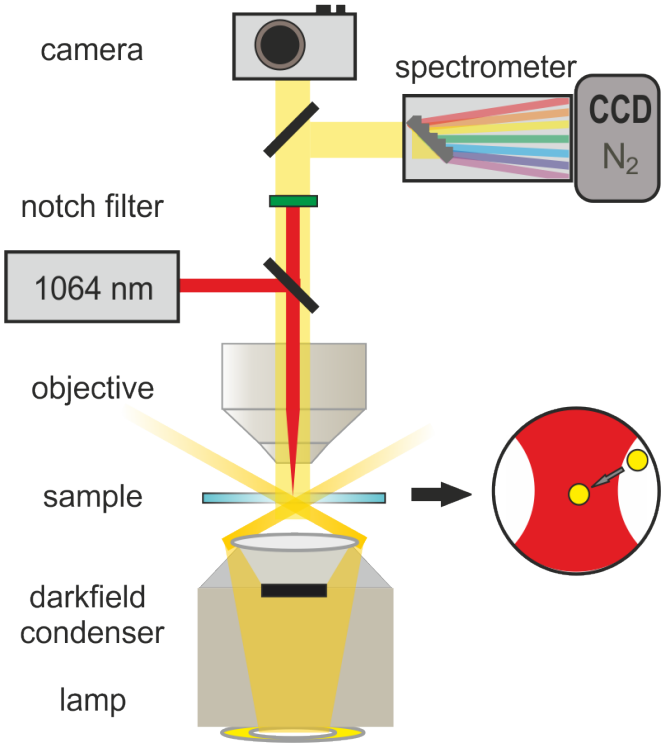

Figure 3.7: Optical trapping dark-field microscopy setup. White light emanating from the illumination source passes through the dark-field condenser. Light scattered by the sample enters the objective, which is simultaneously used to couple in the trapping laser (cw, 1064 nm, 2.1 W). Detection is performed by the consumer digital camera or alternatively by the spectrometer coupled to a CCD. adapted from [153]

length of the scattering spectrum. A change of the plasmonic properties of the imaged object is observed as a change in color of the scattered light. At low particle concentrations, spatially separated plasmonic single particles can be observed in the dark-field microscope.

In this thesis, dark-field microscopy is performed on an AxioScope A.1 upright microscope from Zeiss, Germany. A Halogen Lamp with 100 W continuous output in the visible range of the electromagnetic spectrum was used as an illumination source. Dark-field configuration of the microscope is achieved by inserting a dark-field condenser between the illumination source and the sample. An opaque disk situated in the dark-field condenser blocks the central part of the light beam

creating a hollow cone of illumination. A condenser lens focuses the light, which then impinges on a sample at very large angles. If the numerical aperture (NA) of the condenser lens is larger than that of the objective lens, the light, which was directly transmitted through the sample, is not collected by the objective. At the same time some of the light scattered by the sample (which has therefore changed its direction) enters the objective. The NA of the dark-field condenser used in this thesis is 1.45 while NAs of the objectives used for imaging range from 0.2 to 1.2 for magnifications from 10 to 100 times, respectively.

In Section 3.2 the approach to create AuNP aggregates with a controlled number of particles in bulk is described. By combining dark-field microscopy and the powerful technique of optical trapping (see Section 2.2 for details) one can manipulate single AuNPs, bring them close to each other and monitor this interaction process in the microscope. In this thesis optical trapping of AuNPs in aqueous solution was performed with a Rumba diode-pumped solid state laser from Cobolt AB, Sweden, operating at 1064 nm in continuous wave mode. The laser was coupled into the microscope through a Achroplan 100x water-immersion objective (Zeiss, Germany) and focused on the sample. In a minority of experiments a Tsunami (Newport, USA) Ti:sapphire laser operating at 808 nm is also used as a trapping laser.

The choice of the laser wavelength for optical trapping of nanoparticles has to be performed with a great care, especially for those having large extinction cross sections. As discussed in section 2.2, three-dimensional optical manipulation can be achieved only if the gradient force acting on the trapped object dominates over the scattering force. For the typical experiments with AuNPs of 60 nm size, a laser operating at λ=1064 nm allows stable trapping.

The maximum output of the trapping laser in the system used in this thesis is 2.1 W. The output power of the laser is controlled with the software provided by Cobolt AB, Sweden, and AuNPs are trapped at 100-200 mW measured under the microscope objective. The quality of the beam is of high importance for optical trapping and the nearly Gaussian beam profile of the Rumba is beneficial for optical trapping experiments. Also the trap stiffness and trapping efficiency directly depend on the focusing of the laser beam. Strongest focusing can be achieved if the laser beam slightly overfills the back aperture of the objective.

That is why the initial beam diameter of 2 mm is enlarged 8-fold by installing a telescope NT64-415 from Edmund Optics, USA, in the optical path. The Achroplan 100x objective is not corrected for infrared illumination, therefore the focal plane of the trapping laser does not coincide with the focal plane of detection. To correct this, an additional lens with focal length of 1 m (Thorlabs, Germany) is installed in the laser path just in front of the microscope opening. In the detection path a notch filter NF03-532/1064E-25 from Semrock, USA, is installed to block the IR radiation.

There are two detection outputs at the setup. One is connected to a Canon EOS 550D digital camera, which acquires videos with a frame rate of 50 frames per second, and another is connected to the spectrometer.

Among the different techniques employed for imaging of optically trapped objects, dark-field microscopy is unique because it provides the opportunity to detect both the trapped object and the area around it [143, 144]. This enables monitoring of the arrival and departure of single particles into and out of the trap, which is of paramount importance for the experiments performed in this thesis.

3.5 Steady-state and time-resolved spectroscopy

Steady-state single-particle spectroscopy. Depending on the size, shape and number of AuNPs, their color in the dark-field image can vary from faint-green to deep-red. The plasmon resonance of an AuNP can be therefore approximately estimated by its appearance in the dark-field image. To characterize the wavelength of the plasmon resonance precisely, the Rayleigh scattering spectra of nanoparticles are taken with the ARC SpectraPro SP2556 spectrometer (Princeton Instruments, USA) and a liquid nitrogen-cooled CCD Camera PI Spec-10 LN400BR (Roper Scientific, Germany) coupled to it. The spectrometer and the camera are operated by the software WinSpec32 provided by the same company. A polarization filter (Thorlabs, Germany) is installed in front of the spectrometer to perform polarization-dependent Rayleigh scattering measurements.

As mentioned previously, by controlling the concentration of the AuNPs in the sample it can be achieved that the plasmonic particles appear as well separated spots in the dark-field image. In this case it is possible to acquire a spectrum of a single particle or of a single aggregate. This is done in the following way: first the spectrometer is moved to the zero position so that the collected light proceeds to the CCD chip spectrally unresolved. In this mode an image of the sample is taken and each particle is located. Then, the specific region containing only the particle of interest is selected and the spectrally resolved signal of this region is acquired. This scattering spectrum is then corrected by subtracting the background signal taken from an empty spot of the same size. Finally, the result is divided by the spectrum of the illumination source. In this way one obtains the scattering spectrum of a single particle.

Steady-state ensemble spectroscopy. Plasmon oscillations in metal nanoparticles result in enhanced extinction cross sections at their resonant wavelengths. Since the resonant wavelength of each sample depends on its size, material and shape, one can obtain rich information about the hydrosol by defining the position, shape and width of the plasmonic peak(s) in the extinction spectra.

In this thesis the extinction spectra of gold colloids in bulk were measured with the Varian Cary 5000 spectrophotometer from Agilent Technologies, USA. In this device a Xenon flash lamp is used as a white light source. Light is sent through the double out-of-plane Littrow monochromator where it is dispersed in the spectral range between 200 and 1100 nm. The dispersed light impinges on the cuvette filled with the colloidal suspension and the intensity transmitted through the cuvette is measured by the photodetector. The signal is then corrected by the software for 100% and 0% transmission and plotted as transmittance or absorbance (optical density) versus wavelength. The transmittance is defined as a linear ratio between the intensity of light transmitted through the sample and the intensity of light on the sample at each wavelength in percentage $T\ (100\%) = \frac{I(\lambda)}{I_0(\lambda)}$. The absorbance is defined as a common logarithm of transmittance $A = -log_{10}T$. It should be pointed out that the absorbance is not the measure of absorption but of extinction since reflection and scattering by the sample contribute to the losses of intensity as well.

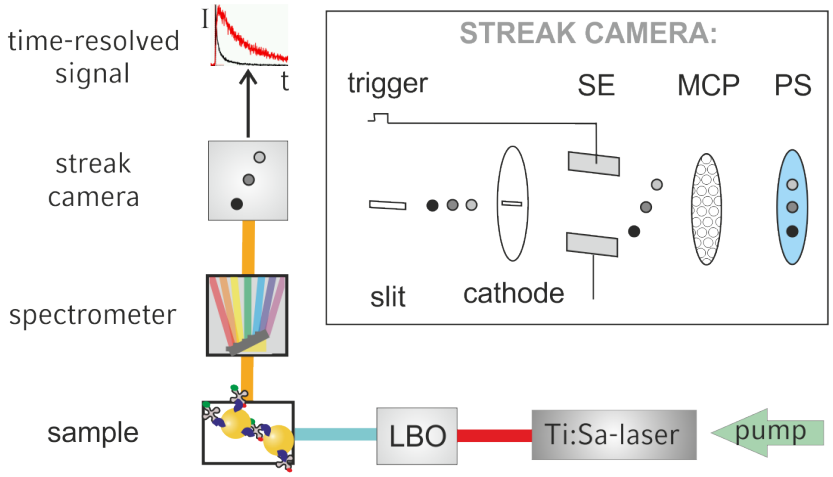

Figure 3.8: Time-resolved fluorescence setup. A Ti:sapphire laser is used as an excitation source. The detected signal is resolved spectrally with a spectrometer and temporally with a streak camera. Inset: the operational principle of the streak camera. Adapted from [145].

Steady state photoluminescence excitation (PLE) and fluorescence (PL) spectra were measured with the Cary Eclipse fluorescence spectrophotometer from Agilent Technologies, USA. In this device the excitation light from the Xenon flash lamp is captured by a Schwarzschild mirror system and directed through the excitation monochromator to the sample. The fluorescence signal from the sample passes through the emission monochromator and photomultiplier and is collected in 90 ^{o} geometry. Amplification of the signal can be tuned by changing the detector voltage. The wavelength range for both excitation and emission spectrometers is 200 - 900 nm. The resolution of the spectrometer is related to the scanning speed; the minimum value for resolution is 1.5 nm. The reference signal is collected in parallel and sent through the reference photomultiplier tube.

Time-resolved ensemble spectroscopy. To quantify the energy transfer process between molecules in the presence of AuNPs, which is discussed in Chapter 5, the fluorescent response of the molecules is resolved in time. This is done on a home-built setup capable of picosecond time resolution. This setup is illustrated in Figure 3.8.

Here a Mira 900-F pulsed titanium sapphire (Ti:sapphire) laser from Coherent, USA, operating in the femtosecond mode serves as an excitation source. The Mira 900-F is pumped by a continuous wave (cw) diode-pumped solid state laser Verdi (Coherent, USA) with an output power of 10 W at a wavelength of 532 nm. The pulsed operation of the Mira 900-F is achieved by mode self-locking due to the nonlinear optical Kerr effect [146]. Since the refractive index of nonlinear media is intensity-dependent, the amplifying medium acts as a convergent lens for high-intensity Gaussian beams. The tunable aperture on the output selects the strongly focused central part of the beam. The nonlinearity in the refractive index results in broadening of the spectrum of the light and in simultaneous reduction of the duration. In this way the short-pulsed response is preferred over the continuous wave operation. The repetition frequency of the Mira 900-F is 76 MHz, which corresponds to 13 ns between pulses. The operational wavelength can be tuned in the range between 750 and 1000 nm. To induce operation below 500 nm the output beam is let through a nonlinear crystal where the second harmonic is generated, so as a result the operational wavelength is half of the initial one.

The laser beam is further directed to the sample by a system of lenses and mirrors. The light transmitted by the sample is blocked and the fluorescence signal is collected at 90^o geometry. The signal first passes through the imaging spectrograph (250is, Cromex, USA) where it is resolved spectrally, and afterwards it enters the streak camera (C5680 Series, Hamamatsu, Japan) where it is resolved temporally.

The working principle of the streak camera is illustrated in the inset of Figure 3.8. Spectrally resolved light passes through the slit and is focused on the photocathode where the photons are converted to electrons. As the electrons proceed towards the anode, they pass through the sweep electrodes situated in it. The electrons, which reach the sweep electrodes at different times are deflected at different angles. After that the electrons travel through the micro-channel plate where the signal is multiplied and reach the phosphor screen where they are converted back to photons. Since the electrons were deflected by the sweep electrodes they hit the phosphor screen at different locations. In this way the temporal evolution of the signal can be visualized.

Finally the spectrally and temporally resolved signal is imaged on the chip of the CCD camera and the image is transferred to the computer. The remote control of the camera as well as data acquisition and analysis are performed by an HPD Temporal Analyzer digital image processing system (Hamamatsu, Japan).

4 Tuning DNA binding kinetics in an optical trap by plasmonic heating

In this chapter the hybridization of DNA strands attached to gold nanoparticles (AuNPs) is investigated. Single AuNPs with DNA on their surface are manipulated in three dimensions (3D) by a tightly focused laser beam performing as an optical trap (OT). When two nanoparticles are in the vicinity of each other they bind due to the hybridization of complementary DNA strands. The binding event is detected optically by the change in the plasmon resonance frequency upon plasmonic coupling of AuNPs.

We find that this specific binding can be tuned by the plasmonic heating. At larger trapping powers the hybridization rates decrease by more than an order of magnitude. This result is explained by higher temperatures preventing the formation of dimers with lower binding energies.

Since factors other than chemical affinity can result in the binding of two nanoparticles in the OT, we further discuss the results of several control experiments, which prove the specificity of binding.

In the outlook we introduce the attempts to extend the idea of binding in the OT to other systems including protein-functionalized AuNPs and AuNPs of non-spherical shapes – nanostars.

4.1 Specific binding of DNA-functionalized gold nanoparticles

Consider two AuNPs of 60 nm size, which are optically trapped by the tightly focused laser beam operating at λ =1064 nm. The region of the OT can be approximated as a sphere with a radius corresponding to the waist radius of the trapping beam. According to [147] the waist radius of the Gaussian beam is calculated as $r = \frac{\lambda}{\pi NA}$, where NA is the numerical aperture of the objective. For the trapping laser and NA used here, the waist radius is $\approx$ 340 nm and the waist diameter is $\approx$ 680 nm. Therefore the OT region is several times larger than the size of the confined particles which allows the free diffusion of particles in the trap. In the dark-field configuration of the optical microscope, where the sample is illuminated by white light and the scattered light is detected, two diffusing AuNPs confined in OT appear as a single green spot due to the resolution limit of the setup. The reason for the green color is the enhanced scattering on the plasmon resonance wavelength of $\sim$ 545 nm.

If AuNPs approach each other and the separation distance becomes smaller than the particle's radius, their plasmon oscillations couple. This gives rise to the excitation of the longitudinal plasmon mode along the axis of coupling resulting in a redshift of the scattering peak. This principle provides the basis of the approach used in this thesis to detect the specific binding of DNA-functionalized AuNPs in the OT. The scheme of our experimental strategy is shown in Figure 4.1a.

The properties of DNA-functionaized AuNPs are described in detail in Section 3.1. Briefly, two types of AuNPs are considered: A-type particles densely covered with single stranded DNA molecules (ssDNA) of 25 adenine units each and T-type particles densely covered with ssDNA of 24 thymine units each. Due to completely complementary strands, A-type and T-type particles have a high chemical affinity to each other. Since particles are functionalized by poly-A and poly-T chains, connection in different configurations can occur. In the case of full hybridization and formation of 24 base pairs, the interparticle distance, considering the interbase distance of 0.34 nm, is 8.5 nm. For the formation of only

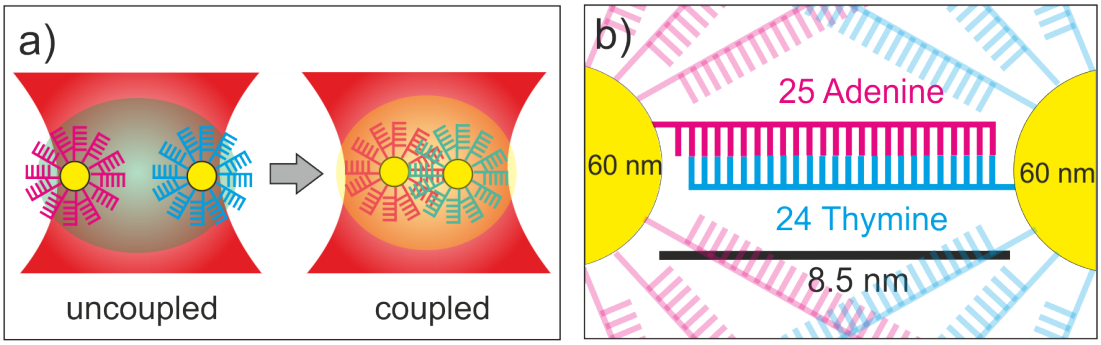

Figure 4.1: (a) Schematic of the specific binding in the OT. Hybridization is detected optically via the scattering signal change due to the plasmonic coupling. (b) Cartoon presenting the interparticle region of two AuNPs bound via hybridization between poly-A and poly-T chains. Full hybridization shown here is only one of many possible configurations. In case of full hybridization the interparticle distance is 8.5 nm. Adapted from [153]

one basepair, the interparticle distance is 16.3 nm. The scheme of full hybridization is shown in Figure 4.1b. To induce the specific binding, A-type and T-type nanoparticles are injected into the droplet of phosphate buffer saline (PBS) on the cover slip under the dark-field microscope. The concentration ratio between A-type and T-type particles is 1:1. Subsequently, NaCl solution is injected so that the final concentration of NaCl in the sample droplet is 200 mM.

The trapping laser is activated and focused well above the surface of the cover slip. One of the particles diffusing near the laser beam is attracted to the focus and becomes optically trapped. Very stable optical trapping is observed and AuNPs escape only if the trap is released by blocking the laser; otherwise the nanoparticles reside in the OT region for tens of minutes. Moreover, by moving the focus of the trapping laser, AuNPs can be moved along x, y and z-axis. This proves that at our experimental conditions the trapped object is confined in all three dimensions.

We set the total concentration of particles in solution very low, ~fM. With this concentration one can monitor arrival of individual particles to the OT and exclude the possibility of uncontrolled multiple trapping.

With the settings described above the subsequent trapping of two single particles is performed and the interaction between them is monitored. Out of 242 experiments where two DNA-functionalized AuNPs are trapped one after another, we observe redshift of the scattering peak in 114 cases. This is consistent with the statistical expectations. Since AuNPs of two types are present in solution in equal quantities, the probability to observe hybridization should be 50%. In the other cases two non-complementary nanoparticles are present in the OT. Events in which no coupling is observed after 3 minutes are considered as no-coupling events and are not included into the analysis.

A typical result of the binding experiment is demonstrated in Figure 4.2. Two micrographs show a pair of complementary AuNPs in uncoupled and coupled states (Figure 4.2a). Redshift of the scattering response can be seen by the naked eye. Figure 4.2b shows the normalized measured scattering spectra of AuNPs in the uncoupled and coupled state. Two single AuNPs in the OT scatter at $\sim$ 555 nm (green line). It is similar to the spectral response of the single particle, only the magnitude of the intensity is different, because two particles scatter twice as much light. The scattering peak of single DNA-functionalized AuNP or of two uncoupled DNA-functionalized AuNPs is slightly redshifted with respect to the plasmon resonance of the unfunctionalized citrate-stabilized AuNPs. This can be explained by the increased refractive index of the surroundings of the particle due to the dense DNA coverage of the surface.

In the coupled state, the redshift of the scattering peak to $\sim$ 575 nm is observed (orange line). This corresponds to the calculated value of the longitudinal plasmon peak of the dimer consisting of 60 nm AuNPs separated by 10 nm, as shown in the normalized calculated scattering spectra in Figure 4.2c. A deviation from the calculated interparticle distance is possible since in this calculation the increased refractive index around the particles is not taken into account. Nevertheless this value is in the expected range between 8.5 and 16.3 nm.

It should be pointed out that the shorter separation distances between nanoparticles result in larger redshifts. Two mechanically touching spheres would scatter not in yellow but in red [148]. This behavior is not observed in our experiments. This again proves that the dimer is formed due to specific interactions

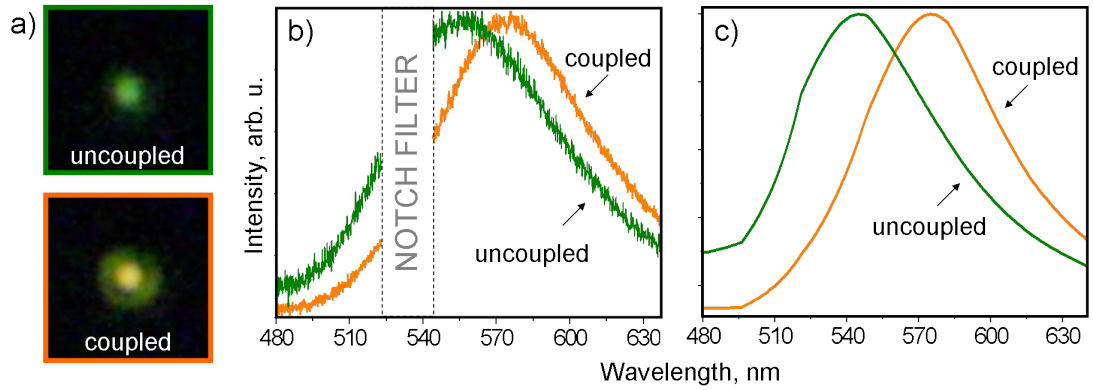

Figure 4.2: (a) Micrographs of a pair of A-type and T-type AuNPs in the OT. Two single nanoparticles scatter in green while chemically bound and plasmonically coupled AuNPs scatter in orange. (b) Measured scattering spectra of uncoupled and coupled AuNPs in the OT. Spectra are normalized to unity. (c) Calculated transversal and longitudinal scattering response of two 60 nm nanoparticles separated by 10 nm. Spectra are normalized to unity.

between complementary DNA strands which are preventing two AuNPs from direct interaction.

At this point it is important to discuss the alignment of the AuNP dimer in the OT. If the dimer was situated parallel to the optical axis, one would not be able to register the longitudinal mode of the plasmon resonance but only the transversal one. However, it was shown, in contrast to elongated micro-sized objects, which align in the OT parallel to the laser beam axis [149, 150], that elongated nanoobjects like gold nanorods or AuNP dimers align perpendicular to the laser axis and parallel to the polarization of the beam [151, 152]. Therefore in our configuration the longitudinal plasmon resonance of the AuNP dimer can be registered. To selectively collect the longitudinal plasmon resonance, a polarization filter is installed in the detection path.

To conclude, through the appropriate choice of the surface decoration the formation of a single dimer in an OT is achieved. The formation of dimer due to specific interaction of complementary DNA strands is statistically confirmed. The unique experimental conditions allow the detection of the plasmonic response of

the particles in unbound and bound states. The interparticle distance in a dimer deduced from the calculated plasmonic response is $\sim$ 10 nm which is consistent with the distance in a DNA-bound AuNP dimer. These precise experimental conditions facilitate a further step in the controlled manipulation of hybridization of DNA near AuNPs as described in the following section.

4.2 Tuning DNA binding kinetics by plasmonic heating

4.2.1 Reduction of coupling rates with increasing laser power

In the experiments described above the plasmonic properties of AuNPs are used to detect the binding event. In this section the plasmonic properties of AuNPs are utilized to actively influence the hybridization of DNA strands attached to them. In particular it is shown that the kinetics of DNA binding can be manipulated by changing the power of the trapping laser which defines the temperature of AuNPs.

The experimental approach employed here is based on the experimental conditions described in the previous section. Complementary A-type and T-type nanoparticles are optically trapped and bind via hydrogen bonding thus forming a dimer. The process is monitored in the dark-field microscope. The strategy is to change the power of the trapping laser and to study the influence of this change on the kinetics of particle coupling. To this end, the videos of the coupling events are recorded at different trapping powers and the kinetics of the coupling is analyzed. A typical timeline of one experiment is demonstrated in Figure 4.3. The lower panel shows the micrographs taken at different times of the experiment and the upper panel presents the corresponding cartoons. In this specific example the power of the laser is set to 141 mW. At the beginning of the observation the first particle is optically trapped and time is set as zero, t = 0 s. At t = 1 s the second particle appears in the focal plane and diffuses around the region of the OT. At a certain moment, in this case at t = 1.16 s, the second particle diffuses into the

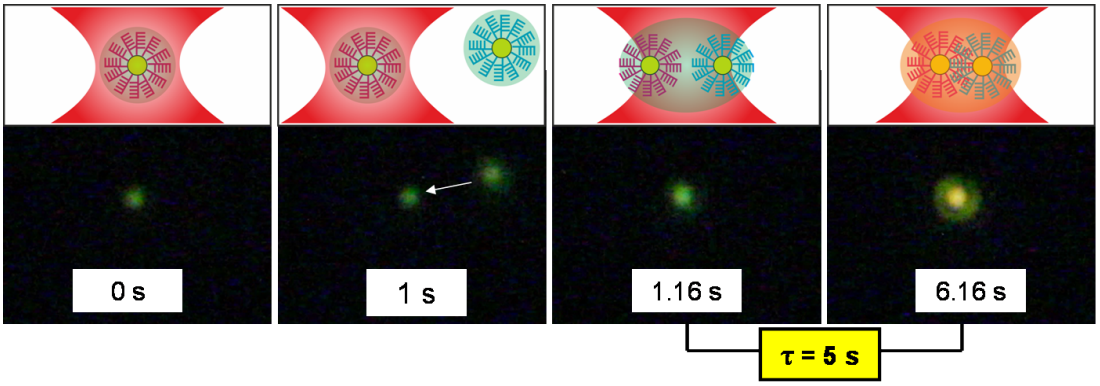

Figure 4.3: Snapshots from a typical experimental video and corresponding sketches. At t=0 s a single DNA-functionalized AuNP in the OT scatters green light. At t = 1 s a second DNA-functionalized AuNP appears nearby the trap and enters the trap at t = 1.16 s leading to an increased scattering intensity. At t = 6.16 s DNA hybridization occurs leading to plasmonic coupling observed as a color change of the scattered light. The binding time τ (i.e. difference between time of color change and time of entry of the second particle) is 5 s in this case. Reprinted with permission from [153]. Copyright 2013 American Chemical Society

region of the OT. As soon as both nanoparticles are in the OT they cannot be optically resolved and thus appear as one object. The presence of the second particle, though, can be detected by the increase of the scattering intensity. No plasmonic coupling is observed yet since the wavelength of the scattered light did not change. After five seconds (t = 6.16 s) the redshift of the scattering peak indicating the plasmonic coupling is observed. The coupling time τ is defined as a difference between the moment of arrival of the second particle to the trap and the moment of the plasmonic coupling.

Figure 4.4a shows the coupling times τ measured at three trapping powers on a logarithmic time scale. A total of 69 coupling events were recorded for the trapping power of 120 mW on the sample, 25 coupling events were recorded for 141 mW and 24 events were recorded for the highest power used in the experiment of 170 mW. Events in which no coupling was observed after 3 min are considered as no-coupling events and are not included in the data set. The medians of the

coupling times are 0.93, 6.95, and 26.20 s for the three trapping powers of 120, 141 and 170 mW, respectively. Clearly, the coupling time increases with the trapping power by more than an order of magnitude.

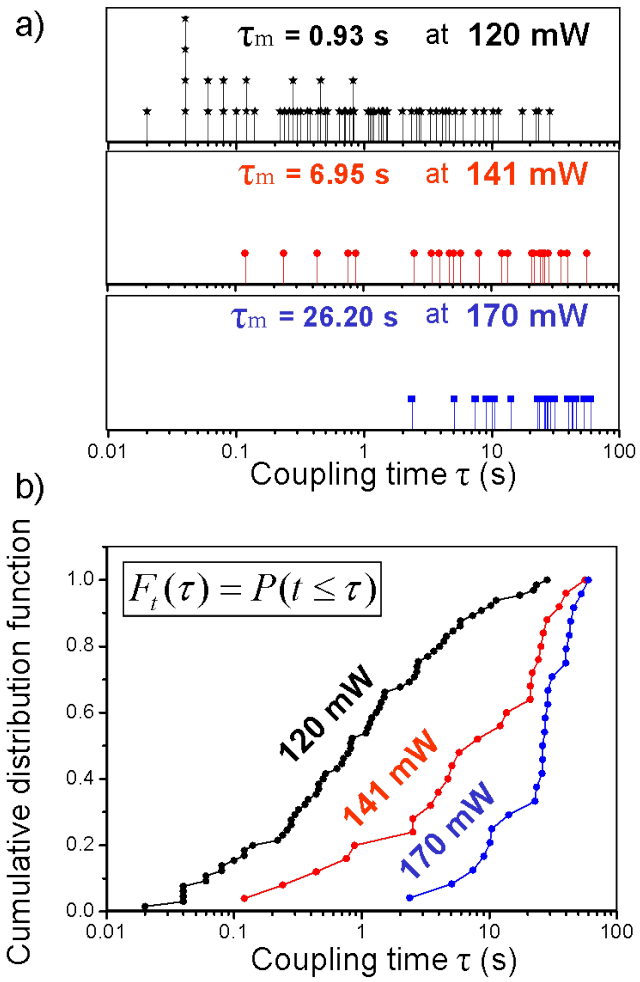

Figure 4.4: (a) Vertical drop line plots of measured coupling times τ at three different trapping powers. Each symbol corresponds to one coupling/hybridization event. A total of 69, 25 and 24 events are observed for trapping powers of 120, 141 and 170 mW, respectively. The coupling times increase with increasing trapping power. (b) Data of panel A plotted as a cumulative distribution function Fτ(t), which expresses the probability to find a coupling event at time $\tau \leq t$.Reprinted with permission from [153]. Copyright 2013 American Chemical Society

If the total number of coupling events at each trapping power is normalized to one and coupling times are put in ascending order while keeping the x-axis the same, these data can be plotted as a cumulative distribution function F_τ(t) versus coupling time τ, Figure 4.4b. A cumulative distribution function is defined by the following expression:

$$F_t(\tau) = P(t \leq \tau). \tag{4.1}$$

where P stands for probability. For a given coupling time τ the value of the cumulative distribution function reflects the percentage of dimers that couple by that time in a set of experiments. The median coupling times for each trapping power therefore correspond to the value of cumulative distribution of 1/2. Each dot in the drop line plot for each power corresponds to one dot on the cumulative distribution curve for each power. A smaller slope of the function corresponds to a broader distribution of coupling times and vice versa. The representation via cumulative distribution function clearly illustrates the deceleration of the binding kinetics at larger powers.

As shown in this subsection, the specific binding process between DNA- functionalized AuNPs and therefore the hybridization of DNA near AuNPs can be manipulated by choice of the trapping conditions. Namely, the decrease in binding rates with the increase of the trapping power is observed. The factors influencing the binding kinetics of the DNA-functionalized AuNPs in the OT, as well as the qualitative model explaining the observed behavior, are introduced in the following subsections.

4.2.2 Effects originating from the increase of the trapping power

The power increase of the trapping laser has two main consequences, which influence the binding kinetics of DNA-functionalized AuNPs: increase of the trap stiffness and increase of the local temperature due to the plasmonic heating by nanoparticles. In the following we first discuss the effect of the trap stiffnes and

then turn to the discussion of the influence of plasmonic heating on the DNA hybridization.

If the trap potential *U(x)* is assumed to be harmonic, the trap stiffness κ is related to the trapping potential via $U(x) = \frac{1}{2}\kappa \cdot x^2$ where x is the displacement of the trapped object from its equilibrium position. With the experimental settings employed here, the non-resonant trapping conditions can be assumed and the OT is dominated by the gradient force. In this case, the stiffness is proportional to the trapping power [143]. With the growing trap stiffness, AuNPs become more confined in the optical trap region and collide more often. More frequent collision would lead to a higher probability for DNA hybridization and therefore result into increase in the binding rates. However, this result is in contradiction to the observed deceleration of coupling rates with increase in power. Therefore the increased trap stiffness is not governing the DNA-functionalized AuNPs binding kinetics at the increased trapping laser power.

Further we discuss the increase in the local temperature around the particles due to plasmonic heating and quantify the temperature increase at each trapping power. Determination of temperature on the nanoscale is a non-trivial task both from the experimental and theoretical point of view [13, 154–156]. Authors in [12] show that the temperature of AuNPs scales with volume. The authors use the heat transfer equation – the expression for the temperature distribution around optically stimulated nanoparticles:

$$\rho(\mathbf{r})c(r)\frac{\partial T(\mathbf{r},t)}{\partial t} = \nabla k(\mathbf{r})\nabla T(\mathbf{r},t) - Q(\mathbf{r},t) \tag{4.2}$$

Here $\mathbf{r}$ and t are spatial coordinate and time, respectively; T is the local temperature; Q represents the heat source; and ρ, c and k are the mass density, specific heat and thermal conductivity, respectively.

In this thesis, the temperature near AuNPS due to plasmonic heating is estimated numerically using a combination of Comsol Multiphysics amd MQMieAggregates commercial programs. In these programs, the optically trapped dimer consisting of two AuNPs of 60 nm is assumed to act as a heat source. The optical power absorbed by a dimer is calculated as $Q = P \cdot C_{abs}/V$ where P is the laser power density, V is the volume of the dimer, and C_{abs} is its absorption cross sec-

tion. C_{abs} of the dimer at the trapping wavelength (1064 nm) is calculated with the MQMieAggregates software. We assume the interparticle distance as 8.5 nm, which corresponds to the length of 25 adenine bases and is the minimum distance possible. We designate that this minimum distance corresponds to the maximum calculated temperature possible in the experiment and the actual temperature is lower. For larger interparticle distances, C_{abs} of the dimer at 1064 nm decreases resulting in lower temperatures. In the calculations the dimer was embedded in a sphere of water with a radius of 5000 nm and a refractive index of 1.33. Effects of the DNA functionalization are neglected in the calculations. Furthermore, the heat distribution around AuNPs is found by solving the heat transfer equation employing the finite element calculations with Comsol Multiphysics software.

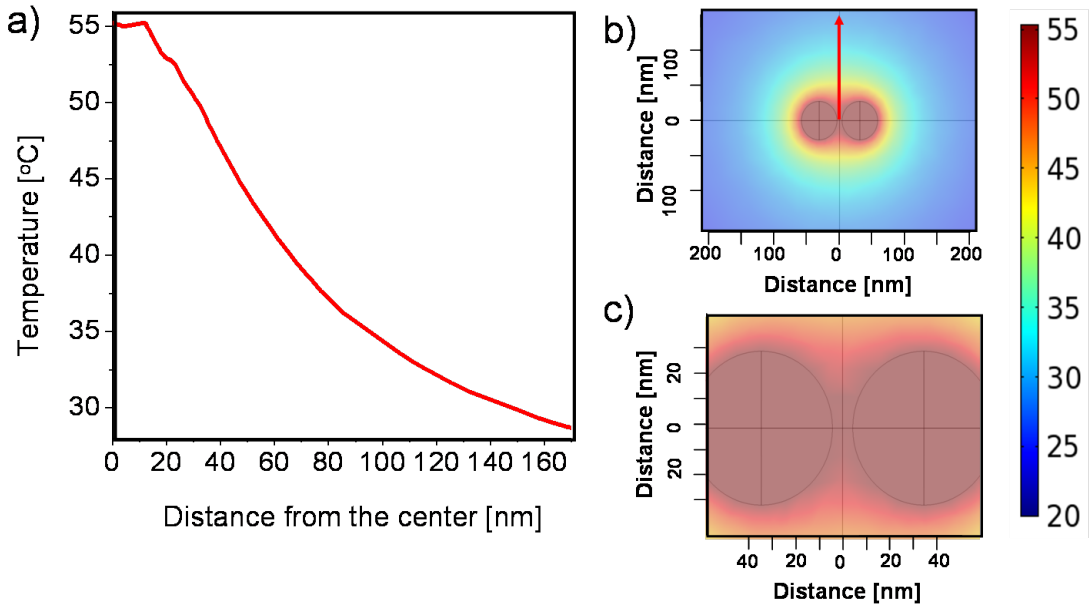

Figure 4.5: Simulated temperature profile of two AuNPs of 60 nm separated by 8.5 nm when excited with linearly polarized 1064 nm laser of 170 mW power. (a) Temperature dependance from the distance from the central region between two nanoparticles. (b) Temperature spatial distribution. (c) Zoom into the central region of (b).

As a result, the maximum temperatures in the center of the dimer, consisting of two AuNPs under excitation with 1064 nm light polarized along the dimer's axis,

are 45, 49 and 55 ^{o}C for the trapping powers 120, 141 and 170 mW, respectively. In literature there are no reports on the temperature of dimer consisting of AuNPs of 60 nm so far. For single particles, however, our calculation procedure provides values that are in agreement with those reported in [13, 155].

In Figure 4.5 the spatial distribution of the simulated temperature values at a trapping power of 171 mW on the sample is shown. The distance from the center is given in nm and the direction is indicated by the red arrow in panel b. At 60 nm away from the center, the temperature falls to half of the initial value. Panel c shows a zoom into the central region of panel b.

Concerning the temporal gradient, we estimate the relaxation time for 60 nm AuNPs to reach the temperature equilibrium with the environment as ∼580 ps. This conclusion is based on work where it is shown that the maximum relaxation time for 50 nm AuNPs is 400 ps and that the relaxation time in nanoscale systems increases with the square of the particle's radius [157]. One can therefore conclude that the processes described in this section are not influenced by the temporal relaxation since they occur on a different timescale.

The temperature increase has several effects: first, it accelerates the diffusion of the AuNPs in the OT volume; second, it increases interactions between single strands; and third, it brings the system closer to the DNA melting temperature region. The increased diffusion of the AuNPs in the OT volume would lead to the same effect as an increased trap stiffness: the probability of particle collision grows and an increase of coupling rates is expected. It can be concluded that increased particle diffusion, though present, is not dominating the observed coupling behavior at elevated laser powers.

Changes in interaction between strands with growing temperature can be discussed in terms of Arrhenius law $k = Ae^{-E_a/k_BT}$, introduced in the Chapter 2.3. For chemical reactions, which follow the two-states-one-step scheme the reaction rates k increase when increasing temperature. The values of reaction activation energies E_a are positive in this case. In contrast, binding kinetics of DNA strands is sometimes modeled as a two-step three-state process [60]. In that model, at particular values for E_a and frequency factors A for each of the two steps of reaction, the dependence between the temperature and reaction rates is reversed. This means that the temperature increase causes the decrease of binding rates

and increase of the binding times [60]. However, for our system and with the simulated temperature values discussed above, we could not find any set of E_A and A parameters satisfying the two-step-three-state model, which would have a physical meaning. This model is therefore not applicable in our case. Obviously, the fact that the system is brought close to the melting temperature region should be considered in the explanation of the observed result.

The calculated temperature maxima in a localized area between the particles are lower than the bulk aggregate hybridization temperature of $\sim 56\ ^{o}$C, which is necessary to observe binding. Indeed, binding (although with different rates) was observed at all trapping powers. Nevertheles we claim that the vicinity to the melting temperature region is governing the binding kinetics of the DNA-functionalized AuNPs. In the next section the semi-quantitative model supporting this idea is introduced.

4.2.3 Semi-quantitative model for the dimer melting temperature

We propose the following semi-quantitative model to explain the observed decrease in the coupling rates with increasing trapping laser powers. The DNA sequences attached to AuNPs are not specific but consist of either purely adenine or purely thymine bases. This does not allow one to define the specific configuration in which the AuNPs can form a dimer, for both the number of hybridized strands N_{HS} taking part in the connection and the number of base pairs hybridized in each pair of strands N_{HB} can vary. For each type of these configuration the binding energy will be different. As a result, at higher trapping powers and thus higher temperatures, dimers with a lower number of connections will not form anymore. Therefore at higher temperatures the probability of successful binding is smaller, which directly means the decrease of binding rates.

In order to develop the model proposed above, we introduce the dimer melting temperature T_{m-dim} expressing the collective melting temperature of the number of hybridized DNA double-strands connecting two AuNPs. The more strands and base pairs are hybridized in a given dimer, i.e., the larger N_{HS} and N_{HB} are, the higher the dimer melting temperature will be. We estimate the dimer melting

temperatures for different configurations and compare them to the previously calculated temperatures in the hot spot of a dimer induced by plasmonic heating.

The melting temperature of the AuNP dimer T_{m-dim} is calculated using the variation of the formula for T_m of the free DNA strands hybridizing in bulk, which is introduced in Section 2.3.

$$T_{m-dim} = \frac{\Delta H_{N_{HB}}}{\Delta S_{N_{HB}} + Rln\left(\frac{C_T}{4}\right)} - 273.15 \tag{4.3}$$

where $\Delta H_{N_{HB}}$ is the enthalpy and $\Delta S_{N_{HB}}$ is the entropy of the hybridization of two single strands with N_{HB} base pairs each, R is the molar gas constant and C_T is the normalized total concentration of strands, calculated as $C_T = N_{HS}/V_{OT}$. Here N_{HS} is the total number of hybridizing strands and V_{OT} is the OT volume.

ΔH_n and ΔS_n are calculated within the nearest neighbor model, where contribution to enthalpy and entropy from neighboring overlapping pairs is summed over the whole length of the double helix. The detailed explanation of this model is given in Section 2.3. According to the nearest neighbor model the expressions for ΔH_n and ΔS_n are as follows:

$$\Delta H_{N_{HB}} = 2 \cdot H[AT_{init}] + (N_{HB} - 1) \cdot H[AA/TT] \tag{4.4}$$

$$\Delta S_{N_{HB}} = 2 \cdot S[AT_{init}] + (N_{HB} - 1) \cdot S[AA/TT] \tag{4.5}$$

where $H[AT_{init}]$ and $S[AT_{init}]$ are the enthalpy and entropy of the initiation of connection, and $H[AA/TT]$ and $S[AA/TT]$ are enthalpy and entropy of connection of subsequent pairs, respectively. These parameters are taken from [67] and corrected for the NaCl concentrations of 200 mM according to:

$$\Delta S_{corrected} = \Delta S_{1MNaCl} + 0.368 \cdot N \cdot ln([Na^+]) \tag{4.6}$$

where N is the number of nucleotide pairs in the strand and $[Na^+]$ is the concentration of Na^+ ions.

The minimum number of connections between two nanoparticles is one, comprising two hybridizing strands, $N_{HS} = 2$. To estimate the maximum possible number of connections between nanoparticles, the following geometrical consid-

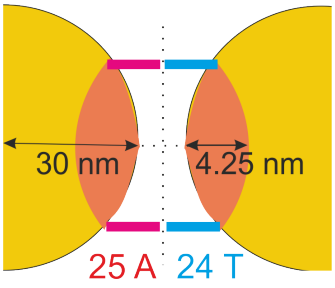

Figure 4.6: Geometrical model to calculate the maximum number of hybridizing strands

eration is applied. A 60 nm AuNP is assumed as a sphere with a total surface area of 11304 nm^2. With a known number of DNA molecules per nanoparticle' surface ($\sim$ 1500) the footprint of one molecule is estimated as 7.5 nm^2. Only the molecules situated in the spherical caps marked in orange in Figure 4.6 are considered to take part in connection. Molecules situated outside of these zones cannot form even a single base pair at any angle. The area of the spherical cap, with the height that equals half of the length of one single strand, $h = 4.25\ nm$, is $\sim 800\ nm^2$. Therefore the maximum number of possible connections between nanoparticles is $\sim$ 100, comprising $\sim$ 200 hybridized strands, so $N_{HS} = 200$. The minimum number of hybridized base pairs is 1 and the maximum number of hybridized base pairs is 24.

The calculated T_{m-dim} curves for different numbers of strands in the dimer N_{HS} as a function of number of hybridized base pairs N_{HB} are shown in Figure 4.7. These values are compared to the estimated dimer temperatures due to the plasmonic heating. Two trends can be clearly recognized. First, the dimer melting temperature increases if more base pairs participate in the hybridization; and second, if more strands hybridize.

It can be concluded from Figure 4.7 that the change of dimer melting temperature with the number of strands and number of bases taking part in binding approximately equals several Kelvin. This, in turn, is approximately equal to the temperature range which corresponds to the laser powers used in the experiments. This can serve as strong support for the semi-quantitative model introduced above. Indeed, as the trapping power grows, the increased temperature prevents the formation of weakly bound dimers with small number of bases or strands participating in the hybridization. The higher the temperature, the more base pairs and strands need to hybridize to form a stable dimer. In other

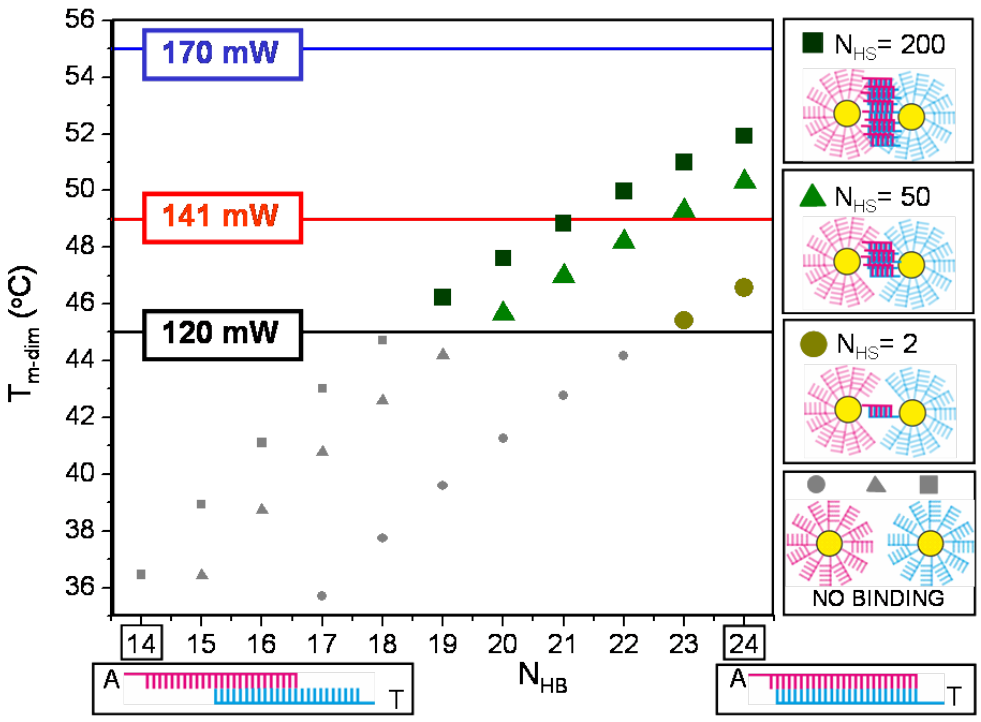

Figure 4.7: Estimated dimer melting temperatures as a function of number of hybridized base pairs N_{HB} for dimers with 2, 50 and 200 strands participating in the hybridization, respectively. Estimates of the temperatures achieved by plasmonic heating are indicated as horizontal lines. Reprinted with permission from [153]. Copyright 2013 American Chemical Society.

words, the probability of forming a stable dimer decreases, binding time increases and a deceleration of the binding kinetics is achieved.

Another observation is related to the fact that the AuNP dimer close to the melting-temperature region behaves as a dynamic system. Therefore, the distance between the nanoparticles fluctuates even after the initial hybridization. This is experimentally observed as a blinking phenomenon in the recorded videos - rapid change of the green (uncoupled) to yellow (coupled) color of the trapped object after initial binding. The timescale of blinking ranges from sub-seconds to several seconds. For detailed analysis it would be beneficial to perform a tracking study and deduce the confinement of particles from the stiffness of the trap. However,

at this late stage of experiment, after several minutes of the observed initial hybridization, the concentration of particles in the near-trap region increases and the trapped pair must be optically moved to prevent diffusing of a third particle into the trap. This movement would influence the tracking study and the analysis of the trap stiffness would not be reliable. When the OT is released by blocking the laser, the nanoparticles escape from the trap region. In some experiments, the escape of a single object scattering in yellow, attributed to the AuNP dimer, is observed. Also in some experiments, two separated nanoparticles each scattering in green leave the region of the trap and diffuse in different random directions. It appears that the state of the released object (coupled dimer or two uncoupled nanoparticles) can be correlated to the power used in the trapping experiment. With 120 mW used on the sample, the release of coupled dimer is observed in 72%. When the trapping power is increased to 141 mW, the release of the coupled dimer is observed in 55% of the cases. With the maximum power of 170 mW, the amount of observed coupled dimers after the trap release decreased to 44%. This observation supports the semi-qualitative model introduced above, in that with the increase of the trapping power the stability of the dimer decreases as a result of the increased temperature in the interparticle region.

4.3 Control experiments to prove the specificity of binding

We claim that the observed plasmonic coupling between the A-type and T-type nanoparticles in the OT is the result of the hybridization between complementary DNA strands decorating their surface. However, effects other than chemical affinity may play a role in plasmonic coupling of AuNPs. To eliminate these effects and prove specificity of A-type and T-type AuNPs binding, several control experiments are performed.

First, the coupling of unfunctionalized citrate-stabilized AuNPs in an OT is studied. Two citrate-stabilized AuNPs of 60 nm size are trapped with a laser operating at 808 nm with a power of $\sim$ 25 mW on the sample. The particles are trapped one after another (see Figure 4.8a) and their interaction in the OT is

monitored. Most of the trapped pairs exhibit no plasmonic coupling, which can be seen from the micrographs of the OT region, taken at the interval of several seconds. This behavior is illustrated in Figure 4.8b. No detectable change of the wavelength of scattering light is observed with time, and hence no plasmonic coupling occurs.

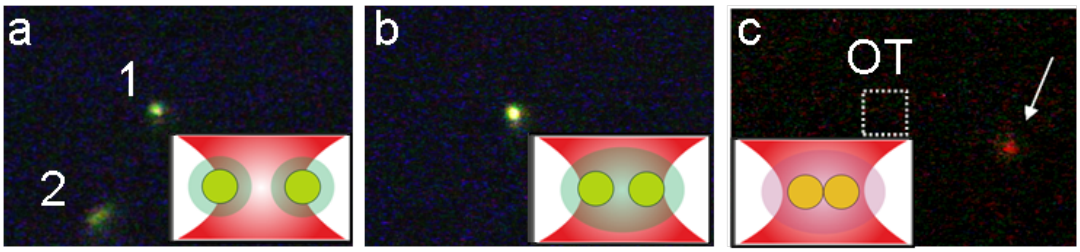

Figure 4.8: Characterization of two citrate-stabilized AuNPs in the OT. (a) Micrograph and schematic of one particle trapped (1) and second particle approaching the region of the OT (2). (b) Micrograph and schematic of two AuNPs showing no coupling in the OT (c) Micrograph of AuNP dimer moving away from the region of the OT due to the optothermal escape and schematic of plasmonic coupling of touching spheres.

Only in less than 20% of the cases is the redshift of the scattering peak observed, indicating plasmonic coupling of AuNPs. Contrary to the A-type and T-type AuNPs, which are densely covered with long DNA chains and can not mechanically touch, citrate-stabilized AuNPs can approach each other to very small distances and can mechanically touch in case of inhomogeneity in the surface coverage. This leads to stronger plasmonic coupling and more pronounced redshift of the scattering peak as compared to DNA-connected AuNP pair. At a certain point, the scattering peak becomes close to the wavelength of the trapping laser (808nm), destabilzing the three-dimensional OT and allowing the escape and diffusion of the dimer away from the region of the trap. This effect, known as optothermal escape, was first described in [144]. In the micrograph in Figure 4.8, the dimer diffused out of the OT region is marked with an arrow. The redshift of the scattering signal of the dimer can be seen with a naked eye.

In [158] the dimerization of citrate-stabilized AuNPs is induced by adding NaCl to the sample droplet. Increased concentration of NaCl should lead to screening

of charges on AuNP's surface leading to the decrease in electrostatic repulsion between the AuNPs. In this thesis, however, the addition of the same amount of NaCl promoted the adhesion of the particles to the cover slip but did not influence their interaction in the OT.

Not only do artificially high salt concentrations lead to unspecific binding of AuNPs, but also excessive laser powers both making the role of chemical affinity of AuNPs in the binding process negligible. The next series of control experiments are dedicated to find the range of salt concentrations and laser powers where the specific binding is observed. For this, two samples are considered. The first one consists of exclusively A-type AuNPs without the addition of complementary T-type AuNPs. The second sample contains both types of AuNPs in the concentration ratio of 1:1. Laser power is tuned in the range between 111 mW and 199 mW. Two NaCl concentrations are used: 200 mM and 500 mM. Other experimental conditions including the total concentration of AuNPs in the sample droplet are kept similar to those in sections 4.1 and 4.2.

The results of these experiments are summarized in the tables below. Crosses stand for "no coupling" and ticks stand for "coupling". At a salt concentration of 200 mM for the system of two A-type particles coupling is observed in less than 15% of all meeting events at any laser power. At the salt concentration of 500 mM, coupling is observed in almost all the cases. This is different for the sample containing A-type and T-type particles in the concentration ratio of 1:1. At salt concentration of 200 mM and at laser powers between 111 and 170 mW on the sample, the plasmonic coupling is observed. At the power of 199 mW on the sample the coupling is not observed. At salt concentration of 500 mM coupling is observed in almost all the cases, similar to the case of A-type particles only. Therefore it can be concluded that at laser powers of 111-170 mW and at salt concentration of 200 mM complementary AuNPs bind while the identical AuNPs do not bind. In other words, at these experimental conditions only specific binding is observed and unspecific binding can be neglected.

Laser power	[NaCl] = 200 mM	[NaCl] = 500 mM
111 mW	✘	✔
120 mW	✘	✔
141 mW	✘	✔
170 mW	✘	✔
199 mW	✘	✔

Table 4.1: Binding at different conditions when only A-type AuNPs are present in solution.

Laser power	[NaCl] = 200 mM	[NaCl] = 500 mM
111 mW	✔	✔
120 mW	✔	✔
141 mW	✔	✔
170 mW	✔	✔
199 mW	✘	✔

Table 4.2: Binding at different conditions when A-type and T-type AuNPs are present in solution in ratio 1:1.

Finally, the control experiment "competitive binding" is performed. Free single strands of T-type are injected into the solution, initially containing A-type and T-type particles. Free strands of T-type can hybridize on the A-type particles, thereby blocking them from interaction with the T-type particles. The concentration of the free T-type strands is set to be 1000-fold the concentration of A-type strands decorating the A-type particles. Prior to the optical experiment, the sample is incubated for 1 hour. The laser power on the sample is kept at 120 mW and the concentration of NaCl is set to 200 mM, thus ensuring the specific binding regime. In these series of experiments the coupling is observed only in less than 15% of the cases. This experiment represents another argument for the specificity of binding between A-type and T-type particles.

To conclude, the results of several series of control experiments prove that at the experimental conditions used in Sections 4.1 and 4.2, plasmonic coupling between AuNPs in the OT should be attributed to chemical affinity of the com-

plementary DNA-functionalized AuNPs while contribution of unspecific binding can be neglected.

4.4 Outlook: protein binding and non-spherical nanoparticles

Compared to the weak DNA-DNA binding, connection between the organic molecule biotin and the protein streptavidin is more stable. By using the biotin-streptavidin link for creating single AuNP dimer in the OT, one would be able to precisely set the interparticle distance at ∼5 nm, defined by the size of the protein. This interparticle distance would lead to the strong plasmonic coupling beneficial for the field-enhanced spectroscopy. Other particles attractive for the field-enhanced spectroscopy are non-spherical spiked AuNPs – nanostars – where the high field enhancement on the ends of the spikes is observed [159]. Dimers of these particles might provide even higher field enhancement due to the coupling of the single tips. Motivated by these findings, as a next step we attempt to extend the approach of creating single DNA-bound AuNP dimer in the OT to the biotin-streptavidin bound AuNP dimer and to the dimer of Au nanostars.

Spherical biotinylated AuNPs in the OT. The optical properties and other characteristics of single biotinylated spherical AuNPs of 60 nm are described in detail in Section 3.1. These particles can be linked via protein streptavidin which has high affinity to biotin situated on AuNP's surface. Since biotin is a small molecule, the interparticle distance in the streptavidin-connected AuNP dimer is defined by the size of the streptavidin and is expected to be $\sim$ 5 nm. Two 60 nm AuNPs separated by 5 nm plasmonically couple giving rise to a redshift of the plasmon peak. The calculated transversal and longitudinal modes of the scattering spectrum of two AuNPs of 60 nm separated by 5 nm are shown in Figure 4.9a. The peak related to the transversal mode corresponds to the scattering peak of a single 60 nm AuNP. This peak appears at $\sim$ 545 nm. The peak related to the longitudinal mode appears at $\sim$ 590 nm. The intensity of the longitudinal peak is higher than that of the transversal peak. Due to the small and fixed interparticle distance, the plasmonic coupling in such dimers is stronger

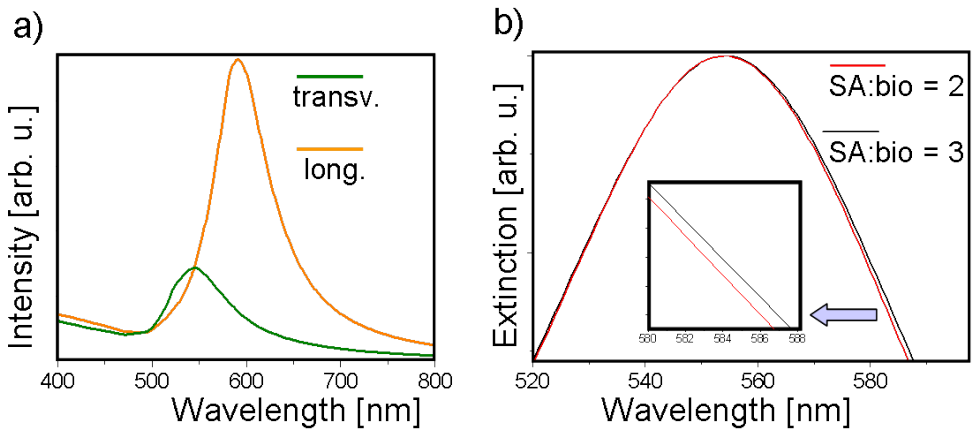

Figure 4.9: (a) Calculated scattering spectrum of AuNP dimer where each particle has a size of 60 nm and the interparticle distance is 5 nm. Transversal and longitudinal modes are shown. (b) Broadening of the extinction spectrum in bulk solution of biotinylated AuNPs upon addition of streptavidin.

and more well-defined than in the case of dimers created via the polyA-polyT link. A coupling of two biotin-decorated AuNPs via streptavidin in the OT is therefore expected to give an intense scattering signal with a strong shift to the red end of the spectrum.

In the binding experiment, the concentration of streptavidin is very important and should be controlled precisely since low concentration leads to low binding efficiencies. If the amount of streptavidin molecules is not sufficient, the probability of AuNP binding is very low. Besides, if the amount of streptavidin molecules exceeds the required amount, the passivation of the biotin cites on the AuNP surface occurs and the binding is not likely either. To evaluate the correct concentration of streptavidin, we perform bulk experiments similar to those described in reference [110]. In these experiments, portions of solution of streptavidin are added to the hydrosol of biotinylated AuNPs in the cuvette and the extinction signal of the sample in bulk is monitored. The pH of the sample is kept at 5.5 to prevent electrostatic repulsion between the nanoparticles and induce their interaction. At the amount of streptavidin sufficient for binding, AuNPs start to aggregate and a slight broadening of the extinction peak is observed. This can

be seen in Figure 4.9b, where the ratio between the streptavidin and biotin concentration is changed from 2:1 to 3:1, red and black curves, respectively. This indicates that at a concentration ratio of 3:1, AuNP aggregation is initiated.

The relative concentrations of streptavidin to biotin used in the trapping experiments are 0:1, 2:1 and 3:1. The experimental approach to detect this process in the OT is as follows: the solution of streptavidin is injected into the droplet of the of biotinylated AuNP hydrosol under the microscope and two AuNPs are optically trapped one after another as their scattering signal is monitored. In the experiments, the laser power on the sample is $\sim$ 25 mW and the wavelength of the trapping laser is 808 nm.

With these experimental conditions, the plasmonic coupling in the OT is observed in only less than 10% of the cases. The addition of NaCl does not promote binding but results into sedimentation of particles on the surface of the cover slip. The plasmonic coupling in the OT is not observed, probably due to the fact that streptavidin molecules are freely diffusing in solution and one cannot control their arrival to the interparticle region. Another reason could be an increased heating of the nanoparticle dimer due to its high absorption cross section at 808 nm. As mentioned in the Chapter 3, the streptavidin-biotin binding is stable only below 70 ^{o}C.

One possible improvement of the expeiment would be to immmobilize streptavidin directly on half of the AuNPs present in solution. In this case, similarly to the system of AuNPs functionalized with polyA and polyT strands, for two particles situated in the OT the expected probabilily of binding would be 50%.

Gold nanostars in the OT. Due to the high field enhancement near the spikes, single Au nanostars have an excelllent performance in the Surface Enhanced Raman Scattering (SERS) spectroscopy [137, 160]. In reference [161], nanostars are arranged on the surface into arrays, which are probed as SERS-active substrates. The scanning electron micrograph of these substrates is shown in Figure 4.10a.

These substrates provide the enhancement of the Raman signal on the order of $\sim 10^5$ as compared to the star-free solution of the analyte. The SERS signal of the analyte is shown in Figure 4.10b. Similar results are reported for other SERS substrates consisting of nanostars or plasmonic particles with other

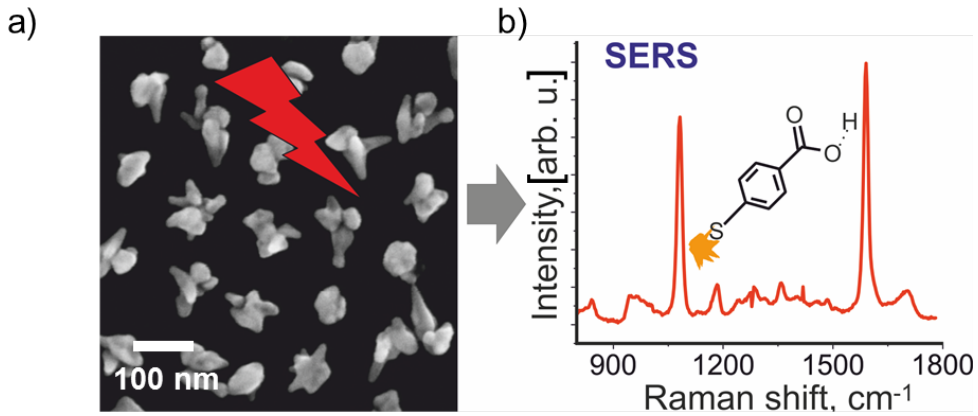

Figure 4.10: Nanostar arrays as SERS-active substrates [161]: (a) Scanning electron micrograph of nanostar array grown on the surface. The nanostars grown on the surface are roughly twice smaller than those synthesized in solution. (b) Enhancement of the Raman signal of mercaptobenzoic acid adsorbed on the surface of nanostars.

shapes arranged on a surface [162–165]. In such arrays of nanostars, the distance between the nanoparticles is larger than their size and therefore no plasmonic coupling between the particles is expected. If one, however, brought two nanostars close by means of optical trapping, plasmonic coupling between tips could occur. This plasmonic coupling would result into "hot spots" – regions between tips of nanostars where the field enhancement is higher than the sum of field enhancements of separate tips. These structures, thus, would offer a much higher field enhancement than both nanostar monomers or dimers of gold nanospheres. Optical trapping might serve as a powerful tool to allow interparticle coupling between those nanostars, as already demonstrated for spherical particles. By means of this technique it might be possible to controllably induce coupling between two tips of the nanostars and as such create region with exceptionally high field enhancements, the so called hot spots.

Nanostars dispersed in the droplet of ultrapure water under the microscope are trapped with the laser operating at 1064 nm. The power of the laser on the sample is tuned between 100 and 200 mW. With these experimental settings only 2D trapping is observed, i.e. the nanostars are confined by the cover slip

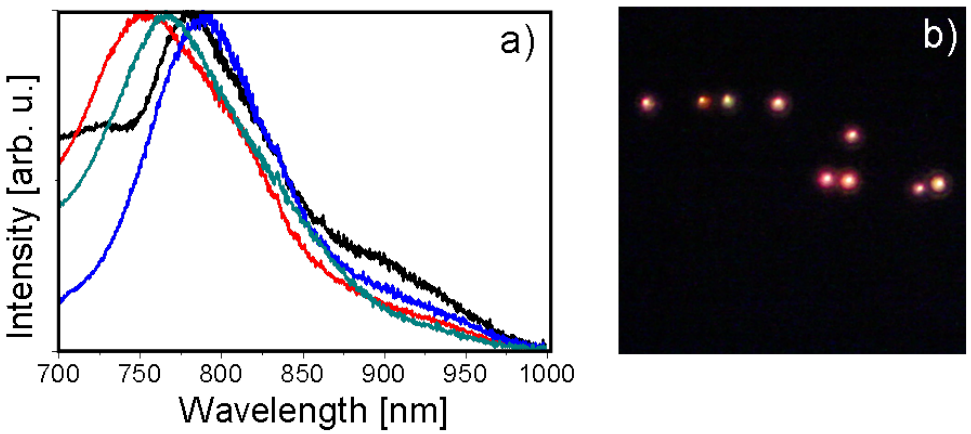

Figure 4.11: (a) Elastic scattering spectra of four different nanostars on the surface. Difference in the position of the peaks is due to the heterogeneity of the sample. (b) Dark-field image of the pattern of printed nanostars.

in the z-direction. At low laser powers (∼100 mW on the sample) the trapping does not appear stable, while at higher powers the stability of the trap increases. However, simultaneous increase in probability of particle deposition on the surface by the trapping laser is observed. At trapping powers of 200 mW on the sample nanostars are almost instantly optically printed on the cover slip. This phenomenon is known as laser printing [48]. The dark-field image of a pattern of printed nanostars is shown in Figure 4.11b.

The reason of nanostar printing at 1064 nm lies in the relative position of the plasmon resonance of the nanoparticles relative to the wavelength of the trapping laser. Plasmon resonances of nanostars in red and infrared region are observed at 775 - 780 nm and at ∼900 nm, see Figure 4.11a. Differences in the spectra are due to heterogeneity of the sample. As explained in Section 2.2, if the linearly polarized trapping laser operates near the plasmon resonance of the AuNP, the absorption and scattering cross section of the particle is very high leading to an increase of the scattering component of the optical force. This increase is more profound than the increase in the gradient component, so the total force acting on the particle is dominated by the scattering force. The scattering force is directed

along the beam propagation resulting in the deposition of the nanoparticles on the surface of the cover slip at higher powers.

Optical trapping of nanostars, therefore, is not possible at 1064 nm with a Gaussian trapping beam profile. Laser sources of the wavelengths shifted even further to the infrared (so that the trapping wavelength is far from the plasmon resonance of the nanostar) are not currently available. To create a stable optical trapping for nanostars, applying alternative trapping geometry is required. One possible solution would be to use an optical vortex trap described in [143]. In this case, the wavelength of the trapping laser is blue shifted compared to the plasmon resonance of the particle, but the trap stability is regulated by the beam shape. There is a region with a zero intensity in the center of the beam surrounded by the ring of high intensity ("doughnut" shape). The nanoparticle is therefore pushed out from the region of high intensity in the outer part of the beam and confined in its middle.

5 Accelerating FRET with gold nanoparticle dimers

The vicinity of AuNPs can have a strong effect on decay rates of fluorescent molecules. This, in turn, can influence the interactions between these molecules and change the efficiency of energy transfer between them. This chapter focuses on the studies of FRET between organic molecules and complexes situated near AuNPs. Performance of AuNP dimers in tuning the FRET is compared to the performance of AuNP monomers.

First, FRET pairs are attached to AuNP monomers and dimers, and the properties of these hybrid systems are characterized. By exciting the donor in the AuNPs/FRET pair system and detecting the acceptor fluorescence, the occurrence of FRET is proven.

The steady-state measurements reveal no difference between the FRET process in the free donor-acceptor pair and the donor-acceptor pair attached to AuNPs; therefore, time-resolved fluorescence measurements are conducted. This allows fluorescence lifetimes of donor and acceptor in different configurations to be obtained. From this data, FRET rates and efficiencies are deduced. It is shown that both single AuNPs and AuNP dimers accelerate FRET. However, AuNP dimers perform moderately better. Calculation of the field enhancement near AuNPs show that in the case of AuNP dimers both regions of field enhancement and field suppression are present. Therefore, to achieve the best performance of AuNP dimers for FRET enhancement, the precise positioning of the FRET pair in the interparticle region is necessary.

5.1 Characterization of the AuNPs/FRET pair system

Two molecules taking part in Förster resonance energy transfer (FRET) are called a FRET pair. In FRET, energy is transferred from a donor molecule to a closely situated acceptor molecule under the condition of a spectral overlap between them. In this thesis, FRET pairs consisting of donor R-phycoerythrin ($\lambda_{ex} = 542$ nm, $\lambda_{em} = 575$ nm) and acceptor Alexa fluor 647 ($\lambda_{ex} = 647$ nm, $\lambda_{em} = 661$ nm) are used. These dyes are placed near 40 nm spherical AuNPs or between two 40 nm spherical AuNPs situated close to each other. The two nanoparticles form a dimer, and the influence of the AuNPs on FRET is studied. FRET without AuNPs is compared to FRET in the presence of AuNP monomers and to FRET in the presence of AuNP dimers. To get a full picture, samples in nine configurations are investigated: gold-free donor, gold-free acceptor and gold-free FRET pair; donor on monomer, acceptor on monomer and FRET pair on monomer; donor in dimer, acceptor in dimer and FRET-pair in dimer.

Gold-free samples, used to study the FRET process in the absence of AuNPs, are obtained by dissolving 5 μl of stock solution of streptavidin attached to donor, acceptor or FRET pair in 500 μl of Mili-Q water. Samples containing AuNPs are prepared by connecting the dyes to AuNPs via streptavidin-biotin link, described in detail in Section 3.1. In the monomers, streptavidin is used only to place dyes near the gold surface, while in the AuNP dimers streptavidin simultaneously plays the role of a linker between two AuNPs.

AuNP monomers and dimers are prepared in one batch. To separate them, the gel electrophoresis procedure described in Section 3.2 is used. In Figure 5.1 the results of the gel electrophoresis procedure can be seen. The bands containing monomers, dimers and bigger aggregates are clearly distinguishable in the gel piece marked "S" (sample). In the reference run, AuNPs without addition of streptavidin are used, so that the formation of aggregates is not possible. Therefore in the gel piece marked "R" (reference) only one band corresponding to single particles is observed. The single band in the reference run confirms that the ap-

pearance of different bands in the gel piece "S" is indeed due to the presence of aggregates of different sizes and not due to the heterogeneity of the gold colloid.

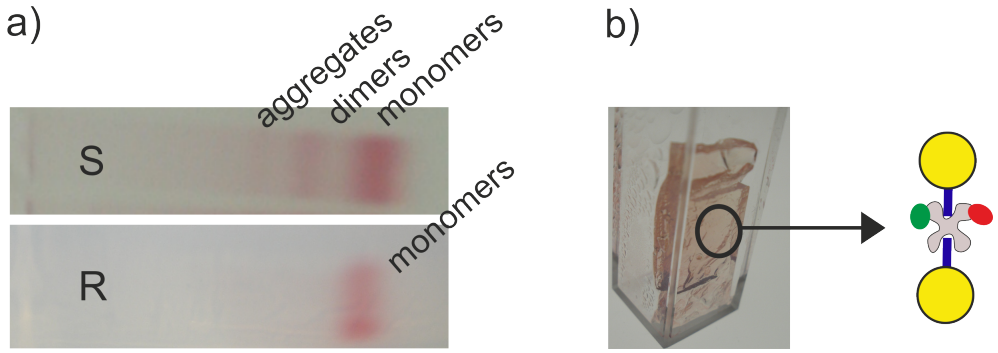

Figure 5.1: Results of the gel electrophoresis method. (a) Photograph of the gel piece with sample (S) where different bands corresponding to monomers, dimers and bigger aggregates can be seen and photograph of the gel piece with reference (R) where only one band corresponding to single particles can be seen. AuNPs absorb in green so they appear red in the transmitted light. (b) Photograph of dimer band in a cuvette and schematic of AuNP dimers connected via streptavidin with a FRET pair on it. Difference in the red colors in panel a and b originates from the settings of the camera.

After the gel electrophoresis procedure, the morphology of the particles and the yield of monomers and dimers are studied by transmission electron microscopy (TEM). For this, particles are extracted from the gel bands as described in Section 3.2 and solutions drop casted on the TEM grid are let to dry. In Figure 5.2 typical TEM image of AuNP dimer where two 40 nm AuNPs are connected via streptavidin is shown.

Analysis of TEM images of particles from dimer bands shows that those contain 65% of dimers. The average interparticle distance in the AuNP dimers is 2 nm. TEM studies show no change in the morphology of single AuNPs after the gel electrophoresis and prove that the monomer band consists almost exclusively of single particles.

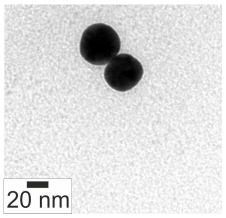

Figure 5.2: Transmission electron microscopy image of AuNP dimer consisting of two monomers of 40 nm each connected via streptavidin.

We expect the plasmon oscillations in AuNPs placed near the FRET pair to influence the FRET process. Therefore, we proceed with the characterization of the plasmonic properties of AuNP monomers and dimers. These properties are probed by elastic scattering spectroscopy of single monomer or single dimer, for which an optical microscope in the dark-field configuration (only scattered light is detected) is used. Solutions of AuNP monomers and dimers are drop casted on the cover slip and the droplets are let to dry. The concentration of the particles is low enough so that the observation of the single monomers or single nanoparticle dimers is possible.

In the scattered light single AuNPs of 40 nm size appear as a green dots due to their plasmon resonance at $\sim$ 530nm which leads to the enhanced scattering. The typical scattering spectra of 40 nm single AuNPs is shown in Figure 5.3a. The plasmonic peak is on the edge of the overlap between the fluorescence spectrum of the donor and the fluorescence excitation spectrum of the acceptor, marked in pink on the graph. In the inset, the dark-field micrograph of 40 nm AuNP is shown.

If two single AuNPs of 40 nm size are assembled into a dimer with an inter-particle distance of $\sim$ 2 nm, they appear as a red dot in the scattered light. This can be seen in the inset of Figure 5.3b, showing the micrograph of such dimer. Two particles appear as a single object due to the resolution limit of the setup. The reason for the color change is the plasmonic coupling between two AuNPs, resulting in a redshift of the plasmon resonance with respect to the scattering peak of the AuNP monomer. The scattering signal of the dimer is polarization-dependent, as can be seen in Figure 5.3b. Here, different colors

of spectra correspond to signal taken at different positions of polarization filter. The filter is turned in steps of 45^o. If the polarization direction of the incident light is aligned with the dimer's long axis, the longitudinal plasmon peak attains its maximum value. If these directions are perpendicular, the intensity of the longitudinal peak is at minimum.

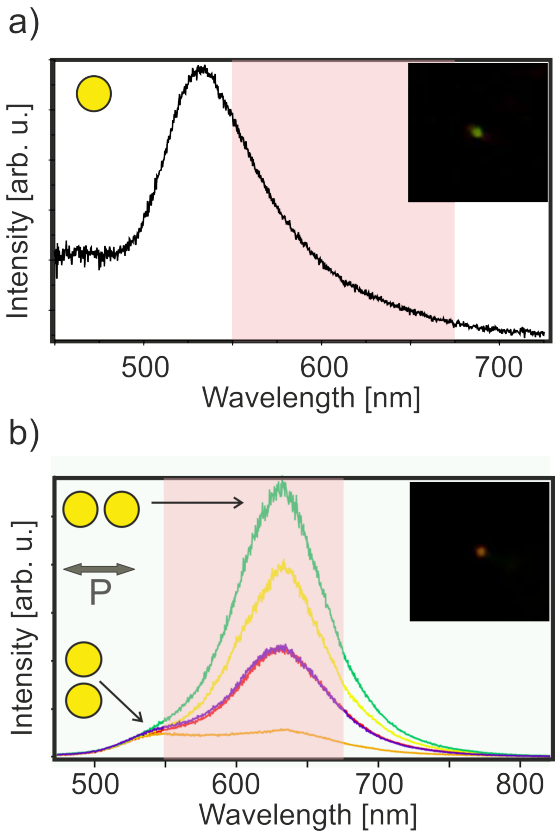

Figure 5.3: (a) Typical scattering spectrum of single AuNPs of 40 nm size. Inset: corresponding typical darkfield micrograph. (b) Typical scattering spectra of the dimer consisting of two 40 nm AuNPs. Spectra are taken at different positions of polarization filter. Inset: corresponding typical darkfield micrograph. The spectral region of the overlap between the fluorescence spectrum of the donor and the fluorescence excitation spectrum of the acceptor is marked in pink color.

In the case of AuNP dimer, the spectral position of the coupled plasmon resonance matches the region of the overlap between the fluorescence spectrum of

donor and the fluorescence excitation spectrum of the acceptor molecule. Moreover, it should be noted that the intensity of the longitudinal peak from the dimer is much higher than the intensity of the transversal peak, which corresponds to the plasmon resonance peak in the monomers. Better spectral overlap of the plasmonic response of dimers with the FRET region and the higher intensity of plasmon oscillations in dimers are both expected to be beneficial for the manipulation of FRET process with dimers as compared to AuNP monomers.

5.2 Steady-state fluorescence

To get the first insight into the influence of the AuNP dimers on the FRET between R-phycoerythrin and Alexa Fluor 647, steady-state fluorescence measurements are performed. Two systems are investigated: free FRET pairs on the streptavidin molecule and FRET pairs placed between AuNPs in the streptavidin-connected dimer. Both systems are investigated in bulk: the free FRET pairs in the form of an aqueous solution of donor and acceptor attached to streptavidin, and FRET pairs in a dimer in the form of particles dispersed in a band cut out of gel piece.

Analyzing the relative intensity of the donor and acceptor in the fluorescence responce of the FRET pair in these two configurations may give information about the change of the FRET process in the presence of the AuNP dimer. A decrease in the fluorescence intensity of the donor in a dimer band compared to the free FRET pair would suggest an increase in the efficiency of the FRET process in the presence of dimers.

For a steady-state ensemble fluorescence measurements, an excitation at 532 nm is chosen. This allows selective excitation of the donor without direct excitation of the acceptor. In Figure 5.4, the fluorescence excitation spectrum of the FRET pair, as well as fluorescence spectra of free FRET pair in solution and of the FRET pair in dimer, are shown. Spectra are normalized to the maximum. The green line shows PLE of the FRET pair. The peaks at $\sim$ 500 at $\sim$ 550 nm correspond to the excitation of the donor R-phycoerythrin while the peak at $\sim$ 650 nm corresponds to the excitation of the acceptor Alexa 647. The black line

corresponds to the PL of the FRET pair. The peak at $\sim$ 575 nm originates from the donor emission and the peak at $\sim$ 670 nm originates from the acceptor emission. The red solid line shows the PL response of the FRET conjugate situated in the AuNP dimer. The concentration of dyes in the gel piece is much lower than in free solution, which causes the signal from dimer band to appear noisy in comparison to the signal from the FRET pair in water.

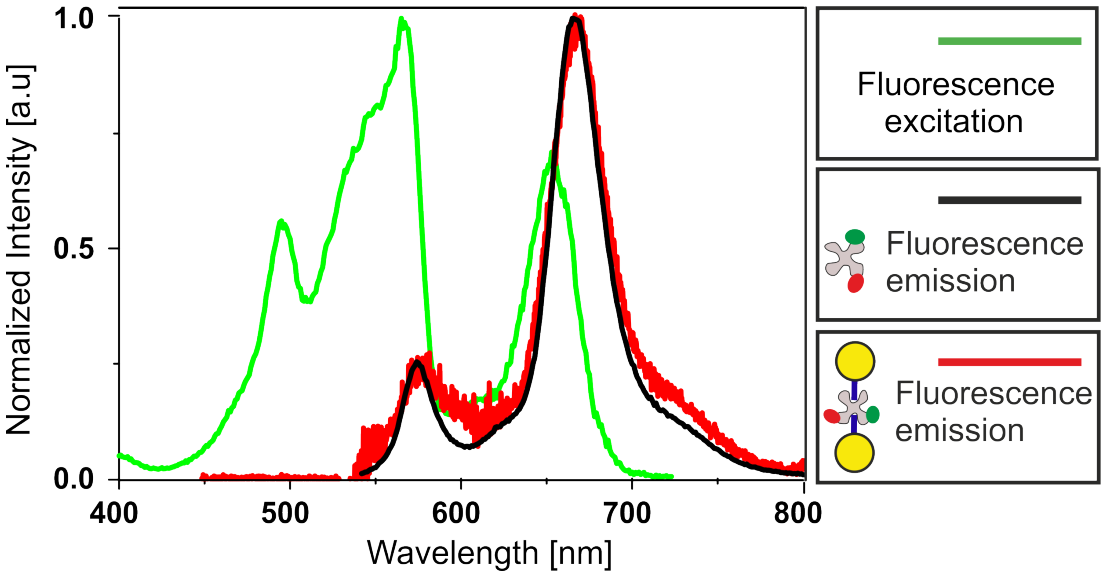

Figure 5.4: fluorescence excitation (PLE) of the FRET pair excited with λ=532 nm (green line) and fluorescence (PL) of the free FRET pair (black line) and of the FRET pair situated between two AuNPs (red line).

From spectra in Figure 5.4 two observations can be made. First, R-phycoerythrin and Alexa 647 placed in the AuNP dimer show the characteristic FRET-pair behavior. That is, upon excitation of the donor, fluorescence from the acceptor is observed (compared to the fluorescence of single components introduced in the Section 3.1). Second, the relative intensities of the donor and acceptor emission in the free FRET system and in the FRET system placed in the dimer do not differ. Therefore, the steady-state PL measurements do not reveal any influence of the AuNP dimer on the FRET process between the R-phycoerythrin and Alexa

647. To obtain more details about the FRET process in this system, we perform time-resolved fluorescence measurements.

5.3 Time-resolved fluorescence

With time-resolved fluorescence measurements, one can quantify the fluorescence decay of the donor and acceptor in the free FRET pair and in the FRET pair near AuNPs. From the fluorescence lifetimes, FRET rates and efficiencies in different configurations can be calculated. Therefore, time-resolved fluorescence is expected to give better insight in the influence of AuNPs on FRET betwen fluorescent molecules near their surface than the steady-state measurements.

For time-resolved fluorescence measurements, dimer and monomer bands are cut out of the gel piece and placed in a cuvette. The sample is excited with frequency-doubled output of the femtosecond pulsed laser. The laser excitation wavelength of 480 nm matches the fluorescence excitation peak of the donor but not the fluorescence excitation peak of the acceptor. The detected fluorescence signal is spectrally and temporally resolved by a spectrometer with a streak camera connected to it. The software of the streak camera makes it possible to separate the signal of the donor and the acceptor acquired in the same measurement. For the analysis of the decay times spectral regions of 20 nm width around the emission maximum of the donor and of the acceptor are chosen. The emission decay of the donor is analyzed between 552 and 572 nm and the emission decay of the acceptor is analyzed between 642 and 662 nm. In the data sets the decay curves of donor and acceptor are normalized to the maximum and shifted to their common starting time t=0.

First we characterize the fluorescence decay of the donor and the acceptor in free FRET pairs and in the FRET pairs placed in dimers and compare them. In Figure 5.5, the fluorescence decays of the donor and of the acceptor in two different geometries – in free FRET pair in solution and in FRET pair in AuNP dimer – are shown. In both cases, the donor shows a fast decay in the range of $\sim$ 100 picoseconds. For the acceptor, two processes are observed in both configurations: first the "build up" of the fluorescent signal occurring on the

sub-100-picosecond scale and subsequently a slower decay on the 100-picosecond scale. Therefore, it is observed that both donor and acceptor qualitatively show the same behavior in free FRET pair and in FRET pair in dimer. This holds also for the donor and acceptor connected to the monomer (data not shown). The fact that the decay of the donor and the build up of the fluorescent signal of the acceptor are on the same timescale is a proof for FRET. It is also important to mention that although the behavior of donor and acceptor do not differ between the configurations qualitatively, quantitatively they are not the same.

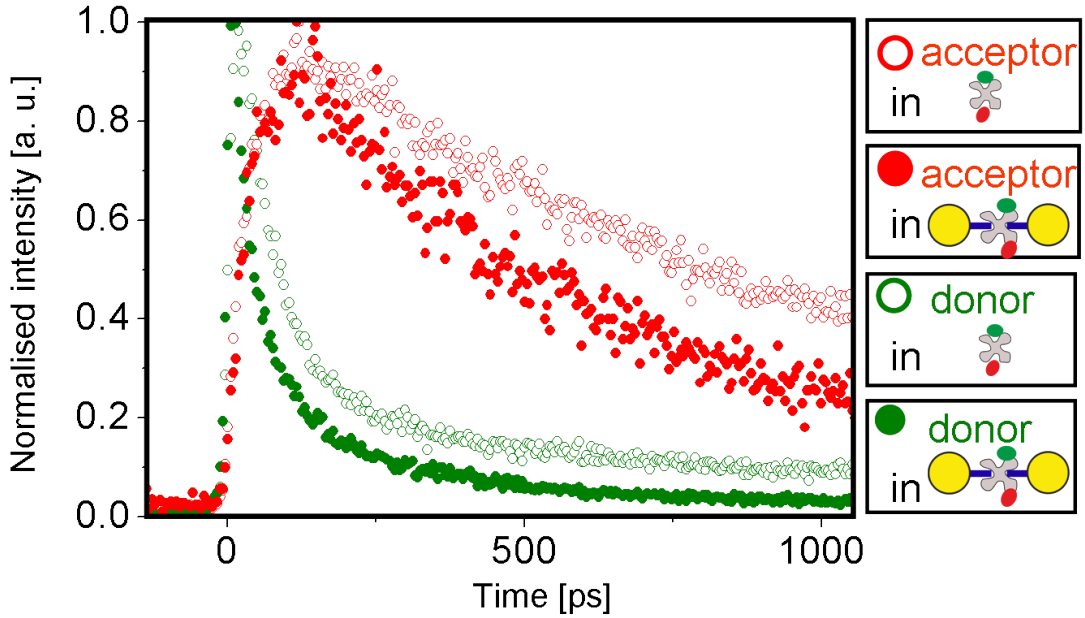

Figure 5.5: Fluorescence decay traces of acceptor and donor (open circles) in free FRET pair and of acceptor and donor in a dimer band (solid circles). Red stands for acceptor and green stands for donor.

The shape of the fluorescence decay curve of the donor needs a special discussion. In general, the fluorescence decay signal of donor, when only one type of donor is present in the system, should appear as a monoexponential decay[166]. Apparently in our studies, the fluorescence decay of the donor in the FRET pair cannot be fitted as a monoexponential function, this suggesting the existence of several different lifetimes. The existence of several different lifetimes is sometimes

explained by the presence of some fraction of the donor molecules not taking part in FRET process [167]. However, in the system investigated here the existence of different lifetimes may have a different reason. To investigate this fact we compare fluorescence decay traces of donor in different configurations as explained below.

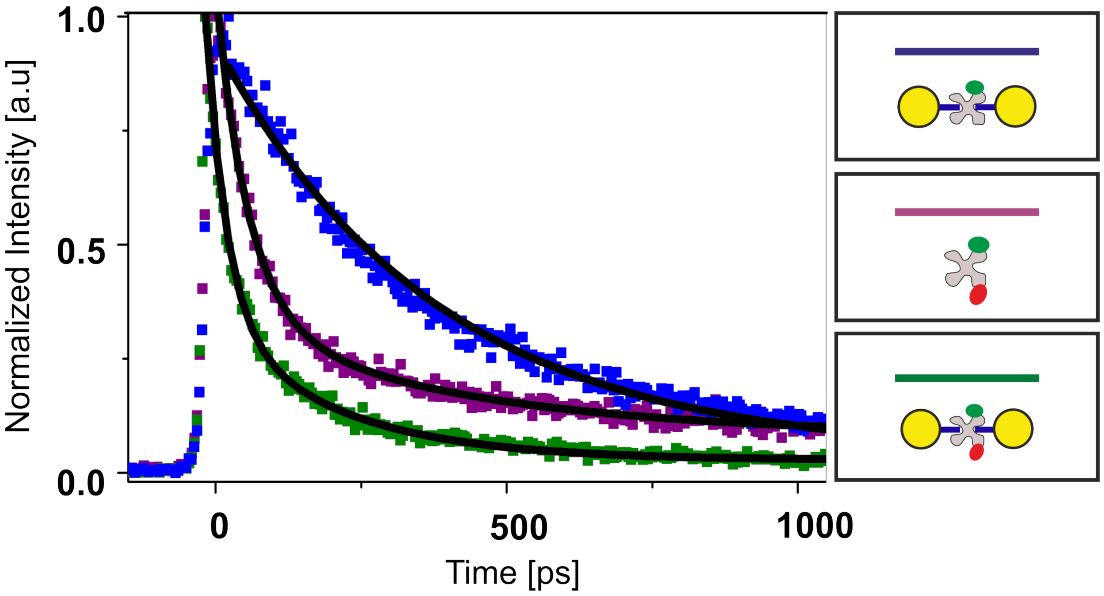

Figure 5.6: Donor fluorescence decay traces in dimers without acceptor (blue), in free FRET pairs (violet) and in FRET pairs placed in dimers (green).

Figure 5.6 shows the donor fluorescence decay curves of donor molecules situated in dimers, free FRET pairs and of the FRET pair in dimer. The donor decay is modeled by a biexponential function $y = Ae^{\frac{\tau}{B}} + Ce^{\frac{\tau}{D}}$. It can be seen that both components of the biexponential decay of the donor change upon addition of the acceptor as well as upon placement of the conjugate in a dimer, which proves that both time components are taking part in FRET. We suggest that the biexponential behavior can be explained by inhomogeneity of the sample. As discussed in Section 2.4, the fluorescence of dyes near the metal surface depends on the distance between the molecules from the surface of AuNPs and on the relative orientations of them. Since we do not have precise control on these factors, monoexponential decay cannot be expected.

Furthermore we quantify the fluorescent lifetimes of the donors in two different configurations – with and without the acceptor. This is done for three different cases: free donor or FRET pair, donor or FRET pair situated near the monomer and donor or FRET pair situated in the dimer. So, in total, there are six different samples for which the fluorescence decay of the donor is quantified. For this the fluorescence life-times are calculated as the amplitude-weighted averages from the biexponential decay curves similarly to [118]. The results of these calculations are summarized in Table 5.1. The lifetime of the donor in the presence of acceptor is referred to as τ_{DA} and the lifetime of the donor in the absence of the acceptor is referred to as τ_D. For donor-only configurations, the lifetime decrease from 2670 ps in water to 460 ps in the monomer and dimer bands is observed. This decrease of lifetime can be attributed to the fluorescence quenching by AuNP. Hence the degree of quenching by monomer and dimer is the same.

Sample	τ_D in ps	τ_{DA} in ps
Free FRET pair	2670	350
FRET pair on monomer	460	96
FRET pair in dimer	460	82

Table 5.1: Fluorescence lifetime of the donor in the absence of the acceptor τ_D and fluorescence lifetime of the donor in the presence of the acceptor τ_{DA} in different configurations.

In the presence of the acceptor, the donor lifetimes decrease from 350 ps in the free FRET pair through the 96 ps in the monomer band to 82 ps in the dimer band. We can therefore see the acceleration of the fluorescence decay of the donor both upon addition of acceptor and upon placing the donor near metal nanoparticles.

5.4 FRET rates and efficiencies in different configurations

FRET rates k and efficiencies E in different configurations are calculated from the lifetimes according to the expressions $k_{fret} = \frac{1}{\tau_{DA}} - \frac{1}{\tau_D}$ and $E = 1 - \frac{\tau_{DA}}{\tau_D}$. Here

τ_D includes all the decay processes that do not contribute to FRET because it is measured in the absence of the acceptor. The calculated rates and efficiencies for the different configurations are summarized in Table 5.2.

Sample	k_{FRET} [ns^{-1}]	E [%]
Free FRET pair	2.5	87
FRET pair on monomer	8	80
FRET pair in dimer	10	80

Table 5.2: FRET rates and efficiencies in different configurations.

It can be concluded that upon attachment to AuNPs, FRET efficiencies stay stable and high. FRET rates increase from 2.5 ns^{-1} in free FRET pair to 8 ns^{-1} in FRET pair near AuNP monomer and to 10 ns^{-1} in FRET pair placed in AuNP dimer.

5.4.1 Calculation of the FRET enhancement

Since a straightforward conclusion about the performance of AuNP dimers for FRET compared to AuNP monomers can not be made from the data discussed above, calculation of the intensity enhancement for the electromagnetic field for both monomers and dimers based on generalized Mie theory is performed. In the geometrical model used in this calculation, AuNP dimer consists of two AuNPs with the radius of 20 nm each placed at 4 nm distance form each other. The oscillating dipole representing a fluorescent molecule is placed 2 nm away from AuNP and is situated radially to its surface. The emission wavelength of the dipole is chosen to be λ=600 nm.

In Figure 5.7, the result of the FRET enhancement calculation is shown. For both monomers and dimers, not only can the regions of enhancement be seen, but also regions of intensity suppression. Intensity enhancement up to seven times is possible and the enhancement regions are clearly larger than the suppression regions. Averaging over a square at the position of dipole in panels a and b in Figure 5.7 yields average FRET rate enhancements of 8% and 25% for AuNP monomers and dimers, respectively. This is consistent with experimental results discussed above.

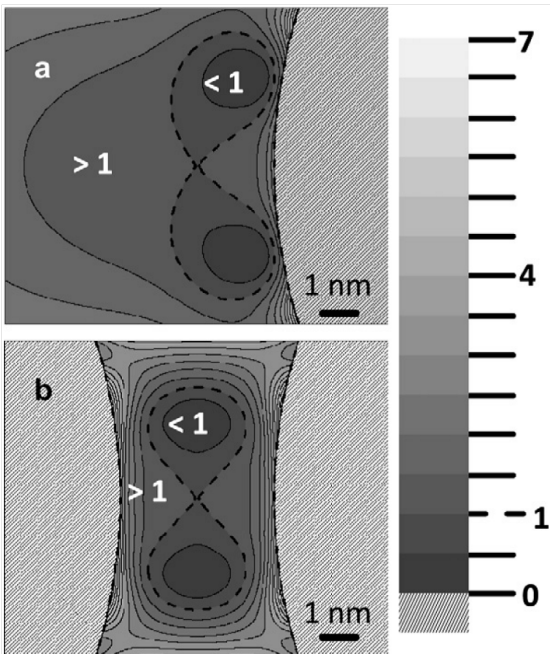

Figure 5.7: a) Zoom-in into the FRET rate enhancement distribution (a) near the surface of gold monomer and (b) in the hot spot of the AuNP dimer. The plane where the emitting dipole is situated is shown. Surfaces of AuNPs are seen as a light gray convex objects. Regions of the intensity enhancement are indicated by >1; regions of the intensity suppression are indicated by <1. Calculation was performed by Dr. C. Hrelescu

Therefore it can be seen that FRET is influenced in the presence of AuNPs and that AuNP dimers have higher potential for FRET enhancement than AuNP monomers. In practice, the precise positioning of the FRET pair in AuNP dimer is necessary to make full use of the superior performance of AuNP dimers. Since the full control over the position is not feasible yet, the experimental data show only slightly higher performance of AuNP dimers.

6 Conclusions and outlook

The aim of this thesis is to manipulate interactions between molecules by plasmonic properties of AuNPs situated in their vicinity. The focus is on the particular configuration of the system where interacting molecules are confined between two spherical AuNPs forming a dimer. Two types of intermolecular processes are investigated - the formation of DNA double strands and the energy transfer between fluorescent molecules. In both cases, it is shown that the interactions between molecules can be actively tuned using plasmonic properties of AuNPs attached to them.

In the first part of this thesis, formation of DNA double strands in the vicinity of AuNPs is manipulated. Hybridization of DNA single strands is actively tuned by plasmonic nanoparticles in the optical trap for the first time. Using laser light, single AuNPs decorated with poly thymine DNA strands are brought close to single AuNPs decorated with poly adenine strands and their interaction is monitored. When situated near each other, the AuNPs bind due to the hybridization of complementary DNA strands on their surfaces. We show that the detection of this binding can be done by registering the change of the plasmonic properties of AuNP dimers in the bound versus the unbound state. Namely, at small interparticle distances, the redshift of the scattering peak of the bound AuNP pair is observed by the naked eye.

Based on this detection method we measure the hybridization times for single AuNP dimers in the OT. By increasing the power of the trapping laser from 121 to 170 mW, we tune the median binding time from 0.93 to 26.2 seconds, i.e., an increase by more than an order of magnitude is achieved. The observed increase in the binding time at higher laser powers is explained with the semi-quantitative model where the calculated temperatures near AuNPs due to the plasmonic heating are compared to the calculated temperatures required for the DNA double

strand dissociation. Since AuNP dimer is connected via poly adenine and poly thymine chains, different connecting in different configurations and sliding along the connection is possible. By increasing the temperature near AuNPs via plasmonic heating, the system is brought closer to the dissociation temperature and the formation of loosely bound dimers is suppressed. Therefore more time is needed to establish the stable connection.

To prove that the observed binding between AuNPs is taking place due to the chemical affinity of the complementary DNA strands on nanoparticle's surface, several series of control experiments are conducted. These control experiments confirm that at the conditions used to measure the hybridization times, unspecific binding between AuNPs can be neglected and binding should be attributed indeed to the chemical affinity between complementary AuNPs.

In the AuNP/DNA system described above, AuNPs are decorated with poly adenine and poly thymine chains. One future development of the system would be to consider DNA strands of specific sequence or to use the sequences which are only partly complementary. This would exclude the possibility of sliding and make only one binding configuration possible. The studies of binding kinetics in such systems on the single-dimer level in the OT might give insights into the exact mechanism of connection between two DNA strands.

Moreover, DNA-bound AuNPs in the optical trap could be used in field-enhanced spectroscopy. Interparticle regions provide high field enhancemnts [159], but unfunctionalized AuNPs in the optical trap can not build a stable dimer since AuNPs might uncontrollably approach each other [144]. Dense DNA coverage prevents AuNPs from mechanical interaction. Stable DNA-connected AuNP dimer in the OT would represent a mobile region of field enhacement for scanning the solution volume. Alternatively an analyte molecule could be fixed in the interparticle region via chemical attachement to DNA strands.

Manipulating biomolecular binding events with plasmonic nanoparticles could also find potential application in lab-on-a-chip devices, where macroscopic control of chemical reactions inside the microfluidic channels is difficult due to laminar flow. Plasmonic nanoparticles which could be moved between parallel flows by means of optical trap would serve as optically-driven mobile reaction actuators and increase the functionality of lab-on-a-chip systems.

In the second part of this thesis, FRET between fluorescent molecules in the vicinity of AuNPs is studied. For this, AuNP monomers and dimers decorated with fluorescent dyes taking part in FRET are prepared. The optical properties and morphology of monomers and dimers with the FRET pair are characterized on the single-particle level. It is shown that the region of the plasmon resonance of AuNP dimers has larger overlap with the FRET spectral region compared to AuNP monomers. Therefore higher influence on FRET is expected for dimers as compared to AuNP monomers. Steady-state fluorescence measurements confirm FRET between fluorescent dyes near nanoparticles but do not reveal any difference between FRET in the absence or in the presence of AuNPs.

Deeper insight into the FRET near AuNP monomers and dimers is obtained with time-resolved fluorescence measurements. The fluorescnence decay times of the energy donor and energy acceptor deduced from these measurements are used to calculate FRET rates and efficiencies in different configurations. It is observed that FRET efficiencies near AuNPs stay as high as those observed for the free FRET pair. At the same time, FRET rates are considerably influenced by the presence of AuNPs. While for the free FRET pair the FRET rate is 2.5 s^{-1}, the FRET pair near monomer and dimer show the FRET rates of 8 s^{-1} and 10 s^{-1}, respectively. Therefore, the acceleration of FRET in AuNP dimer is slightly higher as compared to AuNP monomer.

Calculations of field enhancement distribution in the center of AuNP dimers qualitatively support the experimental findings. According to these calculations, there is a distribution of regions of field enhancement and suppression in the interparticle region. Although the total area of enhancement regions is larger, control of the precise positioning of donor and acceptor molecules is necessary to fully explore the potential of AuNP dimers for FRET enhancement.

Plasmonic acceleration of FRET process could be used to improve the performance of FRET-based dye-sesnsitized solar cells as well as the performance of spectroscopic and microscopic techniques based on FRET process. Since faster FRET decreases the time which donor molecules spend in the excited state, the photostability of these molecules is increased.

References

[1] R. Britten and E. H. Davidson. **Studies on nucleic acid reassociation kinetics: empirical equations describing DNA reassociation**. *Proceedings of the National Academy of Sciences of the United States of America*, **73**:415–419, 1976.

[2] A. A. Travers. **DNA Conformation and Protein Binding**. *Annual Review of Biochemistry*, **58**:427–452, 1989.

[3] D. Rapp and T. Kassal. **Theory of vibrational energy transfer between simple molecules in nonreactive collisions**. *Chemical Reviews*, **69**:61–102, 1969.

[4] N. L. Vekshin. *Energy Transfer in Macromolecules*. SPIE – The International Society for Optical Engineering, Washington, 1997.

[5] P. Nelson. *Biological Physics: Energy, Information, Life*. WH Freeman and Co, New York, 2013.

[6] I. Schoen, H. Krammer, and D. Braun. **Hybridization kinetics is different inside cells**. *Proceedings of the National Academy of Sciences of the United States of America*, **106**:21649–21654, 2009.

[7] M. J. Rust, M. Bates, and X. Zhuang. **Sub-diffraction-limit imaging by stochastic optical reconstruction microscopy (STORM)**. *Nature Methods*, **3**:793–796, 2006.

[8] E. Betzig, G. H. Patterson, R. Sougrat, W. Lindwasser, S. Olenych, J. S. Bonifacino, M. W. Davidson, J. Lippincott-

Schwartz, and H. F. Hess. **Imaging Intracellular Fluorescent Proteins at Nanometer Resolution**. *Science*, **313**:1642–1645, 2006.

[9] F Moresco, G Meyer, K.-H. Rieder, H. Tang, A. Gourdon, and C. Joachim. **Conformational Changes of Single Molecules Induced by Scanning Tunneling Microscopy Manipulation: A Route to Molecular Switching**. *Physical Review Letters*, **86**:672–675, 2001.

[10] M. D. Wang, H. Yin, R. Landick, and S. M. Gelles, J. Block. **Stretching DNA with Optical Tweezers**. *Biophysical Methods*, **72**:1335–1346, 1997.

[11] T. Perkins, S. Quake, D. Smith, and S. Chu. **Relaxation of a single DNA molecule observed by optical microscopy**. *Science*, **264**:822–826, 1994.

[12] A. O. Govorov and H. H. Richardson. **Generating heat with metal nanoparticles**. *Nano Today*, **2**:30–38, 2007.

[13] A. Kyrsting, P. M. Bendix, D. G. Stamou, and L. B. Oddershede. **Heat Profiling of Three-dimensionally Optically Trapped Gold Nanoparticles using Vesicle Cargo Release**. *Nano Letters*, **11**:888–892, 2010.

[14] S. Eustis and M. A. El-Sayed. **Why Gold Nanoparticles are More Precious than Pretty Gold: Noble Metal Surface Plasmon Resonance and its Enhancement of the Radiative and Nonradiative Properties of Nanocrystals of Different Shapes**. *Chemical Society Reviews*, **35**:209–217, 2006.

[15] O. L. Muskens, V. Giannini, J. A. Sanchez-Gil, and J. Gomez Rivas. **Strong Enhancement of the Radiative Decay Rate of Emitters by Single Plasmonic Nanoantennas**. *Nano Letters*, **7**:2871–2875, 2007.

[16] Z. Zhang, P. Yang, H. Xu, and H. Zheng. **Surface enhanced fluorescence and Raman scattering by gold nanoparticle dimers and trimers**. *Journal of Applied Physics*, **113**:033102, 2013.

[17] M. Ringler, A. Schwemer, M. Wunderlich, A. Nichtl, K. Kürzinger, T. A. Klar, and J. Feldmann. **Shaping Emission Spectra of Fluorescent Molecules with Single Plasmonic Nanoresonators**. *Physical Review Letters*, **100**:203002, 2008.

[18] C. A. Mirkin, R. L. Letsinger, R. C. Mucic, and J. J. Storhoff. **A DNA-based method for rationally assembling nanoparticles into macroscopic materials**. *Nature*, **382**:607–609, 1996.

[19] J. Stehr, C. Hrelescu, R. A. Sperling, G. Raschke, M. Wunderlich, A. Nichtl, D. Heindl, K. Kürzinger, W. J. Parak, and T. A. Klar. **Gold Nanostoves for Microsecond DNA Melting analysis**. *Nano Letters*, **8**:619–623, 2008.

[20] A. Govorov, J. Lee, and N. Kotov. **Theory of plasmon-enhanced Förster energy transfer in optically excited semiconductor and metal nanoparticles**. *Physical Review B*, **76**:125308, 2007.

[21] G. P. Acuna, F. M. Moller, P. Holzmeister, S. Beater, B. Lalkens, and P. Tinnefeld. **Fluorescence Enhancement at Docking Sites of DNA-Directed Self-Assembled Nanoantennas**. *Science*, **338**:506–510, 2012.

[22] C. G. Khoury and T. Vo-Dinh. **Gold Nanostars For Surface-Enhanced Raman Scattering: Synthesis, Characterization and Optimization**. *Journal of Physical Chemistry C*, **112**:18849–18859, 2008.

[23] M. A. van Dijk, M. Lippitz, and M. Orrit. **Far-Field Optical Microscopy of Single Metal Nanoparticles**. *Accounts of Chemical Research*, **38**:594–601, 2005.

[24] U. Kreibig and M. Volmer. *Optical properties of metal clusters*. Springer, New York, 1995.

[25] M. Dienerowitz. *Plasmonic effects upon optical trapping of metal nanoparticles*. PhD thesis, Faculty of Physics, University of St Andrews, St Andrews, 2010.

[26] R. H. Ritchie. **Plasma Losses by Fast Electrons in Thin Films**. *Physical Review*, **106**:874–881, 1957.

[27] C.F. Bohren and D.R. Huffman. *Absorption and scattering of light by small particles*. Willey-VCH, Weinheim, 2004.

[28] S.A. Maier. *Plasmonics: Fundamentals and Applications*. Springer, New York, 2007.

[29] P. B. Johnson and R. W. Christy. **Optical Constants of the Noble Metals**. *Physical Review B*, **6**:4370–4379, 1972.

[30] T. Klar, E. Dulkeith, and J. Feldmann. *"Time resolved fluorescence measurements of fluorophores close to metal nanoparticles" in "Radiative Decay Engineering" edited by R. J. Lackowicz and C. D. Geddes*. Springer Science+Business Media, LLC, New York, 2005.

[31] M. Hasegawa and M. Watabe. **Theory of Plasmon Damping in Metals. I. General Formulation and Application to an Electron Gas**. *Journal of Physical Society of Japan*, **27**:1393–1414, 1969.

[32] S. Link and M. A. El-Sayed. **Size and Temperature Dependence of the Plasmon Absorption of Colloidal Gold Nanoparticles**. *The Journal of Physical Chemistry B*, **103**:4212–4217, 1999.

[33] V. Myroshnychenko, J. Rodriguez-Fernandez, I. Pastoriza-Santos, A. M. Funston, C. Novo, P. Mulvaney, L. M. Liz-Marzan, and F. J. Garcia de Abajo. **Modelling the optical response of gold nanoparticles**. *Chemical Society Reviews*, **37**:1792–1805, 2008.

[34] H.C. van de Hulst. *Light scattering by small particles*. Dover Publications, New York, 1981.

[35] K.-H. Su, Q.-H. Wei, X. Zhang, J. J. Mock, D. R. Smith, and S. Schultz. **Interparticle Coupling Effects on Plasmon Resonances of Nanogold Particles**. *Nano Letters*, **3**:1087–1090, 2003.

[36] P. J. Schuck, D. P. Fromm, A. Sundaramurthy, G. S. Kino, and W. E. Moerner. **Improving the Mismatch Between light and Nanoscale Objects with Gold Bowtie Nanoantennas**. *Physical Review Letters*, **94**:017402, 2005.

[37] P. K. Jain and M. A. El-Sayed. **Plasmonic coupling in noble metal nanostructures**. *Chemical Physics Letters*, **487**:153–164, 2010.

[38] L. Gunnarsson, T. Rindzevicius, J. Prikulis, B. Kasemo, M. Käll, S. Zou, and G. C. Schatz. **Confined Plasmons in Nanofabricated Single Silver Particle Pairs: Experimental Observations of Strong Interparticle Interactions**. *Journal of Physical Chemistry B*, **109**:1079–1087, 2005.

[39] W. Rechberger, A. Hohenau, A. Leitner, J.R. Krenn, B. Lamprecht, and F.R. Aussenegg. **Optical properties of two interacting gold nanoparticles**. *Optics Communications*, **220**:137 – 141, 2003.

[40] P. K. Jain, W. Huang, and M. A. El-Sayed. **On the Universal Scaling Behavior of the Distance Decay of Plasmon Coupling in Metal Nanoparticle Pairs: A Plasmon Ruler Equation**. *Nano Letters*, **7**:2080–2088, 2007.

[41] J. M. Gérardy and M. Ausloos. **Absorption spectrum of clusters of spheres from the general solution of Maxwell's equations. II. Optical properties of aggregated metal spheres**. *Physical Review B*, **25**:4204–4229, 1982.

[42] **MQMie 2.4 User Guide.** M. Quninten. Aldenhoven, 2004.

[43] A. Ashkin. **Acceleration and Trapping of Particles by Radiation Pressure**. *Physical Review Letters*, **24**:156–159, 1970.

[44] K. Neuman and S. Block. **Optical trapping**. *Review of Scientific Instruments*, **75**:2787–2809, 2004.

[45] K. Dholakia, P. Reece, and M. Gu. **Optical micromanipulation**. *Chemical Society Reviews*, **37**:42–55, 2008.

[46] T. L Min, P. J. Mears, L. M. Chubiz, C. V. Rao, I. Golding, and Y. R. Chemla. **High-resolution, long-term characterization of bacterial motility using optical tweezers**. *Nature Methods*, **6**:831–835, 2009.

[47] A. Ohlinger, A. Deak, A. A. Lutich, and J. Feldmann. **Optically Trapped Gold Nanoparticle Enables Listening at the Microscale**. *Physical Review Letters*, **108**:018101, 2012.

[48] A. S. Urban, A. A. Lutich, F. D. Stefani, and J. Feldmann. **Laser Printing Single Gold Nanoparticles**. *Nano Letters*, **10**:4794–4798, 2010.

[49] H. Kuwata, H. Tamaru, K. Esumi, and K. Miyano. **Resonant light scattering from metal nanoparticles: Practical analysis beyond Rayleigh approximation**. *Applied Physics Letters*, **83**:4625–4627, 2003.

[50] R. R. Agayan, F. Gittes, R. Kopelman, and C. Schmidt. **Optical trapping near resonance absorption**. *Applied Optics*, **41**:2318–2327, 2002.

[51] C. R. Calladine, H. Drew, B. Luisi, and A. Travers. *Understanding DNA: The Molecule and How it Works*. Elseviewer Academic Press, New York, 2004.

[52] J. D. Watson and F. H. C. Crick. **Molecular Structure of Nucleic Acids: A Structure for Deoxyribose Nucleic Acid**. *Nature*, **171**:737–738, 1953.

[53] D. Bikard, C. Loot, Z Baharoglu, and D. Mazel. **Folded DNA in Action: Hairpin Formation and Biological Functions in Prokaryotes**. *The Journal of Biological Chemistry*, **74**:570–588, 2010.

[54] A. Szabo, K. Schulten, and Z. Schulten. **First passage time approach to diffusion controlled reactions**. *Journal of Chemical Physics*, **72**:4350–4357, 1980.

[55] P. Qu, X. Yang, X. Li, X. Zhou, and X. S. Zhao. **Direct Measurement of the Rates and Barriers on Forward and Reverse Diffusions of Intramolecular Collision in Overhang Oligonucleotides**. *The Journal of Physical Chemistry B*, **114**:8235–8243, 2010.

[56] Y. Yin and X. S. Zhao. **Kinetics and Dynamics of DNA Hybridization**. *Accounts of Chemical Research*, **44**:1172–1181, 2011.

[57] M. I. Wallace, L. Ying, S. Balasubramanian, and D. Klenerman. **Non-Arrhenius kinetics for the loop closure of a DNA hairpin**. *Proceedings of the National Academy of Sciences of the United States of America*, **98**:5584–5589, 2001.

[58] D. Pörschke and M. Eigen. **Co-operative non-enzymatic base recognition III. Kinetics of the helix–coil transition of the oligoribouridylic-oligoriboadenylic acid system and of oligoriboadenylic acid alone at acidic pH**. *Journal of Molecular Biology*, **62**:361–381, 1971.

[59] X.-B. Gu, S.-i. Nakano, and N. Sugimoto. **Consecutive GC base pairs determine the energy barrier of DNA duplex formation under molecularly crowded conditions**. *Journal of Nanobiotechnology*, **10**:8, 2012.

[60] M.E. Craig, D. M. Crothers, and P. Doty. **Relaxation Kinetics of Dimer Formation by Self Complimentary Oligonucleotides**. *Journal of Molecular Biology*, **62**:383–401, 1971.

[61] D. Pörschke, O. C. Uhlenbeck, and F. H. Martin. **Thermodynamics and kinetics of the helix-coil transition of oligomers containing GC base pairs**. *Biopolymers*, **12**:1313–1335, 1973.

[62] L. E. Morrison and L. M. Stols. **Sensitive fluorescence-based thermodynamic and kinetic measurements of DNA hybridization in solution**. *Biochemistry*, **32**:3095–3104, 1993.

[63] C. Chen, W. Wang, Z. Wang, F. Wei, and X. S. Zhao. **Influence of secondary structure on kinetics and reaction mechanism of DNA hybridization**. *Nucleic Acids Research*, **35**:2875–2884, 2007.

[64] R. Owczarzy, Y. You, B. G. Moreira, J. A. Manthey, L. Huang, M. A. Behlke, and J. A. Walder. **Effects of Sodium Ions on DNA Duplex Oligomers: Improved Predictions of Melting Temperatures**. *Biochemistry*, **43**:3537–3554, 2004.

[65] R. H. Garrett and C. M. Grisham. *Biochemistry*. Cengage Learning, 2007.

[66] P.N. Borer, B. Dengler, I. Tinoco, and O.C. Uhlenbeck. **Stability of Ribonucleic acid Double-stranded Helices**. *Journal of Molecular Biology*, **86**:843–853, 1974.

[67] J. SantaLucia. **A Unified View of Polymer, Dumbbell, and Oligonucleotide DNA Nearest-neighbor Thermodynamics**. *Proceedings of the National Academy of Sciences of the United States of America*, **95**:1460–1465, 1998.

[68] D. M. Crothers and B. H. Zimm. **Theory of the Melting Transition of Synthetic Polynucleotides: Evaluation of the Stacking Free Energy**. *Journal of Molecular Biology*, **9**:1–9, 1964.

[69] D. M. Gray and I. Tinoco. **A New Approach to the Study of Sequence-dependent Properties of Polynucleotides**. *Biopolymers*, **9**:223–244, 1970.

[70] O. Gotoh and Y. Tagashira. **Stabilities of nearest-neighbor doublets in double-helical DNA determined by fitting calculated melting profiles to observed profiles**. *Biopolymers*, **20**:1033–1042, 1981.

[71] S. G. Delcourt and R. D. Blake. **Stacking Energies in DNA**. *The Journal of Biological Chemistry*, **266**:15160–15169, 1991.

[72] M. J. Doktycz, R. F. Goldstein, T. M. Paner, F. J. Gallo, and A. S. Benight. **Studies of DNA dumbbells. I. Melting curves of 17 DNA dumbbells with different duplex stem sequences linked by T4 endloops: Evaluation of the nearest-neighbor stacking interactions in DNA**. *Biopolymers*, **32**:849–864, 1992.

[73] N. Sugimoto, S.-i. Nakano, M. Yoneyama, and K.-i. Honda. **Improved thermodynamic parameters and helix initiation factor to predict stability of DNA duplexes**. *Nucleic Acids Research*, **24**:4501–4505, 1996.

[74] A. Wax and K. Sokolov. **Molecular imaging and darkfield microspectroscopy of live cells using gold plasmonic nanoparticles**. *Laser & Photonics Reviews*, **3**:146–158, 2009.

[75] P. Ghosh, G. Han, M. De, C. K. Kim, and V. M. Rotello. **Gold nanoparticles in delivery applications**. *Advanced drug delivery reviews*, **60**:1307–1315, 2008.

[76] M. Thomas and A. M. Klibanov. **Conjugation to gold nanoparticles enhances polyethylenimine's transfer of plasmid DNA into mammalian cells**. *Proceedings of the National Academy of Sciences of the United States of America*, **100**:9138–9143, 2003.

[77] M. P. Busson, B. Rolly, B. Stout, N. Bonod, E. Larquet, A. Polman, and B. Sebastien. **Optical and Topological Characterization of Gold Nanoparticle Dimers linked by a Single DNA Double Strand**. *Nano Letters*, **11**:5060–5065, 2011.

[78] L. H. Tan, H. Xing, H. Chen, and Y. Lu. **Facile and Efficient preparation of Anisotropic DNA-Functionalized Gold Nanoparticles and Their Regioselective Assembly**. *Journal of the American Chemical Society*, **135**:17675–17678, 2013.

[79] S. Y. Park, A. K. R. Lytton-Jean, L. Byeongdu, S. Weigand, G. C. Schatz, and C. A. Mirkin. **DNA-programmable nanoparticle crystallization**. *Nature*, **451**:553–556, 2008.

[80] L. Li and Y. Lu. *"Functional DNA-integrated nanomaterials for biosensing" in "DNA Nanotechnology: From Structure to Function" edited by C. Fan.* Springer Science+Business Media, LLC, New York, 2005.

[81] B. Padmawathy, K. R. Vinoth, and B. M. Jaffar Ali. **A direct detection of Escherichia coli genomic DNA using gold nanoprobes**. *Journal of Nanobiotechnology*, **10**:e8, 2012.

[82] D. Zhang, M. C. Huarng, and E. C. Alocilja. **A multiplex nanoparticle-based bio-barcoded DNA sensor for the simultaneous detection of multiple pathogens**. *Biosensors and bioelectronics*, **26**:1736–1742, 2010.

[83] D. Zhang, D. J. Carr, and E. C. Alocilja. **Fluorescent biobarcode DNA assay for the detection of Salmonella enterica serovar Enteritidis**. *Biosensors and bioelectronics*, **24**:1377–1381, 2009.

[84] T. A. Taton, C. A. Mirkin, and R. L. Letsinger. **Scanometric DNA Array Detection with Nanoparticle Probes**. *Science*, **289**:1757–1760, 2000.

[85] G. T. Hermanson. *Bioconjugate Techniques*. Elsevier, London, 2008.

[86] W. J. Parak, T. Pellegrino, C. M. Micheel, D. Gerion, S. C. Williams, and A. P. Alivisatos. **Conformation of Oligonucleotides Attached to Gold Nanocrystals Probed by Gel Electrophoresis**. *Nano Letters*, **3**:33–36, 2003.

[87] H. Takahashi, Y. Niidome, and S. Yamada. **Controlled release of plasmid DNA from gold nanorods induced by pulsed near-infrared light**. *Chemical Communications*, **17**:2247–2249, 2005.

[88] C. C. Chen, Y. P. Lin, C. W. Wang, H. C. Tzeng, C. H. Wu, Y. C. Chen, C. P. Chen, L. C. Chen, and Y. C. Wu. **DNA-Gold Nanorod Conjugates for Remote Control of Localized Gene Expression by near Infrared Irradiation**. *Journal of the American Chemical Society*, **128**:3709–3715, 2006.

[89] R. Elghanian, J. J. Storhoff, R. C. Mucic, R. L. Letsinger, and C. A. Mirkin. **Selective Colorimetric Detection of Polynucleotides Based on the Distance-Dependent Optical Properties of Gold Nanoparticles**. *Science*, **277**:1078–1081, 1997.

[90] M. J. Hoefert, E.J. Sambriski, and J. R. de Pablo. **Molecular pathways in DNA-DNA hybridization of surface-bound oligonucleotides**. *Soft Matter*, **7**:560–566, 2010.

[91] K. A. Peterlinz, R. M. Georgiadis, T. M. Herne, and M. J. Tarlov. **Observation of Hybridization and Dehybridization of Thiol-Tethered DNA Using Two-Color Surface Plasmon Resonance Spectroscopy**. *Journal of the American Chemical Society*, **119**:3401–3402, 1997.

[92] R. Meunier-Prest, S. Raveau, E. Finot, G. Legay, M. Cherkaoui-Malki, and N. Latruffe. **Direct measurement of the melting temperature of supported DNA by electrochemical method**. *Nucleic Acids Research*, **31**:e150, 2003.

[93] R. Jin, G. Wu, Z. Li, C. A. Mirkin, and G. C. Schatz. **What Controls the Melting Properties of DNA-Linked Gold Nanoparticle Assemblies?** *Journal of the American Chemical Society*, **125**:1643–1654, 2003.

[94] J. Xu and S. L. Craig. **Thermodynamics of DNA Hybridization on Gold Nanoparticles**. *Journal of the American Chemical Society*, **127**:13227–13231, 2005.

[95] P. L. Biancaniello, A. J. Kim, and J. C Crocker. **Colloidal interactions and self-assembly using DNA hybridization**. *Physical Review Letters*, **94**:058302, 2005.

[96] J. R. Lackowicz. *Principles of Fluorescence Spectroscopy*. Springer Science+Business Media, LLC, New York, 2009.

[97] X. Michalet, F. F. Pinaud, L. A. Bentolila, J. M. Tsay, S. Doose, J. J. Li, G. Sundaresan, A. M. Wu, S. S. Gambhir, and S. Weiss. **Quantum Dots for Live Cells, in Vivo Imaging, and Diagnostics**. *Science*, **307**:538–544, 2005.

[98] A. Mooradian. **Photoluminescence of Metals**. *Physical Review Letters*, **22**:185–187, 1969.

[99] L. M. Clegg. *"Förster resonance energy transfer – FRET what is it, why do it, and how it is done" in "Laboratory Techniques in Biochemistry and Molecular Biology. Volume 33: FRET and FLIM Techniques" edited by T. J. W. Gadella.* Elsevier, Amsterdam, 2002.

[100] T. Förster. **Zwischenmolekulare Energiewanderung und Fluoreszenz**. *Annalen der Physik*, **6**:55–75, 1948.

[101] A. Wokaun, H. P. Lutz, A.P. King, U. P. Wild, and R. R. Ernst. **Energy transfer in surface enhanced luminescence**. *Optical Society of America*, **79**:509–513, 2006.

[102] K. Sokolov, G. Chumanov, and T. M. Cotton. **Enhancement of Molecular Fluorescence near the Surface of Colloidal Metal Films**. *Analytical Chemistry*, **70**:3898–3905, 1998.

[103] O. Kulakovich, N. Strekal, A. Yaroshevich, S. Maskevich, S. Gaponenko, I. Nabiev, U. Woggon, and M. Artemyev. **Enhanced Luminescence of CdSe Quantum Dots on Gold Colloids**. *Nano Letters*, **2**:1449–1452, 2002.

[104] H Ditlbacher, J. R. Krenn, G. Schider, A. Leitner, and F. R. Aussenegg. **Two-dimensional optics with surface plasmon polaritons**. *Applied Physics Letters*, **81**:1762–1764, 2002.

[105] J. Malicka, I. Gryczynski, Z. Gryczynski, and J. R. Lakowicz. **Effects of fluorophore-to-silver distance on the emission of cyanine-dye-labeled oligonucleotides**. *Analytical Chemistry*, **315**:57–66, 2003.

[106] B. Dubertret, M. Calame, and A. J. Libchaber. **Single-mismatch detection using gold-quenched fluorescent oligonucleotides**. *Nature biotechnology*, **19**:365–370, 2001.

[107] D.J. Maxwell, J. R. Taylor, and S. Nie. **Self-Assembled Nanoparticle Probes for Recognition and Detection of Biomolecules**. *Journal of the American Chemical Society*, **124**:9606–9612, 2002.

[108] K. Aslan and V. H. Perez-Luna. **Quenched Emission of Fluorescence by Ligand Functionalized Gold Nanoparticles**. *Journal of Fluorescence*, **14**:401–405, 2004.

[109] T. Soller, M. Ringler, M. Wunderlich, T. A. Klar, J. Feldmann, H.-P. Josel, Y. Markert, A. Nichtl, and K. Kürzinger. **Radiative and Nonradiative Rates of Phosphors Attached to Gold Nanoparticles**. *Nano Letters*, **7**:1941–1946, 2007.

[110] M. Ringler. *Plasmonische Nahfeldresonatoren aus zwei biokonjugierten Goldnanopartikeln.* PhD thesis, Faculty of Physics, Ludwig-Maximilians University, Munich, 2008.

[111] E. Dulkeith, A. Morteani, T. Niedereichholz, T. Klar, J. Feldmann, S. Levi, F. van Veggel, D. Reinhoudt, M. Möller, and D. Gittins. **Fluorescence Quenching of Dye Molecules near Gold Nanoparticles: Radiative and Nonradiative Effects**. *Physical Review Letters*, **89**:203002, 2002.

[112] E. Dulkeith, M. Ringler, T. A. Klar, J. Feldmann, A. Munoz-Javier, and W. J. Parak. **Gold Nanoparticles Quench Fluorescence by Phase Induced Radiative Rate Suppression**. *Nano Letters*, **5**:585–589, 2005.

[113] S. Bhowmick, S. Saini, V. B. Shenoy, and B. Bagchi. **Resonance energy transfer from a fluorescent dye to a metal nanoparticle**. *The Journal of Chemical Physics*, **125**:181102, 2006.

[114] P. Anger, P. Bharadwaj, and L. Novotny. **Enhancement and Quenching of Single-Molecule Fluorescence**. *Physical Review Letters*, **96**:113002, 2006.

[115] S. Kühn, U. Hakanson, L. Rogobete, and V. Sandoghdar. **Enhancement of Single-Molecule Fluorescence Using a Gold Nanoparticle as an Optical Nanoantenna**. *Physical Review Letters*, **97**:017402, 2006.

[116] J. I. Gersten and A. Nitzan. **Accelerated Energy Transfer Between Molecules Near a Solid Particle**. *Chemical Physics Letters*, **104**:31–37, 1984.

[117] M. Lessard-Viger, M. Rioux, L. Rainville, and D. Boudreau. **FRET Enhancement in Multilayer Core-Shell Nanoparticles**. *Nano Letters*, **9**:3066–3071, 2009.

[118] H. Szmacinski, R. Krishanu, and J. R. Lakowicz. **Effect of plasmonic nanostructures and nanofilms on fluorescence energy transfer**. *Journal of Biophotonics*, **2**:243–252, 2009.

[119] M. Durach, A. Rusina, V. I. Klimov, and M. I. Stockman. **Nanoplasmonic renormalization and enhancement of Coulomb interactions**. *New Journal of Physics*, **10**:105011, 2008.

[120] J. Zhou, J. Ralston, R. Sedev, and D. A. Beattie. **Functionalized Gold Nanoparticles: Synthesis, Structure and Colloid Stability**. *Journal of Colloid Interface Science*, **331**:251–262, 2009.

[121] C. Burda, X. Chen, R. Narayanan, and M.A. El-Sayed. **Chemistry and properties of nanocrystals of different shapes**. *Chemical Reviews*, **105**:1025–1102, 2005.

[122] K. Lu. *Nanoparticulate Materials: Synthesis, Characterization, and Processing*. John Wiley & Sons, Hoboken, 2013.

[123] T. K. Sau and A. L. Rogach. **Nonspherical Noble Metal Nanoparticles: Colloid-Chemical Synthesis and Morphology Control**. *Advanced Materials*, **22**:1781–1804, 2010.

[124] T. K. Sau and C. J. Murphy. **Seeded High Yield Synthesis of Short Au Nanorods in Aqueous Solution**. *Langmuir*, **20**:6414–6420, 2004.

[125] P.C. Angelome, H. Heidari Mezerji, B. Goris, I. Pastoriza-Santos, J. Perez-Juste, S. Bals, and L.M. Liz-Marzan. **Seedless Synthesis of Single Crystalline Au Nanoparticles with Unusual Shapes and Tunable LSPR in the near IR**. *Chemistry of Materials*, **24**:1393–1399, 2012.

[126] J. Turkevich, P. C. Stevenson, and J. Hillier. **A Study of the Nucleation and Growth Processes in the Synthesis of Colloidal Gold**. *Discussions of the Faraday Society*, **11**:55–75, 1951.

[127] S. J. Hurst, A. K. R. Lytton-Jean, and C. A. Mirkin. **Maximizing DNA Loading on a Range of Gold Nanoparticle Sizes**. *Analytical Chemistry*, **78**:8313–8318, 2006.

[128] **The Merck Index Online**. `https://www.rsc.org/Merck-Index/monograph/mono1500001236/biotin?q=unauthorize`. Accessed: 2014-02-06.

[129] E. A. Bayer, H. Ben-Hur, Y. Hiller, and M. Wilchek. **Postsecretory modifications of streptavidin.** *Biochemical Journal*, **259**:369–376, 1989.

[130] A. Arakaki, S. Hideshima, T. Nakagawa, D. Niwa, T. Tanaka, T. Matsunaga, and T. Osaka. **Detection of biomolecular interaction between biotin and streptavidin on a self-assembled monolayer using magnetic nanoparticles**. *Biotechnology and Bioengineering*, **88**:543–546, 2004.

[131] J. DeChancie and K. N. Houk. **The Origins of Femtomolar Protein-Ligand Binding: Hydrogen-Bond Cooperativity and Desolvation Energetics in the Biotin-(Strept)Avidin Binding Site**. *Journal of the American Chemical Society*, **129**:5419–5429, 2007.

[132] A. Holmberg, A. Blomstergren, O. Nord, M. Lukacs, J. Lundeberg, and M. Uhlan. **The biotin-streptavidin interaction can be reversibly broken using water at elevated temperatures**. *Electrophoresis*, **26**:501–510, 2005.

[133] T. K. Sau, A. L. Rogach, M. Döblinger, and J. Feldmann. **One-Step High-Yield Aqueous Synthesis of Size-Tunable Multispiked Gold Nanoparticles**. *Small*, **7**:2188–2194, 2011.

[134] H. M. Chen, R.-S. Liu, and D. P. Tsai. **A Versatile Route to the Controlled Synthesis of Gold Nanostructures**. *Crystall Growth & Design*, **9**:2079–2087, 2009.

[135] M. Grzelczak, J. Perez-Juste, P. Mulvaney, and L. M. Liz-Marzan. **Shape Control in Gold Nanoparticle Synthesis**. *Chemical Society Reviews*, **37**:1783–1791, 2008.

[136] F. Hao, C. L. Nehl, J. H. Hafner, and P. Nordlander. **Plasmon Resonances of a Gold Nanostar**. *Nano Letters*, **7**:729–732, 2007.

[137] C. Hrelescu, T. K. Sau, A. L. Rogach, F. Jäckel, and J. Feldmann. **Single Gold Nanostars enhance Raman Scattering**. *Applied Physics Letters*, **94**:153113, 2009.

[138] M. Hanauer, S. Pierrat, I. Zins, A. Lotz, and C. Sönnichsen. **Separation of Nanoparticles by Gel Electrophoresis According to Size and Shape**. *Nano Letters*, **7**:2881–2885, 2007.

[139] S. A. Claridge, S. L. Goh, J. M. J. Frechet, S. C. Williams, C. M. Micheel, and A. P. Alivisatos. **Directed Assembly of Discrete Gold Nanoparticle Groupings Using Branched DNA Scaffolds**. *Chemistry of Materials*, **17**:1628–1635, 2005.

[140] N. Pernodet, M. Maaloum, and B. Tinland. **Pore size of agarose gels by atomic force microscopy**. *Electrophoresis*, **18**:55–58, 1997.

[141] A. Zayats and D. Richardson. *Nano-optics and Near-field Optical Microscopy*. Artech House, Inc., Norwood, 2009.

[142] D. B. Williams and C. B. Carter. *Transmission Electron Microscopy: A Textbook for Materials Science, Volume 1*. Springer, New York, 2009.

[143] M. Dienerowitz, M. Mazilu, P. J. Reece, T. F. Krauss, and K. Dholakia. **Optical vortex trap for resonant confinement of metal nanoparticles**. *Optics Express*, **16**:4991–4999, 2008.

[144] A. Ohlinger, S. Nedev, A. A. Lutich, and J. Feldmann. **Optothermal Escape of Plasmonically Coupled Silver Nanoparticles from a Three-Dimensional Optical Trap**. *Nano Letters*, **11**:1770–1774, 2011.

[145] **Hamamatsu: Streak Lifetime Imaging (FLIM) Camera**. `https://www.learn.hamamatsu.com/tutorial/java/streakcamera/`. Accessed: 2013-08-24.

[146] D. E. Spence, P. N. Kean, and W. Sibbett. **60-fsec pulse generation from a self-mode-locked Ti: sapphire laser**. *Optics letters*, **16**:42–44, 1991.

[147] P. C. D. Hobbs. *Building Electro-Optical Systems: Making it all Work, Second Edition*. Wiley & Sons, Inc, 2009.

[148] T. J. Yim, Y. Wang, and X. Zhang. **Synthesis of a gold nanoparticle dimer plasmonic resonator through two-phase-mediated functionalization**. *Nanotechnology*, **19**:435605, 2008.

[149] P. J. Pauzauskie, A. Radenovic, E. Trepagnier, H. Shroff, P. Yang, and J. Liphardt. **Optical trapping and integration of semiconductor nanowire assemblies in water**. *Nature Materials*, **5**:97–101, 2006.

[150] P. H. Jones, F. Palmisano, F. Bonaccorso, P. G. Gucciardi, G. Calogero, A. C. Ferrari, and O. M. Marago. **Rotation Detection in Light-Driven Nanorotors**. *ACS Nano*, **3**:3077–3084, 2009.

[151] K. D. Bonin, B. Kourmanov, and T. G. Walker. **Light torque nanocontrol, nanomotors and nanorockers**. *Optics Express*, **10**:984–989, 2002.

[152] L. Tong, V. D. Miljkovic, and M. Käll. **Alignment, Rotation, and Spinning of Single Plasmonic Nanoparticles and Nanowires Using Polarization Dependent Optical Forces**. *Nano Letters*, **10**:268–273, 2010.

[153] L. Osinkina, S. Carretero-Palacios, J. Stehr, A. A. Lutich, F. Jäckel, and J. Feldmann. **Tuning DNA Binding Kinetics in an Optical Trap by Plasmonic Nanoparticle Heating**. *Nano Letters*, **13**:3140–3144, 2013.

[154] H. H. Richardson, Z. N. Hickman, A. O. Govorov, A. C. Thomas, W. Zhang, and M. E. Kordesch. **Thermooptical Properties of Gold Nanoparticles Embedded in Ice: Characterization of Heat Generation and Melting**. *Nano Letters*, **6**:783–788, 2006.

[155] P. M. Bendix, S. N. S. Reihani, and L. B. Oddershede. **Direct Measurements of Heating by Electromagnetically Trapped Gold Nanoparticles on Supported Lipid Bilayers**. *ACS nano*, **4**:2256–2262, 2010.

[156] M. Honda, Y. Saito, N. I. Smith, K. Fujita, and S. Kawata. **Nanoscale heating of laser irradiated single gold nanoparticles in liquid**. *Journal of Chemical Physics*, **19**:12375–12383, 2011.

[157] M. Hu and G. V. Hartland. **Heat dissipation for Au particles in aqueous solution: relaxation time versus size**. *Journal of Physical Chemistry B*, **106**:7029–7033, 2002.

[158] L. Tong, V. D. Miljkovic, P. Johansson, and M. Käll. **Plasmon Hybridization Reveals the Interaction Between Individual Colloidal Gold Nanoparticles Confined in an Optical Potential Well**. *Nano Letters*, **11**:4505–4508, 2010.

[159] R. Alvarez-Puebla, L. M. Liz-Marzan, and F. J. Garcia de Abajo. **Light Concentration at the Nanometer Scale**. *The Journal of Physical Chemistry Letters*, **1**:2428–2434, 2010.

[160] S. Barbosa, A. Agrawal, L. Rodriguez-Lorenzo, I. Pastoriza-Santos, R. A. Alvarez-Puebla, A. Kornowski, H. Weller, and L. M. Liz-Marzan. **Tuning Size and Sensing Properties in Colloidal Gold Nanostars**. *Langmuir*, **26**:14943–14950, 2010.

[161] L. Osinkina, T. Lohmüller, F. Jäckel, and J. Feldmann. **Synthesis of Gold Nanostar Arrays as Reliable, Large-Scale, Homogeneous Substrates for Surface-Enhanced Raman Scattering Imaging and Spectroscopy**. *The Journal of Physical Chemistry C*, 2013.

[162] T. Vo-Dinh, F. Yan, and M. B. Wabuyele. **Surface-enhanced Raman Scattering for Medical Diagnostics and Biological Imaging**. *Journal of Raman Spectroscopy*, **36**:640–647, 2005.

[163] W. Lee, S. Y. Lee, R. M. Briber, and O. Rabin. **Self-Assembled SERS Substrates with Tunable Surface Plasmon Resonances**. *Advanced Functional Materials*, **21**:3424–3429, 2011.

[164] Q. Su, X. Ma, J. Dong, C. Jiang, and W. Qian. **A Reproducible SERS Substrate Based on Electrostatically Assisted APTES-Functionalized Surface-Assembly of Gold Nanostars**. *ACS Applied Materials & Interfaces*, **3**:1873–1879, 2011.

[165] M. Mueller, M. Tebbe, D. V. Andreeva, M. Karg, R. A. Alvarez-Puebla, N. Pazos-Perez, and A. Fery. **Large-Area Organization of pNIPAM-Coated Nanostars as SERS Platforms for Polycyclic Aromatic Hydrocarbons Sensing in Gas Phase**. *Langmuir*, **28**:9168–9173, 2012.

[166] J. Slavik. *Fluorescence Microscopy and Fluorescent Probes, Volume 2.* Plenum Press, New York, 2007.

[167] H. C. Cheung. *"Resonant Energy Transfer" in "Topics in fluorescence spectroscopy. Volume 2: Priniples." edited by R. J. Lackowicz.* Springer Science+Business Media, LLC, New York, 1991.

Acknowledgments

First of all I would like to thank Prof. Dr. J. Feldmann for the oppotunity to do my PhD in his excellent research group. I am very gratefull to Prof. Dr. J. Feldmann for his time, help, support and advices during this time.

Also I would like to acknowledge my supervisor Dr. F. Jäckel for his expertise, kindness and support. Working under the supervision of Dr. F. Jäckel was a great opportunity to improve my professional skills.

I am also very happy that I had a chance to work together with Dr. S. Carretero-Palacios, Dr. T. Lohmüller, Dr. A. A. Lutich and Dr. J. Rodriguez-Fernandez, from whom I have learned a lot, not only about physics and chemistry but also about the attitude to research and life.

I would like to thank Dr. H. M. Abubaker, Dr. H. Ba, A. Babyinina, V. Baumann, T. Becker, Dr. M. Berr, Dr. A. Blanch, Dr. N. Bouchonville, Dr. M. Carlson, Dr. A. Deak, Dr. F. Deschler, J. Do, Dr. A. Dubavik, V. Fässler, Dr. M. Fedoruk, Dr. C. Hrelescu, S. Kirchner, Dr. I. Kriegel, P. Kühler, Dr. T. Limmer, L. Liu, S. Nedev, Dr. S. Neyshtadt, Dr. A. Ohlinger, T. Pfeiffer, Dr. R. Tautz and all the other collegues for the productive and happy time together in the labs, in the group meetings and during our free time. Special thanks to those of them who helped me with the corrections of this thesis.

My thanks also go to G. Adam, A. Helfrich, C. Holopirek and S. Niedermeyer.

Further I would like to acknowledge the Elite Network of Bavaria for the financial support through the International Doctorate Program NanoBioTechnology (IDK) and to acknowledge the financial support through the project SFB1032.

Finally I would like to thank the spokeman of the IDK, Prof. Dr. J. Rädler for his support, interesting scientific discussions and for all the great things he and the program manager M. Pinto organized in the frames of the program. It was an exciting time and I am very proud to be a part of IDK.